Measurement of $\sigma(\psi(3770) \to p\overline{p}\pi^0)$ and Determination of $\sigma(p\overline{p} \to \psi(3770)\pi^0)$ for the $\overline{P}$ANDA Experiment

Inaugural-Dissertation

zur Erlangung des Doktorgrades der Naturwissenschaften
der Justus-Liebig-Universität Gießen im Fachbereich 07
(Mathematik und Informatik, Physik, Geographie)

vorgelegt von

Matthias Gunter Ullrich

aus Pohlheim

II. Physikalisches Institut
der Justus-Liebig-Universität Gießen
im November 2013

Dekan: Prof. Dr. Peter Jens Klar
1. Berichterstatter: Prof. Dr. Wolfgang Kühn
2. Berichterstatter: Prof. Dr. Alfred Müller

Für meine Eltern

Abstract

Production cross sections for charmonium states and charmonium hybrids in $p\bar{p}$ annihilations are relevant for the planned $\overline{\text{P}}$ANDA experiment, as they allow for the evaluation of luminosity requirements and detection strategies and to perform detector simulations.

In this work the cross section of $\psi(3770) \to p\bar{p}\pi^0$ and its partial decay width has been measured with the BESIII detector located at the electron positron collider BEPCII in Beijing, China. Using a model based on a constant amplitude approximation requiring this partial decay width as an input, the cross section for the process of $p\bar{p} \to \psi(3770)\pi^0$ has been evaluated.

The cross section of $\psi(3770) \to p\bar{p}\pi^0$ has been extracted considering interference between resonant ($e^+e^- \to \psi(3770) \to p\bar{p}\pi^0$) and continuum production amplitude ($e^+e^- \to p\bar{p}\pi^0$). The Born cross section $\sigma_0(e^+e^- \to p\bar{p}\pi^0)$ is determined to be $0.87^{+1.27}_{-0.72}$ pb (<2.7 pb at a 90% confidence level). The phase angle of the interference is in agreement with a total destructive interference between resonant and continuum production amplitude.

The cross section for the process $p\bar{p} \to \psi(3770)\pi^0$ has been calculated to be less than 9.7 nb at a 90% confidence level at a center of mass energy of 5.26 GeV and is thus still in reach of the $\overline{\text{P}}$ANDA experiment.

A second focus of this work lies on the development and implementation of simulation and reconstruction software for an upgrade of the time of flight detector of the BESIII experiment into the BESIII offline software system (BOSS). It is foreseen to replace the endcap time of flight system based on plastic scintillators with a system of Multigap Resistive Plate Chambers (MRPC) in the year 2015.

The geometrical and material properties of the upgraded detector and a realistic model for signal production have been implemented into the simulation framework. The model allows for the simulation of the MRPC's characteristics and is able to reproduce beam test results. The implemented reconstruction packages allow for a matching of the MRPC signals with the reconstructed tracks in the Mini Drift Chamber and the signals of other detector systems. Several correction routines, e.g. for walk corrections, for energy loss corrections and for the correction of the signal transition time in the readout strips are implemented, too.

It is shown that the total time resolution for pions and kaons with a momentum of around 1.45 GeV/c can be expected to be $\sim$80 ps. The upgrade thus will extend the capability for a pion/kaon separation at the 2σ level from momenta of about 1 GeV/c up to $\sim$1.45 GeV/c.

Contents

Introduction and Motivation

The $\overline{\text{P}}$ANDA (Anti$\underline{\text{P}}$roton $\underline{\text{A}}$nnihilations at $\underline{\text{D}}$armstadt) experiment to be build as a part of the future Facility for Antiproton and Ion Research (FAIR) located at the existing Gesellschaft für Schwerionenforschung (GSI) facility in Darmstadt, Germany will address the fundamental physics questions of quantum chromodynamics (QCD), mostly in the non-perturbative region [1]. It is designed to exploit the physics potential arising from a cooled, high-intensity antiproton beam covering the center of mass energy range between $\sim$2.3 and 5.5 GeV and will perform studies of antiproton-proton annihilation and reactions of antiprotons with heavier nuclear targets.

Its scientific program includes not only the search for gluonic excitations such as hybrids (quark-antiquark pairs with additional gluons) and glueballs (pure gluonic states), the study of in medium modifications of hadrons in nuclear matter and the study of the structure of the nucleon, but also hadron spectroscopy up to the region of charm quarks and especially a detailed investigation of the spectrum of charmonium and charmonium hybrid states, including the determination of masses, decay widths, decay properties and quantum numbers. Because of the unprecedented low momentum spread of the anti-proton beam and the possibility of mass scans, measurements of charmonium state masses with an accuracy of the order of 100 keV and of widths with a resolution better than 10% is possible [2].

The states formed in p$\overline{\text{p}}$ annihilations, in contrast to the ones formed in electron-positron annihilations, are not restricted to the quantum number $J^{PC} = 1^{--}$. They rather can have all non-exotic quantum numbers, as the annihilation process proceeds via two or three (virtual) gluons. However, states with exotic quantum numbers are still within the reach of $\overline{\text{P}}$ANDA , as they can be produced in a p$\overline{\text{p}}$ annihilation in association with a light meson (π^0, η, ρ, ω and ϕ) [3]. For example, the mass of the $J^{PC} = 1^{-+}$ exotic charmonium hybrid, which is expected to be the lightest one, is predicted to be in the range of 4.2-4.4 GeV/c^2 [4–7] and thus can be discovered by $\overline{\text{P}}$ANDA . The production in association with a light meson is not only restricted to exotic states. Conventional charmonium states, such as J/ψ, ψ(2S) and ψ(3770), can be formed with a light meson partner as well. So far, only a single exclusive cross section of this type is measured: p$\overline{\text{p}} \to \pi^0 J/\psi$. It was reported by the E760

collaboration to be 130±25 pb near an energy of about 3.5-3.6 GeV [8, 9].

The total proton-antiproton cross section at this energy is measured to be ∼60 mb [10], and thus about eight magnitudes larger compared to exclusive process. Even after neglecting the elastic proton-antiproton cross section (about 15 mb [10]) the ratio does not change significantly. Thus, a main task for the study of such channels at $\overline{\text{P}}$ANDA experiment is the separation of hadronic background from the charm signal.

To investigate detection strategies, to evaluate luminosity requirements and to perform detailed detector simulations with theoretical preferred states, the knowledge of production cross sections for charmonium and charmonium hybrid states is indispensable.

Various theoretical models allow for the estimation of the required cross sections. Estimates based on the quark-gluon string model [11], the annihilation of di-quark pairs [12] or on hypothetic contributions of $D\overline{D}$ molecule pairs to the resonances above the open-charm threshold [13] suggest cross section in the range of 10 nb up to a few 100 nb. In case of direct resonance formation in p$\overline{\text{p}}$ annihilations the cross section can also be calculated with the help of detailed balance. The results of this method are usually in the order of a few nb for resonances above the open charm threshold [1]. For the production in association with a light meson, the cross section can be determined by models based on initial-state light meson emission, constant amplitude approximation and crossing symmetries [3, 8, 14]. All those models require as an input parameter the a priori unknown partial decay width of the investigated state into p$\overline{\text{p}}$ or p$\overline{\text{p}}\pi^0$, respectively.

The partial decay widths into p$\overline{\text{p}}$ and p$\overline{\text{p}}\pi^0$ for charmonium states below the open charm threshold have been reported by various experiments and are relatively well known. However, information on the partial decay widths of higher lying charmonium states is still lacking [10].

The $\psi(3770)$ resonance with a mass of ∼3.773 GeV/c^2 and a width of about 27.3 MeV is the lightest charmonium state above the open charm threshold. It was predicted by *Eichten et al.* [15] and is often interpreted as a mixture of a D-wave and the 2^3S_1 S-wave state, dominated by the $^3\text{D}_1$ D-wave state [16–18]. Due to its closeness to the $D\overline{D}$ threshold and its large width, it was expected to decay almost entirely into $D\overline{D}$ states.

However, a total non-$D\overline{D}$ branching fraction of (14.7±3.2) % has been reported by the BES collaboration [19–22]. This result did not consider interference effects between resonant and continuum production and the CLEO collaboration did measure the non-$D\overline{D}$ branching ratio to be $(-3.3 \pm 1.4^{+6.6}_{-4.4})\%$ considering interference of electromagnetic resonant decays and continuum decays [23]. However, considering interference of continuum decays with the 3-gluon resonant amplitude might change the observed cross section to light hadrons up to about 1.9 nb and thus influence the measured branching ratio [24, 25].

To clarify the situation, both, the BES and CLEO collaboration did perform searches for non-D$\overline{D}$ decay modes [26–28], but the total sum of the of the non-$D\overline{D}$ branching fractions is less than 2 %. The branching fraction into p$\overline{\text{p}}\pi^0$ and consequently the partial decay width,

required as input parameter for the cross section estimation for the $\overline{\text{P}}$ANDA experiment, is only known as an upper limit [10], too.

A great and unique opportunity to determine the partial decay width and to investigate possible interference effects offers the Beijing Electron Spectrometer III (BESIII) experiment, located at the Beijing Electron-Positron Collider II (BEPCII) in Beijing, China at the Institute of High Energy Physics, commonly known as IHEP. The symmetric e^+e^- experiment is optimized for the investigation of charm and τ physics (1.8 GeV $\leq \sqrt{s} \leq$ 4.5 GeV, where $\sqrt{s}$ is the available center of mass energy) [29, 30]. Up to now the BESIII experiment has already accumulated the world largest data sets of J/ψ, $\psi(2S)$, $\psi(3770)$, $\psi(4040)$, $\psi(4260)$ and $\psi(4360)$ events in e^+e^- collisions — and still more data is to be expected in the upcoming years.

The main focus of interest of this thesis is set on the extraction of the partial decay width of $\psi(3770) \to p\overline{p}\pi^0$ by a lineshape analysis using the data collected by the BESIII detector. Interference effects between the continuum ($e^+e^- \to p\overline{p}\pi^0$) and resonant ($e^+e^- \to \psi(3770) \to p\overline{p}\pi^0$) production process, which can be interpreted as the interference between the electromagnetic and the 3-gluon production amplitude [24, 25], will be considered as well. This result is eventually used to predict the cross section of $p\overline{p} \to \pi^0\psi(3770)$ — with the model presented in [8] — over the whole energy range to be investigated by the $\overline{\text{P}}$ANDA experiment.

Since the $\overline{\text{P}}$ANDA experiment will not start its operation before 2018 and more information on exclusive $p\overline{p}$ cross sections is required, this thesis discusses also a possible upgrade for the BESIII detector leading to improved analysis results and thus consequently to better estimates for the $\overline{\text{P}}$ANDA experiment. The presented upgrade is an improved endcap Time of Flight (ToF) system based on a MRPC. Detailed simulations in a realistic environment using the offline software BOSS (BESIII Offline Software System) of the BESIII experiment have been performed. They show that a total time resolution of 80 ps can be reached and the detector system will thus allow for a pion/kaon discrimination at a 95% confidence level up to momenta of 1.4 GeV/c.

Such high momentum pions and kaons can be observed in decays of all charmonium states into light hadrons, but more frequently for states above the open charm threshold [10]. A lot of new resonances, which can not be simply build of only one charm and anticharm quark, have been discovered in the recent decade in this mass region (e.g. the $J^{PC} = 1^{++}$ X(3872) [31, 32] or the charged charmonium like state Z(3900) [33]) and the $\overline{\text{P}}$ANDA experiment may help to shed further light into the nature of these states.

This thesis presents after a brief introduction into the required theoretical background, both the setup of the $\overline{\text{P}}$ANDA and the BESIII detector. The fifth chapter presents the ToF upgrade and shows the performance and results of the developed simulation and reconstruction software packages. The next chapter describes all details concerning the analysis of $\psi(3770) \to p\overline{p}\pi^0$ and the determination of the cross section of $p\overline{p} \to \pi^0\psi(3770)$. This

chapter is followed by a section summarizing and discussing the results and giving brief outlook.

Chapter 2

Theoretical Background

2.1. The Standard Model of Elementary Particle Physics

The standard model of particle physics requires just a few elementary particles, which are the basic constituents of all matter. They interact via four fundamental interactions; three of these a described in the standard model by the means of Quantum Field Theory (QFT). Generally speaking, a QFT consists of equations describing the movement and interactions of particles (fields). They all are combined in a Lagrangian density, which controls the whole dynamics and kinematics of the theory.

By introducing basic symmetries — e.g. the physic does not depend on shifts in the spatial coordinates — the number of allowed equations is reduced and the mass of force carriers is restricted to be zero. However, force carriers (and also the elementary particles) may gain masses through the process of electro-weak symmetry breaking, for which the famous Higgs-boson is required (It has been discovered at the Large Hadron Collider in 2012 [34, 35]).

The symmetry operations can be described mathematically by Lie groups; the symmetry group of the standard model is a product of three different groups, namely

$$SU(3) \otimes SU_L(2) \otimes U(1) \quad,$$

where SU means "Special Unitary".

The strong interaction is described by the non-abelian $SU(3)$ symmetry. The number of its gauge bosons (force carriers) is given by the relation n=dim^2(Group)-1 and thus is eight. The weak interaction, including three gauge boson, is described by $SU(2)$ symmetry; the subscript L denotes that it only acts on left handed fermions. The electromagnetic interaction with only one gauge boson is described by the unitary group 1 (U(1)).

Particles The standard model requires twelve elementary particles (and the corresponding antiparticle) with half integer spin — which are the fundamental building blocks of matter — and elementary force carriers — which mediate the interaction between the particles. They particles with half integer spin obey the Fermi-Dirac statistic and therefore, are called *fermions*. The force carriers (photon (γ), gluon (g), Z^0 and $W^{\pm}$

Fermions	Generations			Electric	Color	Weak	Force
	1	2	3	Charge [e]	Charge	Charge	Carrier
Leptons	ν_e	ν_μ	ν_τ	0	−	✓	γ
	e	μ	τ	-1	−	✓	g
Quarks	**up**	**charm**	**top**	+2/3	✓	✓	$W^\pm$, Z^0
	down	**strange**	**bottom**	-1/3	✓	✓	H

Table (2.1) The twelve elementary fermions arranged in three generations and the gauge bosons (force carrier) of the standard model. The three next-to-last columns denote whether they carry a certain charge, which allows them to participate on the corresponding interaction.

bosons and Higgs boson (H)) have integer spin and are called Bosons as they obey the Bose-Einstein statistics. The fermions can be again divided into a group of six quarks and six leptons according to their different charges (compare to table 2.1). According to their increasing masses, they can be arranged into 3 generations: Each generation contains a neutral and charged lepton and a positively and a negatively charged quark. Why there are exactly three generations of fundamental particles is still unclear, but the possibility of undiscovered generations is rather small. The width of the Z^0 resonance proves that only three neutrino generations with a mass smaller than 1/2 of the Z^0's mass are existing. Since the known neutrinos have rather small masses, it is very unlikely that there are more very massive ones.

It is worth to mention, that all known stable matter is build from the two quarks of the first generation.

Electromagnetic Interaction The electromagnetic interaction is mediated by photons and described within the framework of Quantum Electro Dynamic (QED). The photon couples to the electric charge of the particles and therefore, neutral particles do not interact in first order electromagnetically. The range of the electromagnetic interaction is not limited as photons carry no mass and do not interact with each other (in first order).

Strong Interaction Gluons are the force carrier of the strong interaction. They couple to color charge, which is carried by quark and antiquarks, and by the gluons themselves. The color charge carried by the gluons leads to the unique first order coupling of gluons to themselves. This effect leads to a running coupling constant α_s already at small distances (see figure 2.1) and the *confinement*: If one tries to separate two quarks, the color force between them will steadily increase until sufficient energy is accumulated to produce quark-antiquark pairs out of the vacuum. This also implies that neither quarks or antiquarks can exist as free particles. However, at zero distance
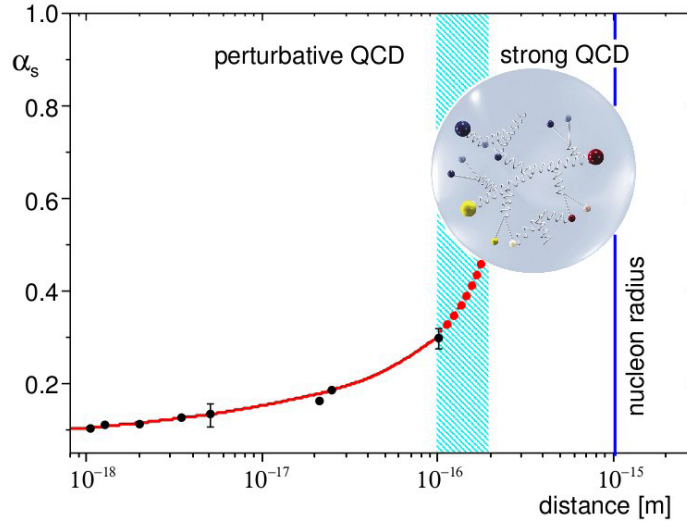
Figure (2.1) The running coupling constant of the strong interaction (taken from [10]). For distances between quarks in the order of some 10^{-16} m, the color forces are strong enough to create quark-antiquark pairs from the vacuum. The $\overline{\text{P}}$ANDA experiment will investigate the properties of this region. The figure is taken from [36].

the quarks are believed to be free, no force acts on them; this principle is known as *asymptotic freedom*.

Quarks can also form stable particles, the hadrons, which are held together by the strong force. They can be divided into different categories: Particles build of three quarks or antiquarks are called baryons, particles build of a quark and an antiquark are called mesons. Also particles build of four or more quarks or antiquarks (multi quark states), states build of quarks, antiquarks and additional gluons (hybrids), or even states build only of gluons (glueballs) are allowed by QCD. All the latter states are referred to as exotica.

The color charge has three manifestations (often chosen to be *red, green and blue*) and due to this additional degree of freedom one would expect a lot of hadrons, which differ only by their color charge. However, such a variety of hadrons is not observed and the absence is explained by allowing only color neutral states: All three colors added together are colorless or a color cancels its corresponding anticolor.

Weak Interaction The weak interactions is the only interaction mediated by massive force carriers, denoted by $W^{\pm}$ and Z^{0}, resulting in the limited range of only $\sim 10^{-3}$ fm. It acts on all leptons with the same strength, but the coupling strength to quarks is non-universal. The introduction of weak eigenstates, which are obtained from rotations of mass eigenstates of the quarks, has solved the dilemma of non-universality. The rotations are described in the famous CKM (Cabibbo-Kobayashi-Maskawa) ma-

trix. The squared absolute value of the matrix's entries describe the probability that a given quark changes its flavor by emitting or absorbing a charged W boson. Flavor changing neutral currents via the emission or absorption of the neutral Z boson do not exist in the standard model.

The weak interaction is also the only one violating charge conjugation C and parity symmetry P: Its force carriers do only couple to the left-handed component of particles and the right-handed component of antiparticles. The combined "charge conjugation parity" symmetry CP, which long time was believed to be preserved, is violated, too. Whether the combined CPT symmetry is conserved, which additionally considers the time reversal T, is still an open question and a field of active research. However, the standard model and all QFTs are based on a conserved CPT symmetry and a violation will clearly indicate physics beyond the standard model.

Gravitation Gravitation, by far the weakest of all known interactions, is the only one which is not yet contained in the standard model. It acts on all particles which have a mass, but the effects are small compared to the other interactions and thus it is often neglected in particle physics.

Since the standard model does not contain a quantum field theory describing the gravitational interaction and can not solve the problem of the unification of the electroweak interaction with the strong interaction, it is far from being complete. Numerous physical theories for *physics beyond the standard model* do exist and a lot of experiments — e.g. the current experiments at the TeV scale, running at CERN and the high precision experiments BELLE, BELLE II, BESIII and LHCb — are searching for experimental hints of new physics, which could help to exclude some of these theories.

2.2. Heavy Quarkonia

Heavy quarkonium refers to states composed of a c and $\bar{c}$ quark (charmonium) or a b and $\bar{b}$ quark (bottomonium). They can be used to probe the regime of QCD where non-perturbative effects are relevant (at low energies) and the high energy regime in which perturbation theory can be applied, as the coupling constant shrinks (compare to figure 2.1). Thus an investigation of the spectra is helpful to understand the features of QCD.

In contrast to the states build by u, d and s quarks, heavy quarkonia are well-defined in terms of the quark-antiquark pair flavor, i.e. they can be seen as states of pure c and $\bar{c}$ or pure b and $\bar{b}$. Due to their small widths and large masses, they do not mix with each other. The mixing effect for the light quark flavors u, d and s can be directly observed for the light $\mathrm{J}^{PC}=0^{-+}$ states (pseudo-scalars) [10]. Toponium, states composed of a t and $\bar{t}$ quark, can not be formed, since the very massive top quark decays via the electroweak interaction before hadronization can take place.

QCD allows (theoretically) the calculation of all meson properties, but simple perturbation theory can not be used to determine properties such as masses, widths and decay rates. However, within the framework of non-relativistic models, effective field theories and lattice QCD particle spectra of charmonium or bottomonium can be calculated. A comparison of the calculated spectra with the measured ones, allows to put QCD on a strict test. One question, that might be answered by heavy quarkonium spectroscopy, is the existence of exotic states like quark-gluons hybrids or tetraquarks; candidates would be states which do not fit into the $q\bar{q}$ model (e.g. the 1^{++} X(3872) [32] , which has been discovered by the BELLE experiment in 2003 [31]) or/and have exotic quantum numbers.

One simple model which allows to calculate the spectra of the states is based on the phenomenological derived Cornell potential [37]

$$V(r) = -\frac{4}{3}\frac{\alpha_s}{r} + kr$$

with α_s the strong coupling constant and k the string tension taking into account the confinement at large distances. The first term, a Coulomb-like part, is describing the interaction a short distances, which should be dominated by a single gluon exchange.

However, it is possible to derive this potential with some more additional corrections, similar to how Gregor Breit did it for a potential for electron-electron and electron-positron scattering [38, 39]. The resulting potential [40],

$$
\begin{aligned}
V^{\text{Breit}}(\vec{r}; \vec{p}_1, \vec{p}_2) = & -\frac{4\alpha_s}{3r} + \frac{4\pi\alpha_s}{3m_q^2}\delta(\vec{r}) - \frac{2\alpha_s}{3m_q^2}\left[\frac{\vec{p}\cdot\vec{p}}{r} + \frac{(\vec{r}\cdot\vec{p})(\vec{r}\cdot\vec{p})}{r^3}\right] \\
& + \frac{4\alpha_s}{3m_q^2}\left[\frac{8\pi}{3}\delta(\vec{r})(\vec{s}_1\cdot\vec{s}_2) + \frac{3(\vec{s}_1\cdot\vec{r})(\vec{s}_2\cdot\vec{r}) - \vec{s}_1\cdot\vec{s}_2}{r^3}\right] \\
& + \frac{2\alpha_s}{m_q^2}\frac{(\vec{r}\times\vec{p})\cdot(\vec{s}_1 + \vec{s}_2)}{r^3} \quad ,
\end{aligned}
\tag{2.2.1}
$$

is based on an one-gluon exchange and considers also spin-orbit and spin-spin interactions, as well as the interaction arising from the magnetic dipole of the two quarks (tensor forces). The following abbreviations are used in the formula 2.2.1: m_q describes the quark mass, $\delta(r)$ the Dirac distribution, p and r are the momentum and the spatial coordinates and s is the corresponding spin of the particles. A term, taking into account the confinement has still to be added, but lattice gauge theories show (in the limit of static quarks) a linear behavior for large distances of r.

As relativistic effects are expected to be non-dominant in charmonium and bottomonium systems (the quark masses of the heavy quarkonia are dominating the masses of the mesons they build and thus should have non-relativistic velocities), the spectra can be calculated by simply solving the non-relativistic radial Schrödinger equation.

Figure 2.2 shows the calculated charmonium spectra, the experimental observed states and

some transition between those states. The states are ordered by their J^{PC} quantum numbers, which can be determined for *quark-antiquark states* as follows: J is the total angular momentum, which can be calculated by coupling the spins of its constituents S and the orbital angular momentum L. The parity quantum number P is related to the orbital angular momentum by $P=(-1)^{L+1}$ and its charge conjugation C is related to the spin S and the angular momentum L by $C=(-1)^{L+S}$.

The strong coupling constant α_s has been set to 0.29, the mass of the charm quark m_c to 1.22 GeV and the string tension σ to 1.3 GeV/fm for the calculations. The value of α_s and m_c can be considered as reasonable [10], but the value of the string tension is about 30 % larger than expected by lattice calculations [40].

Especially for the states below the open charm threshold the calculated spectra fits the experimental one rather well. However, for the states near and above this threshold discrepancies are arising; the simple model can not reproduce the whole spectrum and should be seen as an approximation. The $\psi(2S)$ state, for example, is predicted by the model to be above the $D\overline{D}$, also the other 1^{--} states with larger angular momentum are predicted far to high.

The black marked states in figure 2.2 are believed to be conventional $c\overline{c}$ states, since their masses fit with the prediction of some more sophisticated models (compare to [41]). Both, the J/ψ and the $\psi(2S)$ resonance have a small widths, as they can not decay into D-mesons and the strong decay via 1 or 2 virtual gluons is forbidden and at least 3 gluons are required, each of which has to have a sufficient energy to produce $q\overline{q}$ pairs (OZI rule [42–44]). At first glance one could expect that the X(3872) state might be the excited χ_{c1} state, but its width is far to small for a pure charmonium state above the $D\overline{D}$ threshold and the mass is about 50 MeV of from the value predicted in [41]. All the blue marked states are experimental observed resonances, which do not seem to fit into the $c\overline{c}$ model or where the quantum numbers are not yet known. The green bars indicate the observed charged states: They can not be conventional charmonia, but decay into a charged pion and a charmonium state. For the states, which are not marked with an arrow and a decay channel, transitions to other charmonium resonances have not been observed yet or are only known as an upper limit. Those states, except for the η_c', decay dominantly to *open charm*, i.e $D\overline{D}$ pairs.

2.3. Particle Antiparticle Collisions

A simple way to produce the previously discussed heavy quarkonium states are particle antiparticle collisions. Both, the $\overline{\text{P}}$ANDA and the BESIII experiments, to be presented in the chapters 3 and 4, (will) run in a similar energy region, but use different initial particles for their collisions: The BESIII experiment employs electron positron collisions, whereas the $\overline{\text{P}}$ANDA experiment will analyze collisions of protons and antiprotons; both techniques have advantages and disadvantages, which will be discussed briefly.
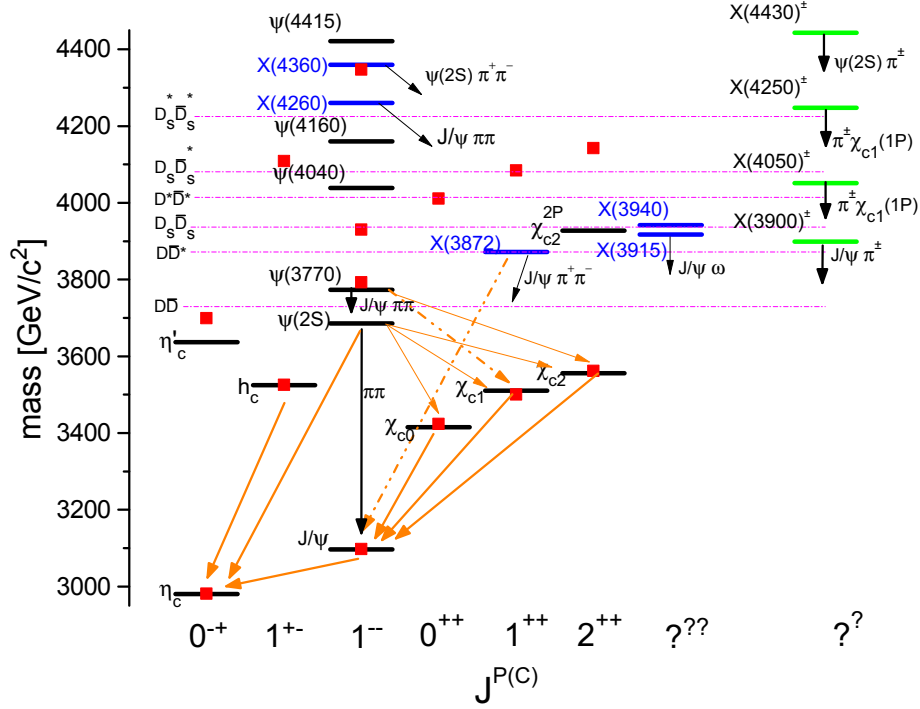
Figure (2.2)   The black lines indicate experimental measured states, which are commonly believed to be $c\bar{c}$ states, the blue lines are experimentally discovered neutral states, which seem not to fit in the ordinary $c\bar{c}$ model. The green lines describe charged resonances, which can not be made simply of a quark and an antiquark. The arrows and its labels show some of the observed transition between the charmonium states, the orange arrows stand for radiative γ transitions. The purple lines indicate the respective D thresholds. The names of the particles are according to the PDG's naming scheme [10], the X(3900) is the state, which has been recently discovered by the BESIII collaboration [33] and was named by them $Z_c(3900)$.

The red points are the masses which have been calculated by simply solving the non-relativistic Schrödinger equation with the potential from equation 2.2.1. The masses of the states below the $D\overline{D}$ threshold fit rather well to the one, which have been calculated with this simple model.
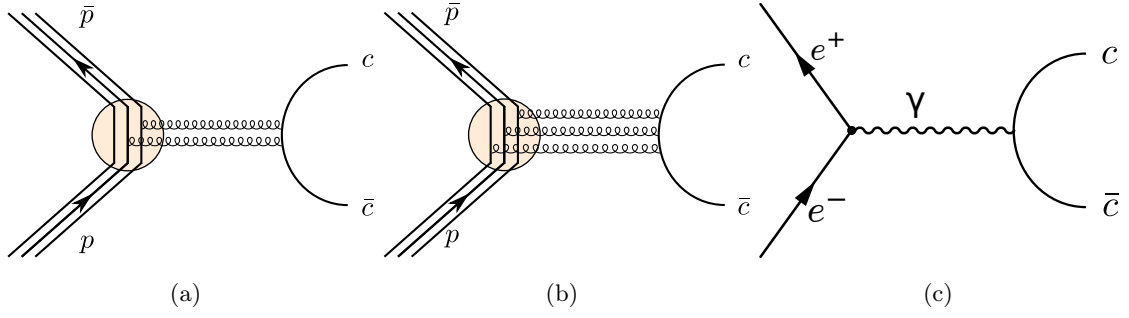
Figure (2.3) **(a)** and **(b)** show a possibility of charmonium production in proton-antiproton annihilations for parity odd and parity even states. **(c)** shows the production of charmonium via a virtual photon in electron-positron collisions. The produced state in electron-positron annihilations is restricted to quantum numbers of the virtual photon, whereas the proton-antiproton annihilation can produce a variety of of J^{PC} states (compare to table 2.2).

L	0	0	1	1	1	1	2	2	2	2
J^{PC}	0^{-+}	1^{--}	1^{+-}	0^{++}	1^{++}	2^{++}	1^{--}	2^{--}	3^{--}	2^{-+}
# *gluons*	3		2				3			

Table (2.2) J^{PC} states which can be produced in p$\bar{\text{p}}$ annihilation with an angular momentum $L \leq 2$. # *gluons* are the number of virtual gluons in the intermediate state. Note that exotic J^{PC} states can not be produced directly.

For precision experiments the knowledge of the initial state is rather important. Electrons and positrons are both particles with no substructure. As a consequence the energy of the collision is well known, despite small radiative tails arising due initial state radiation and bremsstrahlung. This is in marked contrast to proton-antiproton collisions. Even though the energy of the proton or the antiproton is well known, the particles, that interact with each other are the quarks and gluons. Hence, more effective degrees of freedom are existing and the energy of a certain collision is a priori unknown.

The annihilation of electrons and positrons is governed by the electroweak force, which means that the virtual intermediate state is either a virtual photon or a virtual Z boson. At center of mass energies below the Z boson mass($\sim$91 GeV), the photon is dominating the propagator — the annihilation proceeds almost entirely via the virtual photon (compare to figure 2.3). However, this also restricts the produced particle to the J^{PC} quantum number of the photon ($J^{PC}=1^{--}$). States with a large cross section and $J^{PC}=1^{--}$, such as J/ψ, ψ(2S), ..., can be produced almost background free.

To reach states with different quantum numbers one has to rely on transitions between

states. The J^{PC}=1^{--} ψ(2S) resonance, for instance, decays in about 27 % via emission of a real photon to the J^{PC}=1^{++} χ_{c0}, χ_{c1} and χ_{c2} states [10]. Transitions to J^{PC}=1^{+-} states, for example, can proceed via a decay into this state and a neutral pion and have also already been seen [10] (e.g. $\psi(2S) \rightarrow h_c \pi^0$).

In p$\overline{\text{p}}$ collisions, the particles do interact additionally via the strong interaction, which dominates the collision process (compare to figure 2.3). This complicates the analysis of the decay products, but allows for the study of gluon rich environments and also to produce a variety of J^{PC} states directly. Table 2.2 shows the reachable J^{PC} states for proton anti-proton annihilations, which proceed via 2 or 3 gluons for angular momentums of the p$\overline{\text{p}}$ system below 3 (both, the proton and antiproton have the quantum number J$^P = 1^+$). All the J^{PC} states which can be produced directly are non-exotic states, i.e. they can be composed from a quark and an antiquark partner.

However, also states with exotic quantum numbers (compare to section 2.1) may be produced in p$\overline{\text{p}}$ annihilations, but with an additional recoil particle. The neutral pion, with J$^{PC} = 0^{-+}$, as recoil particle would allow for the production of J^{PC}=1^{-+} and 2^{+-} exotic states (without additional angular momentum and considering only the J^{PC} quantum numbers listed in table 2.2).

Another drawback for proton-antiproton collisions is the requirement to produce the antiprotons. Electrons and positrons can be produced relatively easy and rather high currents and eventually also high luminosities can be achieved. The BESIII experiments for example has a design luminosity of $\mathcal{L}$ =10^{33} cm^{-2} s^{-1}, the BELLE experiment, which was located at the High Energy Accelerator Research Organization, commonly known as KEK, has reached a luminosity of $\mathcal{L} = 2.1 \cdot 10^{34}$ cm^{-2} s^{-1}, which is the world record.

The luminosities expected at the $\overline{\text{P}}$ANDA experiment ($\sim 2 \cdot 10^{31}$ cm^{-2} s^{-1} in the high resolution mode [1]) are significantly smaller compared to the one of electron positron machines. However, the assessment only based on the luminosities is not meaningful here, as the production cross sections at the experiments are different. $\overline{\text{P}}$ANDA might be easily produce much more events of a certain resonance (but also the amount of background events could be higher).

The $\overline{\text{P}}$ANDA Experiment

The $\overline{\text{P}}$ANDA (Anti$\underline{\text{P}}$roton $\underline{\text{An}}$nihilations at $\underline{\text{D}}$armstadt) experiment will be build as a part of the future Facility for Antiproton and Ion Research (FAIR) located at the existing GSI facility in Darmstadt, Germany. Figure 3.1 shows a layout of the existing GSI facility and the planned FAIR facility and the different experiments, which will address among other physics, topics in the field of nuclear structure and matter, atomic and plasma physics and also in the field of QCD, especially in the non-perturbative regime [1].
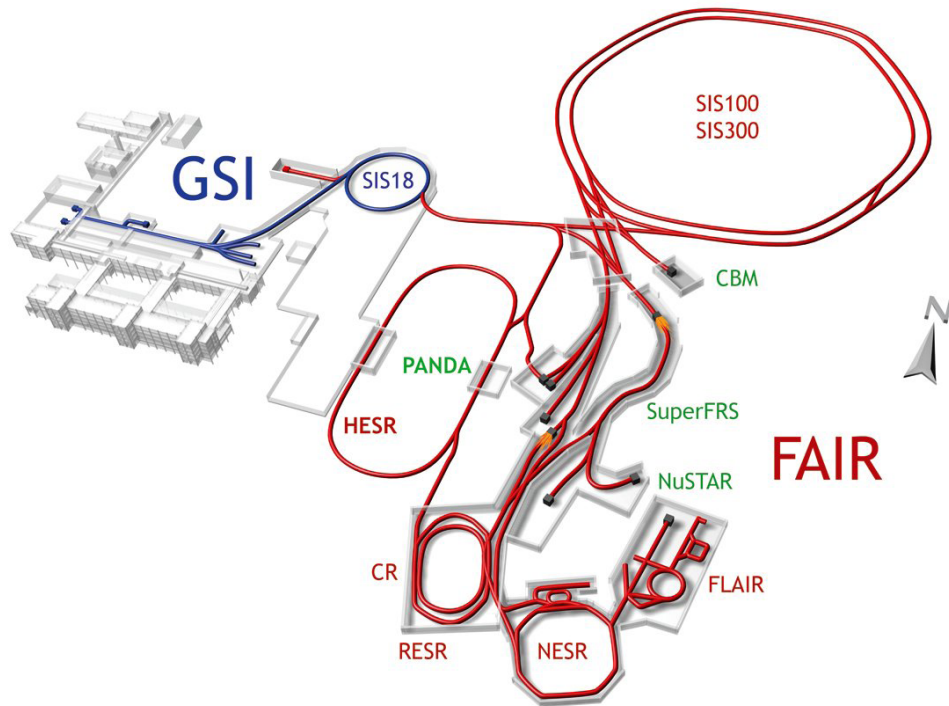
Figure (3.1)   The existing GSI facility (in blue) and the planned FAIR extension (in red). Shown are the location of the planned experiments, synchrotrons (SIS), the Collector Ring (CR), the experimental storage ring (NESR, HESR), the fragment separator (FRS) and the accumulator ring (RESR). The figure is taken from [36].
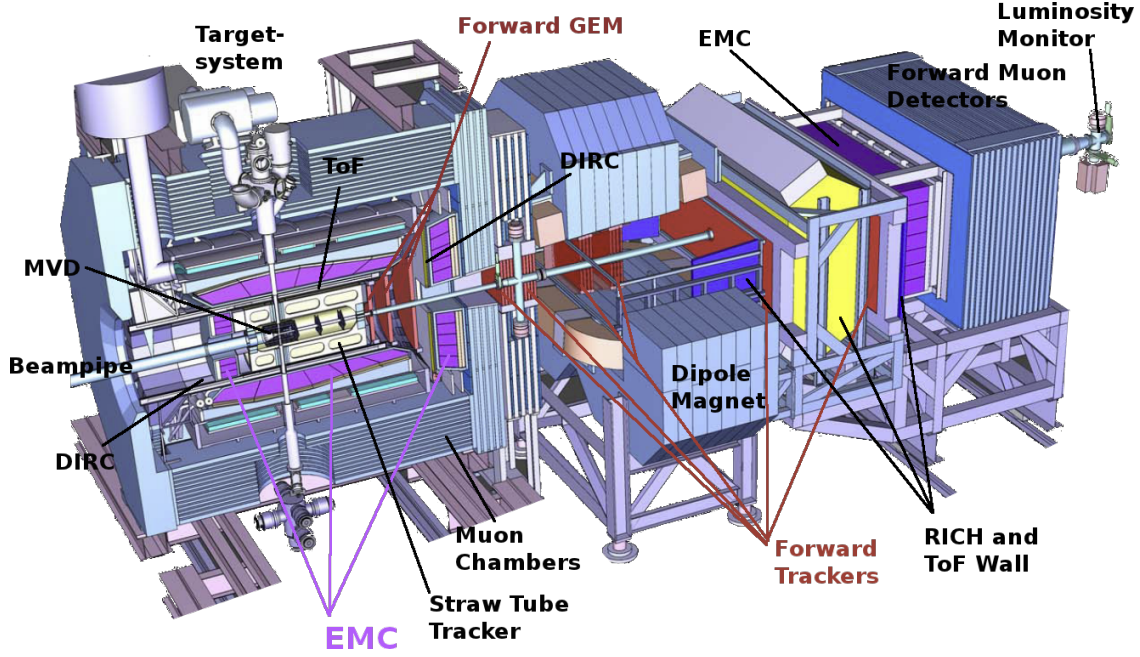
Figure (3.2) Schematic layout of the $\overline{P}$ANDA detector

FAIR will provide intense secondary pulsed beams of antiprotons, ions (from protons to uranium) and rare isotopes in a broad energy range. The antiprotons will be produced as follows: A proton beam with energy of about 30 GeV, provided by the primary synchrotron SIS-100, will collide with an internal nickel target of about 60 mm length to produce a bunch of at least 10^8 antiprotons [36], which will then be selected by a magnetic separator. The cycle of the antiproton production can be repeated every 10 s, but an upgrade for a cycle time of 5 s is foreseen [36]. The antiprotons will be compressed into single bunches and transfered into the High Energy Storage Ring (HESR).

The $\overline{P}$ANDA detector will be located at the HESR, which can supply $\overline{P}$ANDA with antiprotons over a broad momentum range from ~1.5 GeV/c to 15 GeV/c. The ring employs stochastic and electron cooling systems [45, 46] and is designed to run in two different operational modes: It can be driven in a *high resolution mode*, providing a luminosity $\mathcal{L}$ of ~$2 \cdot 10^{31}$ cm^{-2}s^{-1} and a Root Mean Square (RMS) momentum spread of $\sigma_p/p \leq 4 \cdot 10^{-5}$ in the momentum range from 1.5 to 8.9 GeV/c. The second operation mode, the *high luminosity mode*, provides a luminosity $\mathcal{L}$ up to $2 \cdot 10^{32}$ cm^{-2}s^{-1} and a RMS momentum spread of $\sigma_p/p \sim 10^{-4}$ in the momentum range of 1.5 to 15 GeV/c [1].

3.1. The $\overline{P}$ANDA Detector

The asymmetric detector (compare to figure 3.2), is designed to investigate high rate collisions of an antiproton beam with fixed proton or nuclear targets. Three different types of

targets are foreseen [1]:

Cluster Jet Target Narrow jets of hydrogen clusters are produced by the expansion of pressurized cold hydrogen gas through a Laval-type nozzle into vacuum. The jets will provide a homogeneous and adjustable target density without any time structure. The cluster size will vary from $\sim 10^3$ to $\sim 10^6$ hydrogen molecules with a density of about 10^{15} atoms/cm^3. This type of target technology can be used with heavier gases, too.

Pellet Target Frozen hydrogens spheres with a size of 25-40 μm will traverse the antiproton beam with a velocity of about 60 m/s, the spacing between the pellets will be between 0.5 mm and 5 mm. This type of target gives access to high effective target densities and can also be used with heavier gases such as N_2, Ar or Xe.

Nuclear Targets Different types of heavier nuclear targets, e.g. wire targets made of Be, C, Si or Al, can be inserted in the detector to study antiproton-nucleus interaction.

The detector itself is split into two spectrometer parts, the target spectrometer, situated around the interaction point, and the forward spectrometer, placed downstream the interaction point. The detector has a total angular acceptance of almost 4π.

3.1.1. The Target Spectrometer

The system consists of several sub-detectors, arranged in onion-shell-like layout; its design is asymmetric as most particles to be measured will go into the forward region. The modular design of the spectrometer allows for removing the backward endcap calorimeter and one layer of the forward muon detector. Instead of these components a dedicated nuclear target station and additional detector for photons, required for the study of hyper-nuclei, can be placed.

Micro Vertex Detector The innermost detector is a micro vertex detector based on radiation hard silicon pixel detectors with an inner radius of 2.5 cm and an outer radius of 13 cm. It will consist of 4 layers, the inner two layers are instrumented with pixel detectors, the outer two layers are equipped with double-sided silicon strip detectors [2]. It is optimized for the detection of secondary decay vertices from charmed and strange hadrons; another purpose is to improve the transverse momentum resolution of charged particles which enter the next outermost detector, the *Central Tracker*.

Straw Tube Tracker The central tracking detector will consist of 4636 of aluminumized Mylar tubes arranged in 27 layers in radial distances between 15 cm and 41.8 cm from the beam pipe. They result in a material budget of 1.2% of one radiation length [47]. In order to achieve a resolution of $\sim$3 mm in z-direction (parallel to the beam

axis), the 8 central layers are skewed. Each tube will have a diameter of 1 cm and consist of a single anode wire in the center. It will be filled with an argon based gas mixture to which CO_2 is added as quencher. The resolution in the $x - y$ plane is expected to be $\sim$150 μm, the momentum resolution $\delta p/p$ will be at the percent level.

Forward GEM Detectors Three planes of Gas Electron Multiplier (GEM), placed 1.1 m, 1.4 m and 1.9 m downstream the target, will measure particles emitted at angles below 22°, which thus are not covered by the straw tube trackers. It is not possible to replace the devices by a drift chamber, as the chamber would not sustain the high particle fluxes of about $3 \cdot 10^4$ cm^{-2}s^{-1} — it will suffer from aging [47].

Cherenkov Detectors The particle identification for charged particles with momenta higher than 0.8 GeV/c will be performed by the Detection of Internally Reflected Cherenkov (DIRC) light as realized in the BaBar detector [48]. Fused silica slabs will surround the beam pipe at radial distances from 45 cm to 54 cm. It is intended to focus the images of the light by lenses onto micro-channel plate photomultiplier which can be operated in the magnetic field. A similar DIRC concept is foreseen for the forward region [47].

Time of Flight detector The detector will placed just outside the barrel DIRC detector and will allow for particle identification of slow particles at large forward angles. The detector, based on scintillator tiles, read out by two silicon photomultipliers, can also be used to detect the photon conversions in the DIRC radiator. The time resolution for the device is expected to be about 100 ps [47].

Electromagnetic Calorimeter The electromagnetic calorimeter is the outermost detector within the magnetic field and will be build by lead tungstate ($PbWO_4$) crystals. The tapered crystals with a front size of 2.1×2.1 cm will be 20 cm long ($\sim$22 radiation length) and provide an energy resolution of better than 2% for particles with an energy below 1 GeV. 11,360 crystals will be installed in the barrel region, 3,600 in the forward region and 592 in the backward region (upstream the interaction point). The crystals will be read out by large area avalanche photo diodes, except in the backward region, where vacuum photo-triodes will be used. To achieve the required photon detection down to a few MeV, the crystals have to be cooled down to -25°C. This results in a factor of four larger light yield compared to room temperature [49].

Solenoid Magnet and Muon Chambers The superconducting magnet with a length of 2.8 m and an inner radius of 90 cm will provide a homogeneous field of 2 T; fluctuations in the field strength will be less than $\pm$2%. The return yoke of the magnet in the barrel part will be instrumented with 2,600 mini drift tubes (MDT), which will be arranged in 13 sensitive layers of a thickness of 3 cm [36]. MDTs are drift tubes with

capacitive coupled strips, which are read out on both ends to obtain a longitudinal spatial information. The layers are separated by 3 cm thick iron absorbers (the first and the last absorber have thickness of 6 cm), which will absorb the pions and so allow for a pion/muon separation. In the forward region 700 MDTs will be installed in 2 times six detection layers, placed behind 6 cm thick iron layers.

3.1.2. The Forward Spectrometer

The forward spectrometer located downstream the interaction point allows for the detection of particles emitted in the polar angle range between $5° < |\theta| < 10°$. It consists of several layer of sub-detectors required for tracking and particle identification.

Dipole Magnet A 2 Tm dipole magnet with a length of ∼2 m and a 1 m gap will be used to determine the momentum of the particles in the forward region. However, the dipole field will also influence the antiprotons, which did not undergo a reaction: At the maximum momentum of 15 GeV/c the incident beam will be deflected by 2.2° [36]. This deflection will be compensated by two correction dipole magnets, which will be placed around the detection system.

Forward Trackers 6 independent station of tracking detectors will measure the deflection of charged particles caused by the magnetic field. 2 stations each are placed in front and after the dipole magnet, the remaining pair is placed within the dipole field. Each station will consist of 4 double layers of straw tubes. The first and last layer will be installed vertical to the beam direction and the inner two will be shifted by +5° and −5°, respectively.

RICH and ToF Wall The Ring Imaging Cherenkov Detector's favored design is a dual radiator RICH detector, which will allow for pion/kaon/proton separation over a momentum range from 2 GeV/c to 15 GeV/c. The Cherenkov light will be detected by an array of photo-tubes, which will be placed outside the sensitive volume.
The Time-of-Flight (ToF) wall will be made of plastic scintillator, which are read out on both sides. The ToF wall, with an expected resolution of 50 ps, will be placed in distance of about 7 m from the interaction point and allow for pion/kaon and kaon/proton separation up to momenta of 2.8 GeV/c and 4.7 GeV/c, respectively [47]. Similar detectors will also be placed in the field of the dipole magnet — they will allow for the detection of charged particles, which do not leave the magnetic field.

Forward EMC The forward EMC will be a shashlik-type calorimeter, which will be made of 680 mm (corresponding to ∼20 radiation length) long lead-scintillators with a lateral size of 110×110 mm. A higher spatial resolution will be achieved by dividing the scintillators into 4 subareas with a size of 55×55 mm, their readout will be based

on wave-length shifting fibers to which photomultipliers are coupled. In total 351 modules arranged in 13 rows and 27 columns will cover the whole forward acceptance; with similar types of modules energy resolutions of $4\%/\sqrt{E}$ have been achieved.

Forward Muon Detectors Absorber material separated by rectangular aluminum drift tubes, similar to the system of the target spectrometer, placed 9 m away from the interaction point will not only allow for the separation of pions and muons, but also for the detection of pion decays and the energy determination of neutrons and antineutrons.

Luminosity Monitor At small momentum transfers (corresponding to small polar angles) the elastic proton-antiproton scattering is dominated by the exact calculable Coulomb term and can be used for the determination of the time integrated luminosity. 4 layers of silicon micro-strip detectors, which cover the whole azimuthal angle, will measure the angle of each scattered antiproton and so allow for the calculation of the luminosity.

Chapter 4

The BESIII Experiment

The BES experiment has a long ongoing history; the electron positron collider BEPC [50] was operated from 1989 to 2004 at IHEP providing collisions in the τ-charm energy region for the BES [51] and the BESII (starting its operation in 1996) [52] experiment. It was a single ring operated in a single bunch mode a maximum luminosity of about $1 \cdot 10^{31}$ cm^{-2} s^{-1} [50].

After the approval by the Chinese government in 2003, the double ring multi-bunch collider BEPCII has been installed in the tunnel of BEPC. Almost all components have been replaced, e.g. the beam pipes, the vacuum system and the magnets and its power supplies. Also a new positron and electron source, which allows for the injection of a "new" beam without damping the remaining one and thus leading to an increase of the average luminosities has been installed [29].

BEPCII is again running in the τ-charm energy region, covering an energy range of $\sqrt{s} = 2 - 4.6$ GeV; but optimized for a center of mass energy of $2 \cdot 1.89$ GeV.

Parameter	BEPC	BEPCII
cm energy [GeV]	2-5	2-4.6
Circumference [m]	240.4	237.5
RF frequency [MHz]	199.5	499.8
Number of bunches	$2 \cdot 1$	$2 \cdot 93$
Beam current [mA]	35	910
Bunch length σ_z[cm]	$\sim$5	1.5
Bunch size $(\sigma_x \times \sigma_y)$ [μm]	$\sim$840 $\times$ $\sim$37	$\sim$380 $\times$ $\sim$5.7
Crossing angle [mrad]	0	$\pm$ 11

Table (4.1)   A comparison of the design parameters of BEPCII with the one of BEPC [29].

Its design luminosity of 10^{33} cm^{-2} s^{-1} [29], which is about 100 times larger than that of BEPC, allows for the collection of large data samples and thus for high precision studies

at the boundary of the perturbative and non perturbative regime of QCD. Such high luminosities are achieved by high beam currents, by a large and closely spaced number of bunches and by the compression of the vertical beam size with the help of superconducting quadrupole magnets, which are installed adjacent to the interaction point (compare to figure 4.1). Table 4.1 shows a comparison of the main design parameters of BEPCII and BEPC. Moreover, the BEPCII accelerator is also a synchrotron radiation facility; here the electron beam with a current of 250 mA and an energy of 2.5 GeV is used as source of the high fluxes of synchrotron radiation.

Up to now the BESIII experiment has collected remarkable and unique data sets (compare to table 4.2), which allow for studies of the τ-charm sector with an unprecedented precision.

Resonance	J/ψ	$\psi(2S)$	$\psi(3770)$	$\psi(4040)$
	$\sim 1.2 \cdot 10^9$ events	$\sim 0.6 \cdot 10^9$ events	$\sim$2.9 fb^{-1}	$\sim$480 pb^{-1}
Energy	4230 MeV	4260 MeV	4360 MeV	3650 MeV
	$\sim$1.2 fb^{-1}	$\sim$800 pb^{-1}	$\sim$520 pb^{-1}	$\sim$45 pb^{-1}

**Table (4.2)** Some data sets collected by the BESIII experiment up to July 2013.

4.1. The BESIII Detector

A schematic overview of the BESIII detector is given in figure 4.1. The technical choices and design decisions for the detectors have been made according to the expected data rates and the typical event structure: The average momentum expected for charged particles is about 0.3 GeV/c, the most probable photon energy is approximately 100 MeV and the average multiplicities for charged particles and neutral particles are in the order of 4 particles per event [29].

The setup of the BESIII detector is typically for particle experiments nowadays, as the components, which are required for particle identification, are similar: The innermost detector is a drift chamber, followed by a ToF detector or a detector with similar capabilities, and a calorimeter. Those components are usually surrounded by a magnet, the outermost detector are resistive plate chambers. The following subsections in this chapter discuss the different components of the BESIII detector in detail.

4.1.1. Interaction Region

To minimize multiple scattering and secondary interactions of the particles produced in the e^+e^- annihilation, the material around the interaction point (IP), to be more precise, the area within the acceptance of the BESIII detector ($|\cos(\theta)|$<0.93, compare to figure 4.1), has to be reduced as much as possible.
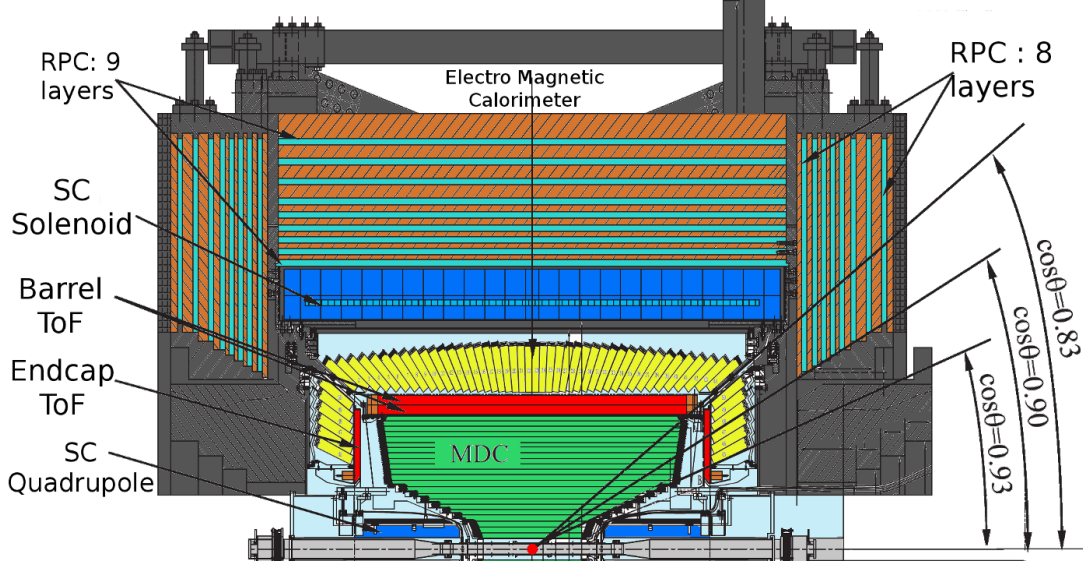
Figure (4.1)   A schematic view of the upper half of the BESIII detector.

The **beam pipe** has to withstand the high heat load ($\approx$ 700 Watt), maintain the high vacuum (the design value is $5 \cdot 10^{-10}$ Torr in the interaction region) and its electric conductivity must be large enough to shield the RF radiation from the beam [29, 53].

As beryllium does meet all the requirements, it is used to construct the inner (thickness = 0.8 mm) and outer (thickness = 0.6 mm) wall of the beam pipe; the 0.8 mm gap between both parts is used for the cooling fluid. The cooling is required as the working temperature of the Mini Drift Chamber (MDC) is restricted to 293.15 K to prevent wire breakages [53]. Cooper extensions are surrounding the beryllium beam pipe outside the sensitive region of the BESIII detector ($|\cos(\theta)| > 0.93$) to shield secondary particles. To monitor the temperature and the radiation level on the beam pipe, twelve radiation detectors (6 on each side) are mounted in the gaps between the copper extensions and the central beryllium beam pipe [29].

Two **luminosity monitors** are placed in a distance of 3.1 m from the IP facing the incoming beams. As the available space is limited, the monitors have to be as compact as possible. The luminosity determination is based one radiative Bhabha scattering ($e^+ e^- \rightarrow e^+ e^- \gamma$): A tungsten target converts the photons into electron-positron pairs, fused silica placed afterwards serves as a scintillation crystal; the scintillation light is finally collected by two photomultipliers (PMT) [54].

Recently one of the luminosity detectors has been replaced by a **Zero-Degree Detector (ZDD)**. This type of detector can not only cover the luminosity determination, but it can be used to tag initial state radiation (ISR) photons. It is a calorimeter, sandwiched of Pb and scintillating fibers, which allows also for the measurement of the energy and the direction of the ISR photons [55].

4.1.2. Mini Drift Chamber

The **MDC** has to fulfill several tasks: It has to allow for the reconstruction of tracks of charged particles traversing the chamber, for the determination of their momentum, charge and energy loss (dE/dx) and should also be used for the level 1 trigger to select events.

The chamber is divided into an inner and outer chamber, which are assembled at the end plates and thus sharing a common gas volume. Both layers are divided again into 11 super layers, where each of these layers contains again 4 layers of sense wires, except of the last one, which contains only 3 [56]. Each sense wire (in total 6,796) made of gold plated tungsten has a diameter of 25 μm and is surrounded by 8 field wires (in total 21,844) made of gold plated aluminum with a diameter of 110 μm. A drift cell of the inner chamber has a width of 12 mm and of the outer chamber a width of 16.2 mm, the average single wire spatial resolution $\sigma_{r\phi}$ is in the order of 135 μm. In order to be able to determine the z-position (the z-axis is the one along the beam direction) the layers 1-8 and 21 to 36 are small angle stereo layers, whereas the other layers are axial ones. At the boundary of axial and stereo layers additional field wires are necessary to compensate drift-distance/drift-time variations caused by the 1 Tesla magnetic field [56, 57]. This configuration and magnetic field strength allows to determine the momentum of charged particles with momenta of 1 GeV/c with a resolution of 0.5%. The spatial resolution σ_z at the IP can be determined with an accuracy of about 2 mm.

The outer radius of the MDC is 810 mm, the radius of the outermost field wire is 789 mm, the inner radius is 59 mm and the innermost field wire is placed at radius of 73 mm [29]. The MDC's maximum z-length is 2.582 m and it covers the polar angle regime of $|\cos(\theta)|$<0.93 and the azimuthal angle range of $0 : 2\pi$; thus the detector has in total an acceptance of 93% of 4π.

Critical for the momentum determination are multiple Coulomb scattering processes in the gas volume, hence a helium based gas mixture (60% He / 40 % C_3H_8) at a pressure of 3 mb above ambit pressure, similar to other experiments [58–61], is being used. It has a radiation length of about 550 m and the primary ionization is adequate for dE/dx measurement with a resolution of better than 6%. This allows for a pion/kaon separation up to momenta of $\approx$ 600 MeV/c at the 3σ level [30].

4.1.3. Time of Flight Detector

BESIII's **ToF** system, placed between the MDC and the Electromagnetic Calorimeter (EMC), is based on plastic scintillators, which are read out by fine mesh photomultipliers. The system plays not only an important role for charged particle identification, but is also used to provide fast trigger signals.

It consist of three parts; two single layer endcaps (made of BC-404 scintillators) and the double layer barrel ToF system (made of BC-408 scintillators) [62]. Due to the compact

design of the BESIII detector, the available space for the barrel part (0.81 m<r<0.93 m) and the endcap part (z<5 cm) is limited [29, 63].

Each layer of the barrel system covers the polar angle regime of $|\cos(\theta)|$<0.82 and consists of 88 trapezoidal plastic scintillation counters with a length of 2,300 mm and a thickness of 50 mm. Two PMTs are placed at each end of the barrel counters and coupled to the scintillator bars by the mean of an 1 mm thick silicone pad. The layers are staggered to avoid dead area between the edges of the two scintillators.

The single layer time resolution was estimated to be 100-110 ps, whereas the double layer design was expected to have a total time resolution of 80-90 ps. The naively expected factor of $1/\sqrt{2}$ between the single and double layer resolution is not met as correlated sources of uncertainties are existing. Only the intrinsic time resolution σ_i caused by the rise time of the scintillation light, the fluctuation of photon arrival time at the PMTs, the transition time spread of the PMTs, and the resolution σ_w, which is caused by the time walk of a fixed threshold discriminator, can be improved by the factor of $\sqrt{2}$ [29]. Additional sources, such as the uncertainty from the global accelerator timing marker, the uncertainty from the determination of the interaction point, the uncertainty from the z-hit position on the scintillator, the uncertainty of the Time to Digital Converter (TDC) measurement and the one from the determination of the flight path length and the momentum of a particle still have to be considered.

The design goals have been achieved, the double layer time resolution for Bhabha scattering events is 78 ps [64]. Figure 4.2(a) shows the measured time resolution of the barrel system depending on the z-hit position of the barrel (the figure was taken from [64]). The worse time resolution in the middle of a scintillator is due to the reduced amount of scintillation light which arrives the PMTs at the end of the scintillator bars [65].

The endcap systems, which cover a polar angle range of 0.85<$|\cos(\theta)|$<0.95, are build of 48 trapezoidal shaped plastic scintillator with a height of 480 mm and a thickness of 50 mm. The width is 62 mm at the bottom and 109 mm at the top [29]. The detectors are placed behind the MDC's endplate. At the bottom, on the front of each scintillator, a 45° cut is used to reflect the light into the PMT, which is attached at the bottom on the back (compare to figure 4.1).

The design time resolution of 110 ps has only be reached for *dimuon* events, the resolution for electrons is around 150 ps. The worse resolution is mainly caused by the interaction of the electrons with MDC's endcap plate [66]. The total time resolution for pions and kaons has also been determined in [66]: It is in the order of 135 ps and thus allowing for a pion/kaon separation at a 2σ level up to momenta of 1 GeV/c (compare to figure 4.2(b)).

Small gaps between the endcaps and the barrel part are required for mechanical support, supply and service structures of the MDC.
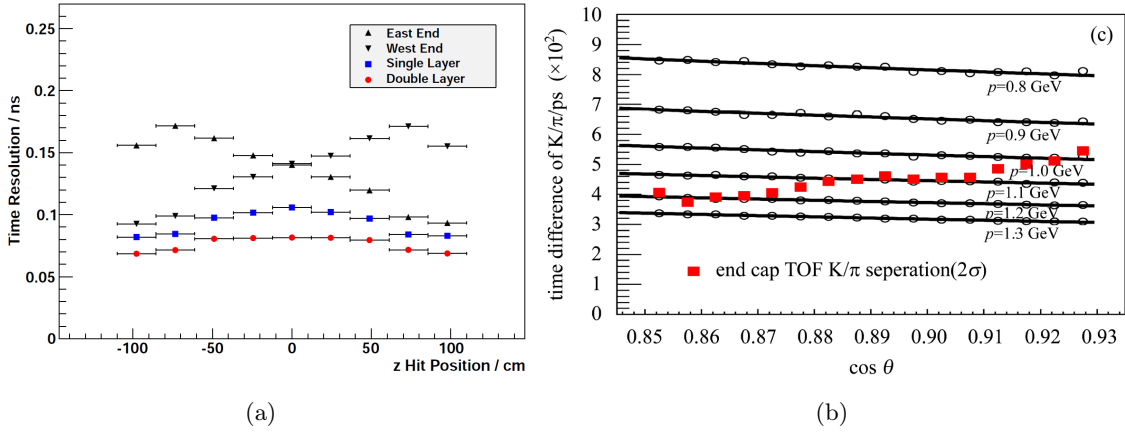
Figure (4.2)   **(a)** shows time resolution of the barrel ToF depending on the z-coordinate ($z = 0$ corresponds to the IP). The time resolution is worse at z=0, as the fewest scintillation photons are collected here. The figure is taken from [64].
(b) shows the time difference of kaons and pions vs. the polar angle θ determined with the endcap ToF system. The red points show the capability of a 2σ kaon/pion separation. The figure is taken from [66].

4.1.4. Electromagnetic Calorimeter

The EMC is the outermost detector which is still within the magnetic field. It is mainly used for the detection of photons from 20 MeV up to about 2 GeV and the electron/pion discrimination; high energy resolution, adequate position resolution and high efficiency are mandatory. It does also provide a fast energy trigger information, which is used to select events.

The EMC consists of a barrel and two endcap parts, which both are build of trapezoidal formed thallium doped cesium iodide (CsI(Tl)) scintillating crystals. The endcap and barrel systems are separated by a 5 cm gap which is required for support, supply and service structures for the inner most detectors. The crystals are tilted about $1.5°$ in ϕ direction and $1.5°$-$3°$ in θ direction (compare to figure 4.1) to avoid that photons escape through the contacting surfaces [29].

The length of a crystal is 28.5 cm (corresponding to 15.1 radiation lengths X_0), the surface at on end is $5.2 \cdot 5.2$ cm^2 and at the other end $6.4 \cdot 6.4$ cm^2. Each crystal, wrapped by a thin reflection material (260 μm Tyvek foil, 25 μm aluminum and 25 μm mylar) [67], is read out by two photodiodes mounted on the top of a crystal. 5,280 crystals arranged in 44 rings with an inner radius of 94 cm build the barrel system and 960 crystals arranged in 6 rings at a distance of ±138 cm from the interaction point build the endcap system. The polar angle covered by the barrel system is $33.5°<\theta<146.5°$ (corresponding to $|\cos(\theta)|<0.83$), the endcaps cover the range of $0.85<|\cos(\theta)|<0.93$.

The energy resolution was measured for Bhabha events at $\sqrt{s}$ =3.686 GeV to be 2.3% in the barrel and 4.1% in the endcap system. For photons the resolution is 2.7% for the barrel and 4.2% for the endcap systems, respectively [68]. The position resolution for photons with an energy of 1 GeV is 6 mm in the barrel region and 9 mm in the endcap region.

4.1.5. Superconducting Solenoid Magnet

The Superconducting Solenoid Magnet (SSM) provides a uniform axial magnetic field with a strength of 1.0 Tesla and allows for the accurate momentum determination together with the MDC. It encloses the 3 innermost sub-detectors; the inner radius, determined by the EMC is $\sim$1.38 m, the outer one 1.7 m. The SSM is cooled with liquid He with a temperature of 4.5 K and has a nominal current of 3,369 A [29]. The material of the flux return yoke, which is segmented into layers (9 in the barrel, 8 in the endcap region) and instrumented with Resistive Plate Chambers (RPCs), is low carbon steel.

4.1.6. Muon Identification System

The main goal of the muon identification system, build of RPCs, is to separate muons from charged pions and other hadrons based on their hit patterns. The system of octagonal shape is embedded in the magnetic flux return and is constructed out of 9 RPC layers in the barrel part (polar angle regime $|\cos(\theta)|$<0.75), where the first layer is placed in front of the innermost steel plate, and out of 8 layers in the endcap region (polar angle regime 0.75<$|\cos(\theta)|$<0.89). Each layer contains a superlayer segment (SL), build of double stack RPCs, summing up in total to 72 SLs for the barrel and 64 for the endcap regime [69]. The thickness of the steel plates is varying from 3 cm up to 15 cm, where the first layer of steel plates are the thinner ones. This ensures that the cut-off momentum for muon detection, which is around 400 MeV/c [29], is as small as possible.

A RPC module is build of two 2 mm Bakelite plates engulfing a 2 mm thick gas gap. To improve detection efficiencies, single gas gaps RPCs are arranged in a two layer structure and embedded in a 32 mm thick aluminum case; the readout strips — their size is varying from 20 mm to 54 mm — are placed in between two RPC modules. With the double layer design the detection efficiency can be enhanced from about 95% up to 98% [29].

As the modules can only measure one spatial coordinate the orientation of the signal strips is alternated for each layer, allowing for the measurement of two spatial coordinates.

The RPC modules are driven in a streamer mode with a gas mixture of $Ar : C_2F_4H_2 : C_4H_{10}$ (50:42:8) with a working voltage of $\sim$8000 V.
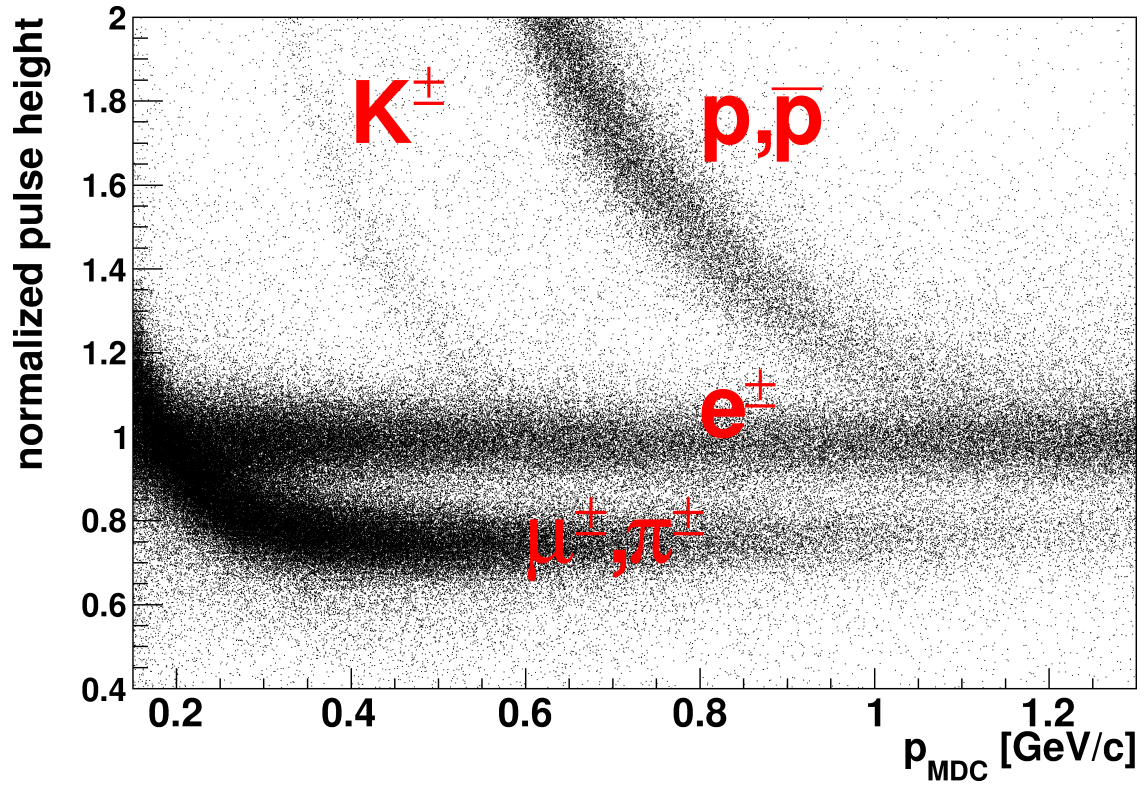
(a)
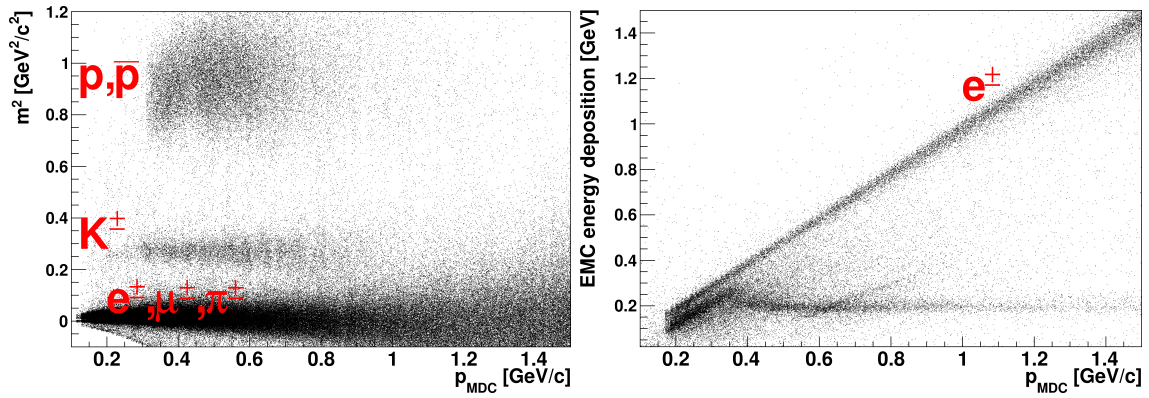
(b)

(c)

Figure (4.3) **(a)** shows the energy loss (normalized pulse height in the MDC) of the particles in the drift chamber vs. the momentum measured in the MDC.
(b) shows the squared mass of a particle determined with the ToF information (compare to equation 4.2.1) vs. the particle's momentum in the drift chamber.
(c) shows a particles' energy deposited in the EMC vs. their momentum.
The data for the plots was taken from a subsample of the $\psi(3770)$ data collected by the BESIII experiment.

4.2. Particle Identification

Particle Identification (PID) plays an important role to produce valuable and reliable analysis results. Electrons and positrons (e$^\pm$), muons ($\mu^\pm$), pions ($\pi^\pm$), kaons ($K^\pm$) and protons (p) and antiprotons ($\overline{p}$) have to be separated, but also of neutral particles (mainly photons (γ)) have to be identified. A good μ/π separation, for example, is required for high precision measurements of the ratio of the decay constants of D$_s$ and D mesons f_D/f_{D_s}. The accuracy of the CKM matrix elements V_{cs} and V_{cd} can be improved with a high reliable electron identification [30].

Each sub-detector provides quite different information for different momentum ranges to determine the particles species. They can be combined by method such as likelihood methods, H-Matrix estimators or artificial neural networks and thus improve the PID performance [70–72].

MDC Figure 4.3(a) shows the normalized pulse height in the MDC (which is proportional to the dE/dx information) versus the momentum of charged particles: In the momentum regime around 0.2 GeV/c $e^\pm$, $\mu^\pm$ and $\pi^\pm$ can not be separated by their (dE/dx) information, though pions and kaons can be well separated up to momenta of about 600 MeV/c. It is also possible to separate electrons and pions which have momenta higher than 0.4 GeV/c, but not electrons from kaons around 0.6 GeV/c. Protons and antiprotons can be clearly identified by their energy loss up to momenta of about 1 GeV/c.

ToF system It is possible to calculate the relative velocity β and eventually the mass m of a particle with the measured time of flight information $t_{me.}$:

$$\beta = \frac{L}{v_c t_{me.}}, \qquad m^2 = p^2 \cdot \frac{1-\beta^2}{\beta^2} \qquad , \tag{4.2.1}$$

with L the corresponding flight path, p the momentum of the particle and v_c the velocity of light. Figure 4.3(b) shows the squared mass distribution versus the momentum of particles in the barrel part.

Again the protons and antiprotons can be separated well. The pion and kaon separation at a 2σ level is possible up to momenta of 0.9 GeV/c for the barrel system [62] with its time resolution of about 80 ps (compare to section 4.1.3). With nowadays available time of flight techniques, the capability of pion/kaon separation of the barrel system can not be enhanced significantly — an improvement could only be gained with a complete new detection technology, e.g. Cherenkov detectors.

The endcap system allows also for a pion/kaon separation at a 2σ level up to 0.9 GeV/c (compare to 4.2(b)). However, due to the longer flight paths and the worse time resolution (compare to section 4.1.3) much more room for improvement is existing.

The capability could be enhanced up to about momenta of 1.4 GeV/c using nowadays technologies; section 5 of this thesis is discussing such an upgrade in detail.

EMC Electrons, positrons and photons produce an electromagnetic shower in the EMC and deposit their whole energy. Their ratio of deposited energy and total momentum is ≈ 1 (compare to figure 4.3(c)) as their masses are so low [10]. Electrons and positrons can be separated from photons with the help of the MDC tracks: Neutral particles do not produce signals within the MDC, as they do not interact with the MDC's gas mixture.

Other minimum ionizing particle (i.e. not electrons and positrons) pass under normal circumstances the EMC and deposit about 0.17 GeV of their energy in the crystals (compare to figure 4.3(c).)

Muon system Most of the hadrons penetrating the EMC will get stuck somewhere in the absorber material of the magnetic field's return joke. They will produce a hadronic shower and a lot of hits near the layers where the interaction did occur [30].
However, muons with a high momentum have a high probability to cross all the layers and are likely to produce only one signal in each of the layers.

4.3. The BESIII Offline Software System

The BESIII Offline Software System (BOSS) [73], developed in object-oriented C++, based on the Gaudi architecture is the offline software for the BESIII experiment and allows for the simulation, calibration, reconstruction and analysis of the collected data.
As the simulation and reconstruction software developed for the MRPC is implemented into this system, the following section provides a brief introduction into the major BOSS packages:

Simulation Packages They are based on Geant4 (GEometry ANd Tracking) [74] and allow for the complete simulation of the BESIII sub-detectors and the simulation of the response of the individual components. They include a variety of generators allowing for accurate simulation of charmonium production and the subsequent decays. Eventually, the digitized output of a real event is delivered.

Calibration Packages This part of the software enables the reconstruction algorithms to obtain the calibration constants for all the sub-detectors produced by the associated calibration algorithms.

Reconstruction Packages They fulfill the central part for the offline data processing. Tracks are created from the individual hits of the MDC, the dE/dx information required for

PID is calculated, the reconstructed tracks are matched with the information of the outer lying detectors, the deposited energy in the EMC is determined, etc.

Analysis Packages This part of the software provides the central algorithm for the analysis of the data. It provides not only tools to determine the vertex and the particle species (PID), but also kinematic fitting tools, which can help to improve the momentum and mass resolution.

Chapter 5 _____

Multigap Resistive Plate Chambers - A Possible Upgrade for the BESIII Experiment

As already discussed in section 4.2 the endcap ToF system has still a lot of room for improvement: To enhance the capability of pion/kaon discrimination from momenta of 1.0 GeV/c up to 1.4 GeV/c at a 2σ level, the total time resolution (including tracking, etc.) has to be reduced to less than 80 ps. Such time resolutions can be already achieved with nowadays available MRPC technology, which is used in various high energy physics experiments [75–77].

It is discussed to replace BESIII's actual endcap ToF detector with a system based on MRPCs in the year 2015.

The following sections address the development of the simulation and reconstruction software for the planned upgrade, but also the functional principal of MRPCs itself.

5.1. Multigap Resistive Plate Chambers

RPCs are relatively simple devices: They consists of a gas volume bounded by resistive plates, covered with electrodes on the outer surface [78]. Passing charged particles will create electron-ion pairs and the electrons will form an avalanche when they are accelerated towards the anode by a sufficiently strong electric field. However, the time resolution of such a device is far to bad to be used as ToF detector. Shrinking the gap size would improve the time resolution, but some particles may not create an avalanche large enough to be detected.

Rising the electric field strength will also lead to an improved time resolution, since the signal will have a much faster rise time. However, this causes a rate problem, since the large amount of charge produced in the gas volume has to be discharged through the resistive plates [79].

MRPCs can solve the dilemma: They are gas based avalanche detectors composed of a stack of resistive plates, with a high bulk resistivity (between 10^{11} and 10^{13} Ωcm), which are separated by the mean of spacers, creating a series of equal sized gas gaps. Electrodes

are connected only to the outer surface while the inner plates are kept electrically floating. The small gap-size and a high field strength lead to a very good time resolution and a small amount of charge, the large amount of gaps increases the efficiency ($> 99\%$). The signal collected by the pickup electrodes is the sum of all gaps, thus the signal is large enough to be "easily" detectable.

5.1.1. Basic Information about the Planned Upgrade

The MRPC modules planned to be used for the ToF upgrade at the BESIII detector are double stack MRPCs with in total 12 gas layers of a thickness of 0.22 mm (Figure 5.2) and 24 readout channels. They will be operated at a voltage of about 14 kV (corresponding to a field strength of ≈ 112 kV/cm) with a gas mixture of 90 % $C_2F_4H_2$, 5 % SF_6 and 5 % iso-butane. The signal produced by the MRPC is a differential signal reducing the noise significantly.

The modules will be placed in an aluminum frame. At each side of a frame an additional box containing the front-end electronics (FEE) is mounted (Figure 5.1). The 4 connectors at the bottom of the box are the inlet (outlet) for the gas mixture and the high voltage. To overcome the dead area arising due to the additional box, each endcap will contain two layers of modules. A single layer will be 25 mm thick and contain 18 modules and thus have 432 readout channels.
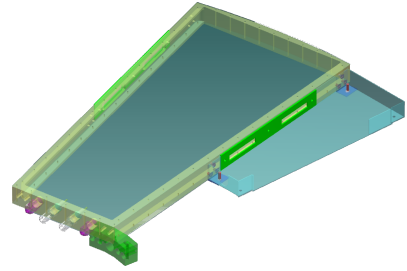

Figure (5.1) The aluminum frame and the box for the FEE.

Until now, two different versions of the MRPC's design are being discussed, the *single end readout* and the *double sided readout* version. They only differ in the design of the readout strips (Figure 5.3). The double sided readout version has the advantage that the hit position can be reconstructed without the information of others detectors, whereas the single end read out version would require additional information from other detectors, but would have a lower multi-hit rate per strip [80].

The FEE planned to be used is based on NINO chips [81], that are ultra-fast and low-power front-end amplifier/discriminators designed specially for MRPCs (developed at CERN). NINO allows not only for the time measurement, but also for charge measurement via time-over threshold. The detection threshold can be varied between ~15 fC and ~150 fC. The NINO signals will be fed to a TDC based on HPTDCs (High Performance TDCs) [82], providing a time resolution of 25 ps [83]. This chip has also been developed at CERN.
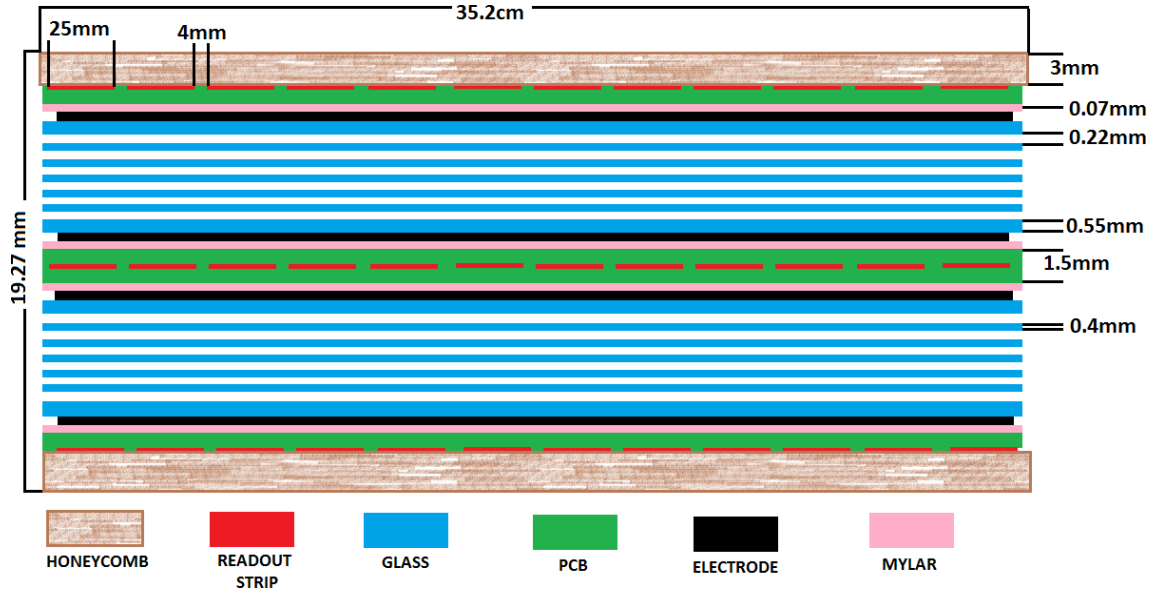
Figure (5.2) Sketch of the MRPC planned to be used for the ToF upgrade at BESIII. PCB is the acronym for printed circuit board.
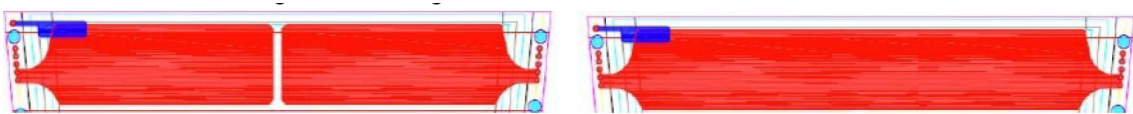
Figure (5.3) The readout strips in one row for the single end readout version (left) and for the double sided readout version (right). The single end readout version will have a lower multi hit rate, but additional information from other detectors is required to obtain the impact position of a signal creating particle.

5.2. Simulation of the MRPC System in BOSS

The simulation packages contain not only the geometric definition of the detector but also the digitization models, which are responsible to simulate the detector's characteristics, such as efficiency, resolution and signal as realistic as possible using the information provided by Geant4. The digitization process should be as fast as possible to reduce the computing time for Monte Carlo (MC) simulations.

5.2.1. Implementation of the Geometry

The geometry and material properties of the MRPC detector are implemented by means of Geant4's concept of *logical* and *physical volumes*. Logical volumes manage the representation of detector element properties, physical volumes the spatial positioning. The detector's solid modeling is done with the help of predefined solids, such as boxes, tubes, cones, ... Different *Boolean* operations, like *union, intersection or subtraction,* for solids do exist to describe peculiar shapes in a simple and intuitive way.

A list of the used materials for the MRPC's implementation and the design drawings of the individual components can be found in the appendix A.1. Figure 5.4(a) shows the final implementation in Geant4 for a single layer; the second layer is shifted by 10° respective to the first one. Figure 5.4(b) shows the Geant4 representation of a single module and its interaction with a penetrating pion.

5.2.2. The Digitizer

The process of signal production in a MRPC is at first glance relatively simple: A particle crossing the detector ionizes the gas; the electrons create an avalanche in the electric field, moving towards the anode. The movement of the electron induces a signal into the readout strips, which can be detected.

For each step Geant4 provides in its tracking algorithm (a step is an interaction of the respective particle with matter, e.g. the detector's material) information like momentum of the particle, energy loss, number of electron-ion pairs, etc. The number of electron-ion pairs is used as input for the avalanche simulation.

Avalanche Simulation

Electron multiplication in high electric fields can be described using statistical language [84]. Starting from one electron at $x = 0$ the probability to have n electrons at $x + dx$ is:

$$P(n) = \begin{cases} k\frac{\bar{n}(dx)-1}{\bar{n}(dx)-k} & \text{for } n = 0 \\ \bar{n}(dx)\left(\frac{1-k}{\bar{n}(dx)-k}\right)^2\left(\frac{\bar{n}(dx)-1}{\bar{n}(dx)-k}\right)^{n-1} & \text{for } n > 0 \end{cases} \tag{5.2.1}$$

(a)　　　　　　　　　　　　　　　　　(b)
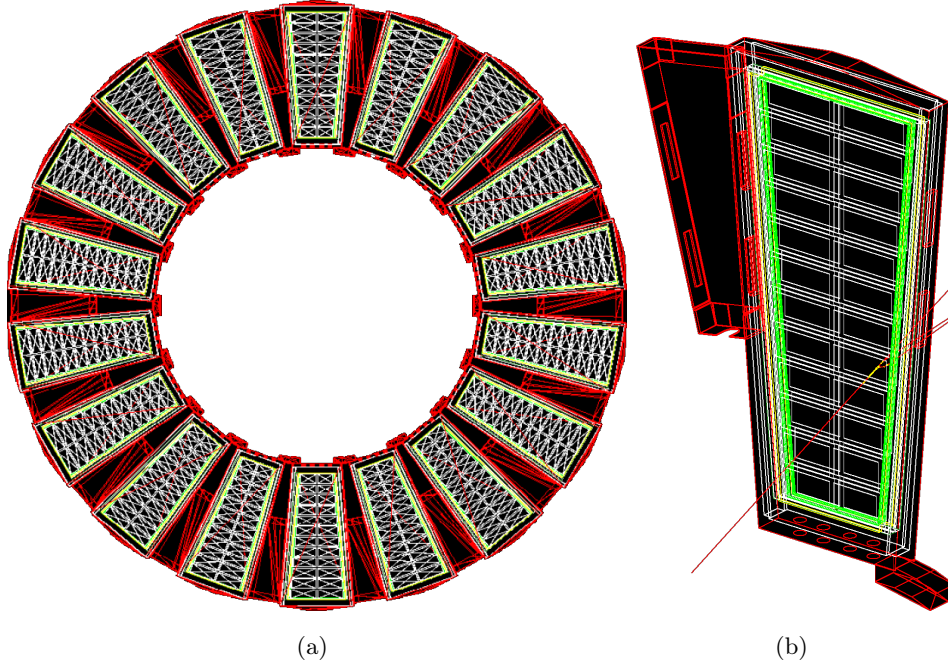
Figure (5.4)　**(a)** shows the Geant4 representation of a single layer of the MRPC upgrade. Between two MRPC modules an aluminum box is mounted, which will contain the FEE. **(b)** shows a single MRPC module and the box which will contain the FEE. A particle penetrates the module (red line), interacts (yellow) and the particle and secondaries are leaving the module.

with $\bar{n}(dx) = exp((\alpha - \eta)dx)$, $k = \eta/\alpha$, α the Townsend-coefficient and η the attachment coefficient. Equation 5.2.1 can only be employed, when $\alpha \neq \beta$ and $\alpha \neq 0$. As the MRPC is operated with a high electric field ($\sim$110 kV/cm), this is always the case (compare also to figure 5.6(a)).

To generate random numbers according to equation 5.2.1, one draws a random number s out from a uniform distribution in the interval $(0, 1)$ and calculates

$$n = 0; \qquad s < \frac{\bar{n}(dx) - 1}{\bar{n}(dx) - k}$$

$$n = 1 + int\left[\frac{1}{ln(\frac{\bar{n}(dx)-1}{\bar{n}(dx)-k})}ln\left(\frac{(\bar{n}(dx)-k)(s-1)}{(k-1)\bar{n}(dx)}\right)\right]; \text{ else },\qquad (5.2.2)$$

int is the conversion into an integer number [85].

The simulation of the avalanche itself is based on the 1D-model [85]:

1. A gap of the MRPC is divided into N steps of a size dx and the electron-ion-pairs are distributed accordingly to the information provided by Geant4.

2. For each single electron, the number of electrons at the distance $x + dx$ is calculated by drawing random numbers according to equation 5.2.2.

3. The second step is repeated until all electrons have left the gap.

The evaluation of the logarithm for large numbers of electrons in equation 5.2.2 is time consuming. To speed up the simulation process, for sufficient large numbers of electrons (=150, compare to figure 5.5) a different technique is applied.

The number of electrons at the distance $x + dx$ is calculated by drawing a random number from a Gaussian distribution with mean μ and standard deviation σ given as

$$\mu = n(x)\overline{n}(x) \qquad \text{and} \qquad \sigma = \sqrt{n(x)}\hat{\sigma}(dx) \quad . \tag{5.2.3}$$

$\hat{\sigma}$ is the variance of the distribution 5.2.1:

$$\hat{\sigma}(x)^2 = \frac{1+k}{1-k}\bar{n}(x)(\bar{n}(x) - 1) \quad . \tag{5.2.4}$$

However, this simple model has a serious drawback: It does not consider space charge effects of the avalanche itself and an avalanche will grow until is leaves the gap [86]. To take into account such effects, a simple cutoff is applied. As soon as the avalanche exceeds a certain number of charge carriers ($1.5 \cdot 10^7$ electrons per avalanche [86]), the electron multiplication stops. This rude cutoff does not affect the main characteristics, such as efficiency and time resolution, of the MRPC. They are only sensitive to the early stage of the avalanche, where space charge effects can be neglected [87].

Signal Induction into the Readout Strips
The current induced by moving charge carriers into a readout strip can be calculated utilizing Ramo's theorem [88]:

$$I(t) = E_w v_d Q N(t) \quad , \tag{5.2.5}$$

with v_d the drift velocity of the charge carriers, Q the charge of the charge carriers and $N(t)$ the number of electrons at a certain time t in the avalanche. E_w is the weighting-field, which can be expressed as [89]:

$$E_{\text{weight}} = \frac{1}{n_{gap}d_{gap} + ((n_{gap} - 1)d_{in} + 2d_{out})/\epsilon_{\text{Glass}} + 2d_{\text{Mylar}}/\epsilon_{\text{Mylar}}} \quad . \tag{5.2.6}$$

Here n_{gap} is the number of gaps, d_{gap} the width of the gap, d_{in}, d_{out} and d_{Mylar} the thickness of inner, outer resistive plate and Mylar tape. ϵ is the relative permittivity

of the respective material (Figure 5.2).

Input Parameter from External Sources

In order to perform the avalanche simulation, the Townsend-coefficient α, the attachment-coefficient η and the drift velocity of the electrons is required. They depend on the gas mixture, the applied voltage and condition such as temperature and pressure. They are not provided by Geant4, but can be calculated by a software called *MAGBOLTZ* [90, 91].

The simulation's results for a gas mixture of 90 % $C_2F_4H_2$, 5 % SF_6 and 5 % iso-butane at standard conditions for temperature and pressure for different electric field strengths is shown in figure 5.6(a) and 5.6(b).

The average energy per electron ion pair w for the gas mixture is required at simulation level, too. This value depends on the energy of the incident particle [92], but approaches a certain value above a certain threshold (usually a few MeV [93]). The type of the high energy particle does not influence this value, the difference between the particle species is usually less than $\sim$2 eV [92]. The w value for $C_2F_4H_2$ is unknown yet (SF_6: $\sim$35.5 eV [94], iso-butane: $\sim$23 eV [95]), but electro negative gases with a high primary ionization production and a small free path for electron capture have w-values of about 50 eV [95]; eventually the w-value was set to be 40 eV in the simulation.

Figure 5.5 shows the avalanche simulation in a single gas gap: Two avalanches start both with one electron at different positions. Initially, fluctuations in the avalanche size can be observed, but as soon as the number of electrons is larger than $\sim$50, the avalanche evolves exponentially. Here, the total amount of charge carriers is limited to $1.6 \cdot 10^7$. The Townsend and attachment-coefficient have been chosen according to the simulation's result at 110 kV/cm.

Uncertainties in the Simulation Process

The uncertainties of the avalanche simulation arising due to different ionizations in the gas gaps and fluctuations in the electron multiplication are described by the model and are in the following called *intrinsic time resolution*. Figure 5.7(a) shows the intrinsic time resolution as a function of the applied electric field strength. At the intended operating voltage the intrinsic time resolution is $\sim$20 ps.

Further uncertainties from electronic components are not directly considered in the simulation process and have to be added manually; that are: The TDC's resolution (27 ps [96]), the uncertainty on which gap has been hit (10 ps), the jitter from the leading edge of the NINO chip (accordingly to figure 5.7(b)) and the resolution from further electronic components and cables (20 ps).
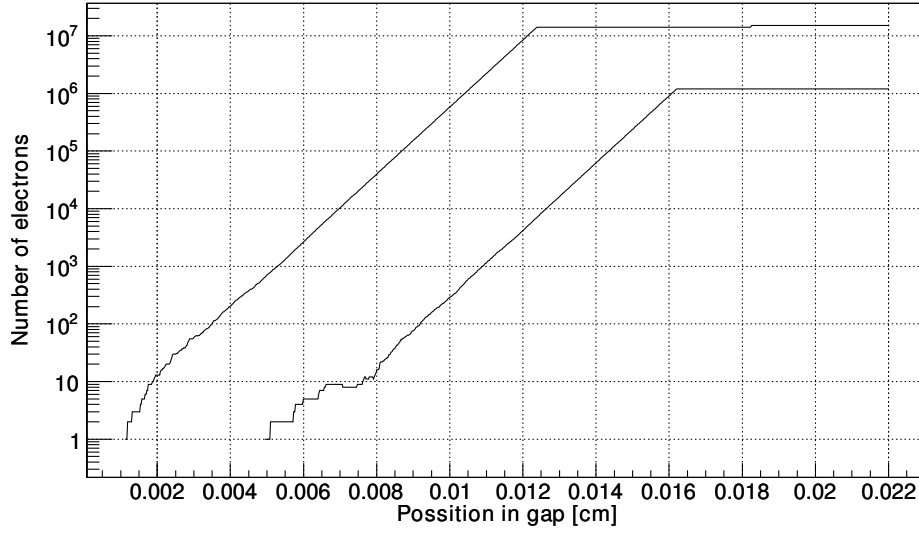
Figure (5.5)   Evolution of two avalanches in one gas gap following equation 5.2.2.
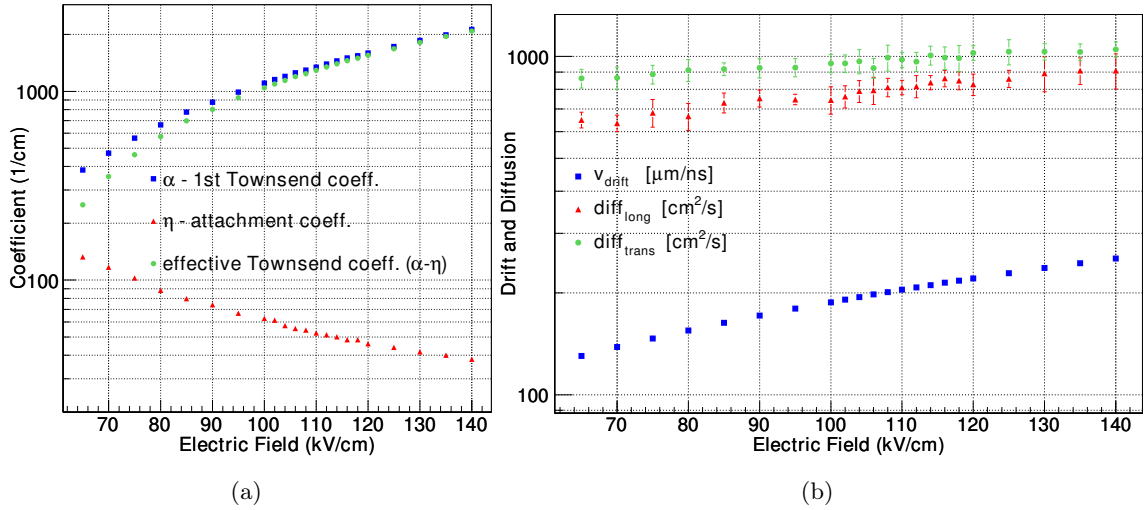
Figure (5.6)   **(a)** shows the Townsend-coefficient α (blue), the attachment-coefficient η (red) and the effective Townsend-coefficient (green) $(= \alpha - \eta)$ for the MRPC's gas mixture under normal conditions simulated by MAGBOLTZ. **(b)** shows the drift velocity (blue) and the avalanche's transversal (green) and longitudinal (red) diffusion-coefficient for the MRPC's gas mixture under normal conditions simulated by MAGBOLTZ.

(a)   (b)
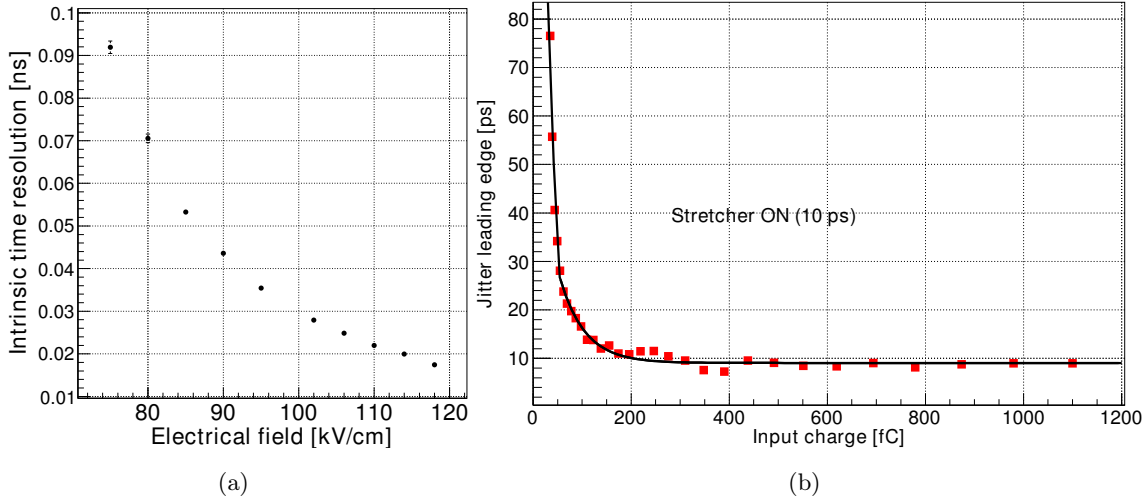
Figure (5.7)   **(a)** shows the intrinsic time resolution: The threshold crossing times of the avalanches have been fitted with a Gaussian, the given value is the standard deviation. **(b)** shows the jitter of the leading edge produced by the NINO chip [97].

The threshold crossing time of the avalanche, which is used as measured result in the simulation, is smeared by these additional uncertainties.

Charge to Pulse Length Conversion

The NINO chip converts the induced charge into the pulse length of the produced signal, the Time Over Threshold (TOT). There is a clear relationship between induced charge and pulse length as shown in figure 5.8(a). The induced charge, calculated with Ramo's theorem [88], is simply converted into the pulse length by the corresponding relating function. The jitter of the pulse length is depending on the input charge (compare to figure 5.8(b)) and is also considered in the simulation: The time of the falling edge is smeared by this value.

5.2.3. Comparison of Simulation Results and Measured Data

The MRPC prototypes have already been objected to intensive tests at the BEPCII E3 beamline at Institute of High Energy Physics (IHEP), including a test with protons with a momentum of ∼600 MeV/c [98].

The test data has been compared with simulated data. The simulated setup did consist of one MRPC detector and two reference detectors (plastic scintillators), which have been placed in front and after the MRPC. The reference detectors are important for the efficiency determination. Only when a particle produces a signal

(a)

(b)
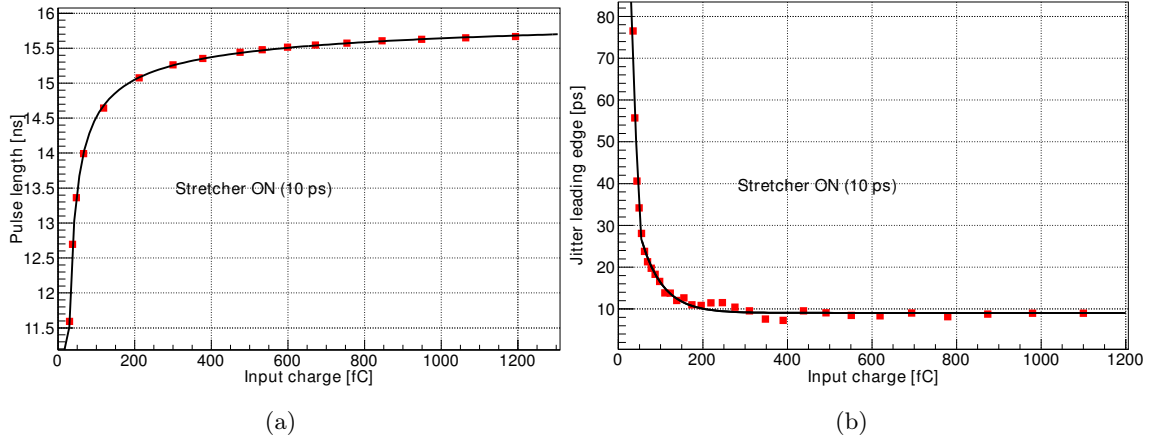
Figure (5.8)   **(a)** shows the relationship of input charge and the produced pulse length for the NINO chip [97]. The pulse length is stretched artificially by the NINO chip by 10 ps. **(b)** shows the jitter of the falling edge produced by the NINO chip [97].

(a)

(b)
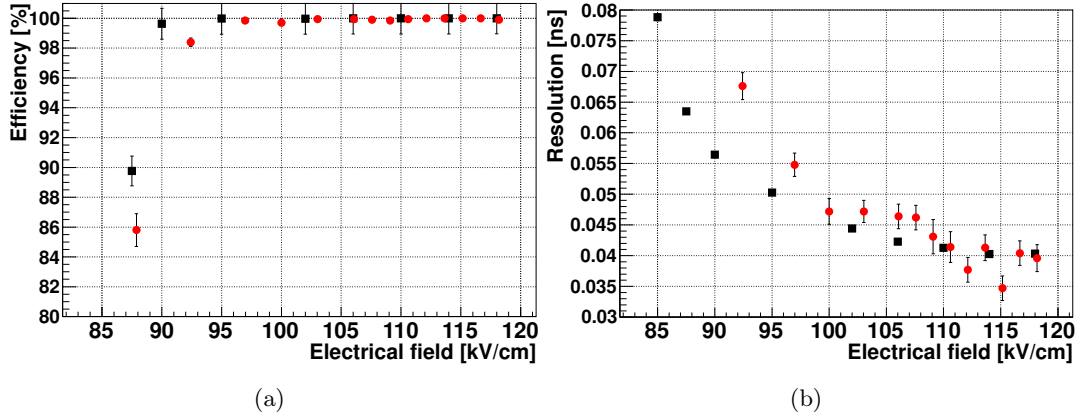
Figure (5.9)   Comparison of measured data (red) and simulated (black) data for protons with a momentum of about 600 MeV/c [98]: **(a)** shows the time resolution as a function of the applied electrical field strength and **(b)** shows the efficiency of the MRPC detector.
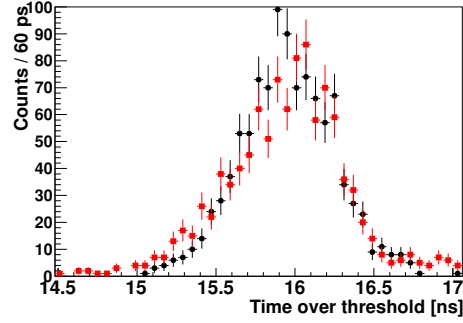
in both scintillators, the events is considered. All parameters at the simulation level are set as described in the previous chapters, for the time over threshold conversion an uncertainty of 0.3 ns is assumed.

Figure 5.9(a) shows the comparison of the simulation results for the efficiency with the one for the beam test. Both, the simulated and measured efficiency do agree with each other.

The threshold for signal detection for the MRPC itself was set to 70 fC, similar to the one in the beam test. Figure 5.9(b) shows the comparison of the simulated time resolution with the measured one as a function of the applied electrical field.

The simulated data matches the measured one for field strengths higher than 100 kV/cm, for field strength lower than this value, the time resolution is underestimated.

Figure (5.10) Comparison of the TOT spectra at E=112 kV/cm (measured data in red).

In this area recombination effects of electron-ion pairs in the early stage of the avalanche which aren't considered in this simple model may play an important role. A comparison of the time over threshold for data and simulation at an electrical field strength of 112 kV/cm is shown in figure 5.10. From the comparisons one may conclude that the model is able to reproduce the measured data for the planned working electrical field strength of ~112 kV/cm.

5.3. Reconstruction Software of the MRPC System in BOSS

The reconstruction procedure for a ToF system involves not only the provision of the measured time of the system itself, but also the matching of the time signals with the information provided by the inner and outer sub-detectors. The measured time will be corrected with information gained from the time-amplitude correlation and with the help of the reconstructed hit position on the readout strips. Information about the energy loss of the particles can be provided from the measured information as well.

5.3.1. Time-Amplitude Correction

The average threshold crossing time for the *avalanche* is correlated with the time over threshold measurement, which decodes the induced charge information. This correlation can be used to perform the time-amplitude (TA) correction (also known as *walk correction*). The correlation has been extracted from the simulation and is fitted with a polynomial (compare to figure 5.11). The fitted distribution is eventually used to correct the measured time information.
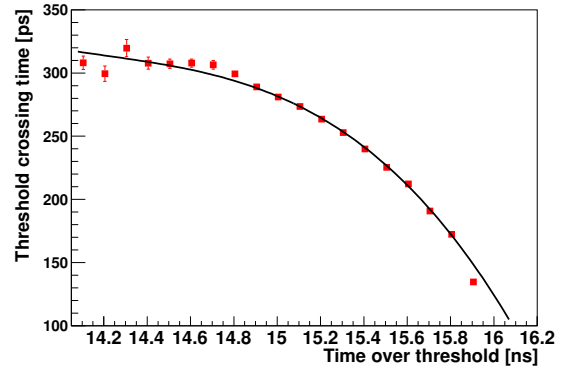

Figure (5.11) Fitted TA correlation, the data points (red) have been extracted from the simulation.

Figure 5.12(a) shows the uncorrected time information for pions with momenta between 1.1 and 1.3 GeV/c, the mean value of the distribution is around 195 ps. After applying the correction the mean value is as expected ∼0 ps (compare to figure 5.12(b)). This correction helps to determine the true ToF information (without the "contamination" of the time required for the signal production) and improves also the resolution of the corrected distribution by ∼ 5 ps.

5.3.2. MDC-ToF Matching

The information from the ToF system has to be matched with the tracks, which have been reconstructed by the MDC. The matching is based on an algorithm extrapolating reconstructed MDC-tracks to the outer sub-detector systems by means of Geant4's tracking and stepping algorithms; the algorithm considers magnetic deflections and ionization energy loss as well.

(a)

(b)
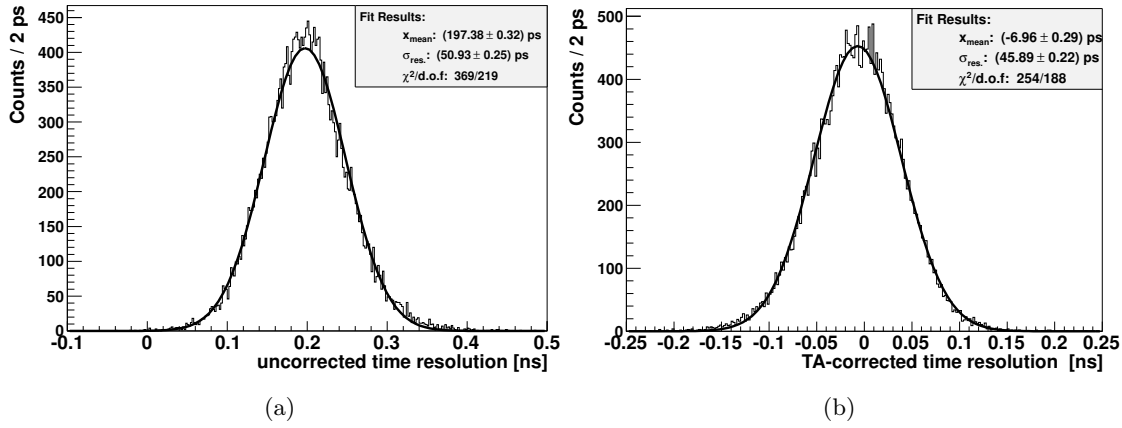
Figure (5.12) **(a)** shows the measured time information for pions with momenta between 1.1 and 1.3 GeV/c without applying the time-amplitude correction, the mean value of the distribution is at about 195 ps. **(b)** After applying the correction the whole distribution is shifted towards the 0 ps, the resolution improves by 5 ps, too.

It is searched for signals from the MRPC detector around the extrapolated position. The area to be searched for signals, in the following referred to as neighborhood, can be varied. For the *double sided readout* version, five different sets of neighborhoods are available, for the *single end readout* six different sets are considered (compare to figure A.5.). The smallest in area is the neighborhood set with the smallest number (set 1), the largest in area the one with the largest number (set 5 or 6 respectively). If more than one adjacent strips are available, the one with the largest deposition of charge, i.e. the longest time over threshold, is selected.

The neighborhood sets are introduced, since the "real" track might be scattered, e.g. at MDC's endcap plate material, and thus the extrapolated one might not be at the same position, but the ToF information is still suitable and should not be discarded. The size of the neighborhood set strongly affects the reconstruction efficiencies. Table 5.1 and 5.2 show the reconstruction efficiencies (extrapolated tracks with associated ToF information divided by the total number of extrapolated tracks) for the different neighborhood sets and different decay modes:

- $\Psi' \to \chi_{c1}\gamma$, $\chi_{c1} \to K^+\pi^- K^0\pi^0$. The subsequent decays of the neutral pion and kaon are: $\pi \to \gamma\gamma$ and $K^0 \to \pi^+\pi^-$. All particles decay accordingly to a phase space model.

- Single charged pions, shot into the endcaps: $0.85 < \cos(\theta) < 0.94$, $0 < \phi < 2\pi$, 0.05 GeV/c $< |\mathrm{p}| < 1.45$ GeV/c

- $J/\psi \to \rho\pi$, 33% decay into $\rho^0\pi^0$, 33% decay into $\rho^+\pi^-$, 33% decay into $\rho^-\pi^+$.

The subsequent decays are accordingly to [10].

As expected, the largest neighborhood results in the highest reconstruction (matching) efficiency and comes closest to the efficiency of the current ToF version, which uses a similar technique for track matching (the area of the largest neighborhood is almost equal to the one used by the current ToF system). The introduction of larger sets does not improve the reconstruction efficiency significantly anymore. For all further studies the neighborhood set with the highest reconstruction efficiency has been used.

Eff. (%)	Set 1	Set 2	Set 3	Set 4	Set 5	Set 6	"current ToF"
charged π	76.9	81.0	83.3	85.5	85.4	87.5	90.0
$\Psi' \rightarrow \chi_{c1}\gamma$	64.7	68.5	70.3	72.7	72.4	75.4	74.8
$J/\Psi \rightarrow \rho\pi$	62.0	66.3	68.6	71.1	70.8	74.2	75.48

Table (5.1) MDC-ToF endcap matching efficiency for the different neighborhood sets and reactions for the 'single end readout version'. The total errors for each number are $< \pm 2\%$.

Eff. (%)	Set 1	Set 2	Set 3	Set 4	Set 5	"current ToF"
charged π	59.95	74.26	79.41	81.31	89.82	90.02
$\Psi' \rightarrow \chi_{c1}\gamma$	49.35	63.28	68.51	69.65	78.89	74.78
$J/\Psi \rightarrow \rho\pi$	45.14	59.34	65.27	65.95	76.15	75.48

Table (5.2) MDC-ToF endcap matching efficiency for the different neighborhood sets and reactions for the 'double sided readout version'. The total errors for each number are $< \pm 2\%$.

5.3.3. Determination of the Readout Strip's Signal Transition Time

The impact position of a particle causing a signal in the MRPC module is a priori unknown, i.e the time required for the induced signal to propagate through the readout strips is unknown, too. This results in an additional uncertainty, which depends on the geometrical size of the readout strips. For the *single end readout* MRPC version, this uncertainty is varying between 93 ps and 153 ps for the smallest and largest readout strip, respectively (this are the worst cases assuming a signal velocity of $0.75c$). This is larger than the total expected resolution and implies that a correction has to be applied to fulfill the design goal of <80 ps.

For the *double sided readout* version a correction is relatively straight forward, as a 1-dimensional hit position and an approximation to the signal transition time $t_{trans.}$

can be calculated from the timing information read out on both sides:

$$t_{trans.} = \frac{k/v_{sig.} + \Delta t}{2} \qquad , \qquad (5.3.1)$$

with k the strip length, $v_{sig.}$ the signal velocity in the readout strip, and Δt the difference between the measured time information on both sides of the readout strip. However, another method, and even applicable for the *single end readout* version, is existing. The extrapolated track can be used to determine the impact position on the readout strips and so allow for the calculation of the expected signal transition time. However, this method can only be applied, when the readout strip, which the extrapolated track is pointing at has caused the signal. The uncertainty originating from the extrapolated hit position is far smaller than the uncertainty due to the pad size.
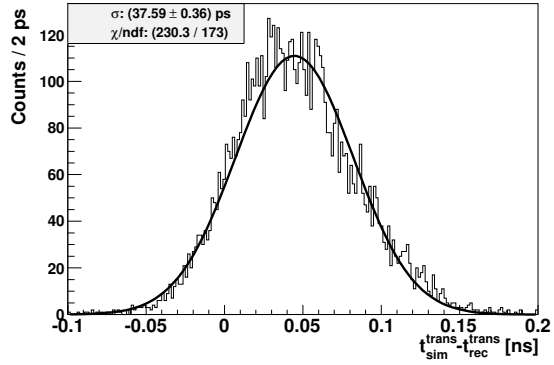
If it is impossible to use the information from the extrapolated track, the transition time can be estimated accordingly to the geometrical pad size of the fired readout strip. Figure 5.14(a) shows the difference of the simulated and reconstructed transition time for events where the extrapolated track information is usable.

Figure (5.13) Difference in simulated and reconstructed transition time for events, where the double sided readout information was usable.

The distribution has been fitted with a double Gaussian. One Gaussian (covering 87% of the signals) has the resolution σ_s of about 18 ps, corresponding to a position resolution of about 0.4 cm.
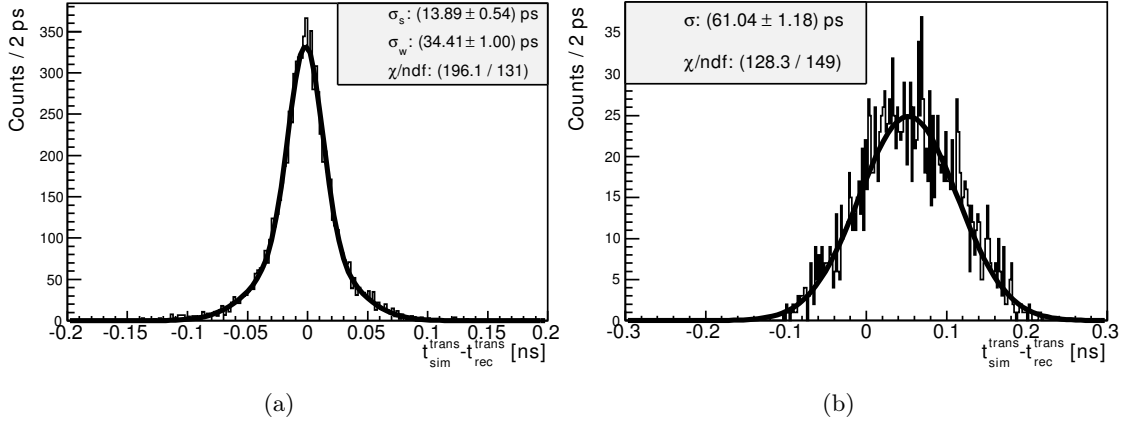
The second Gaussian has a resolution σ_w of about 34 ps. The resolution of the transition time, determined with the time information read out on both sides of a readout strip, and calculated according to formula 5.3.1, is ~ 38 ps (compare to figure 5.14(b)). The resolution for a correction based on the average pad size is shown in figure 5.13; it is around 61 ps.

Hence, to obtain the best results concerning the resolution the priority of the determination of the transition time should be as follows:

1. If the extrapolated track information is available, the transition time should be calculated using this information.

(a)   (b)

Figure (5.14) (a) shows the difference between the simulated transition time in the readout strips and the reconstructed one for events (single charged pions, 0.05 GeV/c<p<1.45 GeV/c), where the extrapolated track information was usable. **(b)** shows the same difference, but for events where the correction based on the average geometrical strip size did have to be applied.

Neighborhood set	Set 1	Set 2	Set 3	Set 4	Set 5	Set 6
$\varepsilon_{cor.}$ (%)	71.5	67.7	65.4	64.2	63.9	62.3

Table (5.3) Percentage of correct extrapolations $\varepsilon_{cor.}$ for pions shoot in to the endcaps $(0.87 < \cos(\theta) < 0.92)$ with a momentum between 0.05 GeV/c and 1.45 GeV/c for the *single end readout* version. The number shrinks for larger neighborhood sets, as the amount of matched candidates is rising.

2. If the extrapolated track information is not available, but the *double sided readout* version is used, the information on the transition time should be determined according to formula 5.3.1

3. If both other methods fail, the correction on the transition time should be determined by the geometrical size of the readout strips.

Table 5.3 shows how often the extrapolated track information can be used for the *single end readout* version; the number shrinks for larger neighborhood sets as the amount of matched candidates is rising. The same information for the *double sided readout* version is given in table 5.2. The differences in the signal's propagation time arising due different *cable lengths* is neglected in this discussion here: It is constant and can be determined by time calibration (the uncertainty of the calibration is included in *further components*, compare to section 5.2.2).

### 5.3.4. Energy Loss in the MRPC System and Neutral Tracks

Particles crossing the MRPC system loose a certain amount of energy by interacting with the MRPC's material. Especially for particles, which deposit their whole energy in the EMC (electrons, positrons and photons) the value might be of interest as a correction of the EMC measurement.

The energy loss of particles and its relation to the signals produced in the MRPC system has been studied in BOSS. The results are shown in figure 5.15 and 5.16.

For electrons and positrons two different clusters are observed (compare to figure 5.16(a)) — a cluster at around 5 MeV energy loss and large time over thresholds, and a rising distribution starting from small time over thresholds — they seem to have different origins. Figure 5.16(b) shows the energy loss vs. the time over threshold for charged particles, which have crossed two different, but adjacent readout strips: The rising distribution is caused by particles producing a signal in two adjacent read out strips.

Photons can also cause a signal in the MRPC system; the signal producing process relies mainly on pair production. Their energy loss is also related to the signal strength (TOT) (compare to figure 5.15).

The decision, whether a track is neutral or not is based on the extrapolated track information: If no extrapolated track is pointing at a MRPC strip, the MRPC measurement is assumed to originate from a neutral particle.
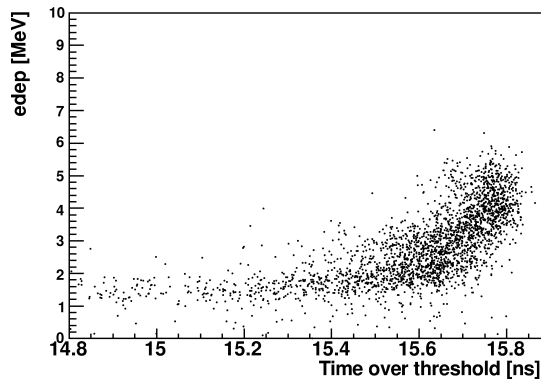

Figure (5.15) The energy loss of photons vs. their produced signal in the MRPC detector.

The energy loss for the three different situations have been fitted and are calculated based on those curves and the measured time over threshold. The calculated energy loss can be used to correct the energy measurement of electrons, positrons and photons.

5.4. Pion and Kaon Separation Power

As already discussed in section 4.2 the main task of the ToF system is to allow for pion and kaon separation starting from momenta of about 0.6 GeV/c. This section is studying the improvement in pion and kaon separation with the planned upgrade. The study has been performed in BOSS 6.6.2. Pions and kaons with

(a)   (b)
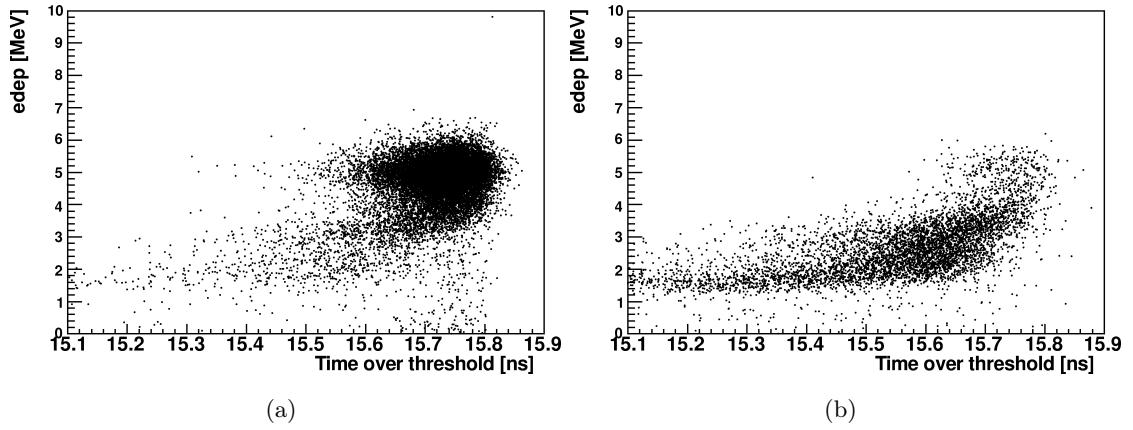
Figure (5.16)   **(a)** The energy deposition of electrons and positrons (0.05 GeV/c < p < 1.45 GeV/c) within the MRPC system related to their time over threshold, two different distribution are prominent. **(b)** The energy loss of electrons and protons when a readout strip and an adjacent readout strip have a signal.

momenta between 0.5 GeV/c and 1.5 GeV/c are analyzed with the current ToF system and with both versions of the planned MRPC upgrade. All the corrections discussed in section 5.3 have been applied.

Figure 5.17 shows the difference of measured time of flight $t_{meas.}$ and expected time of flight $t_{exp.}$. $t_{exp.}$ has been calculated assuming the particle was a pion or a kaon, respectively. The expected time of flight is calculated as

$$t_{exp.} = \frac{L}{\beta c} = \frac{L}{\frac{p/m}{\sqrt{1+p^2/m^2}} \cdot c} \quad .$$ (5.4.1)

Here β is the relativistic velocity of the particle, c the velocity of light, p the momentum and m the mass of the particle. L is the distance traveled (extrapolated track length), which has been determined by a reconstruction algorithm. It is obvious from figure 5.17, that the MRPC detector can separate the two particle hypotheses much better: the two distribution do not overlap as strongly as for the current ToF detector version.

The measured time differences have been fitted with a Gaussian distribution and the standard deviation (resolution) has been plotted in figure 5.18 versus the measured momentum and $\cos(\theta)$. Here, the resolution contains contributions both from the MRPC detector and from the track finding algorithms.

The resolution for high momentum tracks is ∼80 ps, for smaller momenta the resolution deteriorates due to the worse resolution of the tracking algorithm (low momentum particle will scatter more often). However, for low momenta the distributions

(a)

(b)
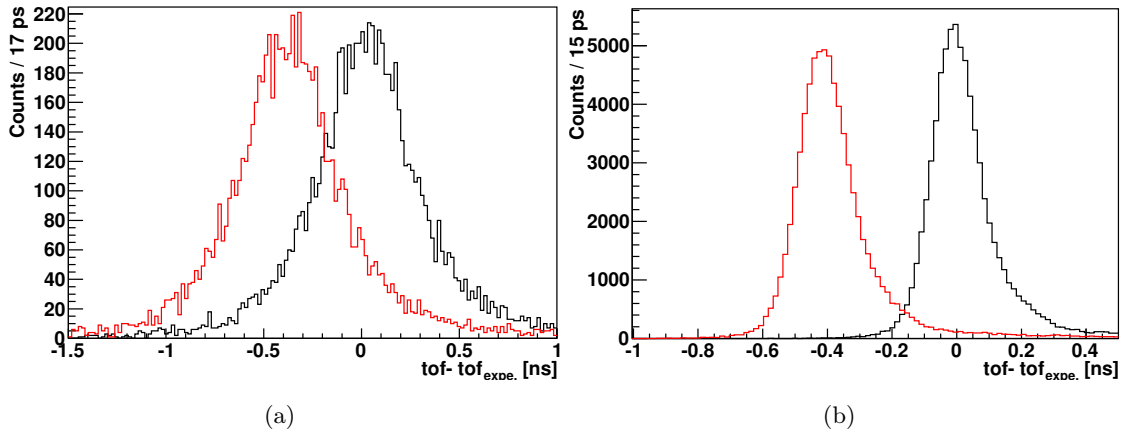
Figure (5.17) The measured time of flight minus the expected time of flight (red expectation value for kaons and black for pions) for simulated pion events with a momentum between 1.1 GeV/c and 1.2 GeV/c for the **(a)** current ToF system and **(b)** single end readout MRPC upgrade.

will be much better separated, and a clear pion and kaon separation is still possible. The pion and kaon separation power can be expressed with the separation power N_σ, which is defined as

$$N_\sigma = \frac{|x_K - x_\pi|}{\sqrt{\sigma_K^2 - \sigma_\pi^2}} \quad . \tag{5.4.2}$$

Here x_i is the fitted mean of the difference of measured time of flight and expected time of flight and σ_i the corresponding width of the distribution. A separation power of $N_\sigma = 2$ corresponds to a misidentification probability of 7.9%, a separation at 95% confidence level corresponds to $N_\sigma = 2.33$.

Figure 5.19 shows the separation power as a function of the momentum for the actual ToF detector compared with the separation power of the simulated MRPC upgrade (figure 5.19(b) for the *single end read* out version and in figure 5.19(a) for the *double sided readout* version).

The improvement with the MRPC upgrade is clear visible. Both simulated versions will allow for a pion/kaon separation up to momenta of 1.4 GeV/c at a 95% confidence level.

(a)   (b)
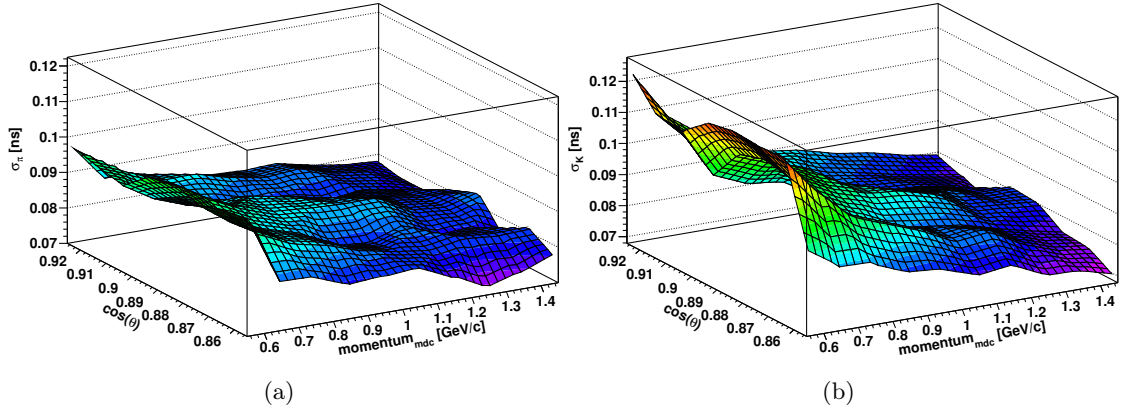
Figure (5.18)   The resolution σ of the measured time of flight minus the expected time
of flight distribution as a function of $\cos(\theta)$ and the momentum of the particles for **(a)**
simulated pion events and **(b)** simulated kaon events (single end readout version). The
resolution rises for smaller momenta as the resolution of the track reconstruction algorithm
becomes worse.

(a)   (b)
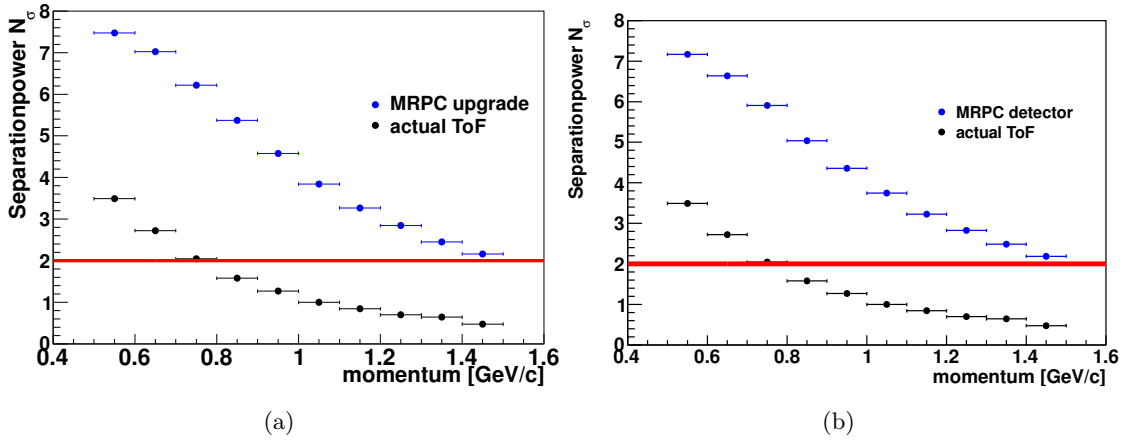
Figure (5.19)   The separation power of the current ToF detector compared with the *single
end readout version* **(a)** and the *double sided readout version* **(b)** of the simulated MRPC
upgrade as a function of the momentum of the particle. A separation power of $N_\sigma = 2$
corresponds to 7.9% misidentification of kaons and pions. A separation at a confidence
level of 95% ($N_\sigma \hat{=} 2.33$) is possible up to momenta of $\sim$1.4 GeV/c.
Both simulated versions of the MRPC upgrade achieve the design goals and have a com-
patible performance.

Chapter 6

The Analysis of $\psi(3770) \rightarrow \mathrm{p\overline{p}}\pi^0$

The partial decay width of the $\psi(3770)$ decay to $\mathrm{p\overline{p}}\pi^0$ is required as input parameter for the estimation of the cross section $\sigma(\mathrm{p\overline{p}} \rightarrow \psi(3770)\pi^0)$, which is from great importance for the $\overline{\mathrm{P}}\mathrm{ANDA}$ experiment, with a model to be presented in section 6.10. This chapter describes the determination of the partial decay width using the data collected by the BESIII experiment in the energy interval between 3.65 and 3.82 GeV.

The relevant quantities will be extracted from a fit on the measured cross sections. For the determination of the cross section it has to be considered, that the data has to be corrected for efficiencies, initial state radiation effects and background events from different sources. Appropriate corrections have to be applied for all these points.

6.1. Data Sets, Software and Monte-Carlo Simulation

The data analysis was performed with the aforementioned BOSS software version 6.5.5. The Monte Carlo production is based on the $\mathcal{KK}$ MC generator [99] and the EvtGen package [100]. $\mathcal{KK}$ MC utilizes predictions of the electroweak standard model for the process $e^+e^- \rightarrow f\overline{f} + n\gamma$, where f is a fermion (μ, τ, u, d, s, c, b). It is used in BOSS to generate the charmonium resonance including effects from ISR and beam energy spread; though, the ISR effects are not considered in the Monte Carlo production of this analysis. The decay of the charmonium state itself is modeled with EvtGen. However, EvtGen can handle also the whole generation, which is utilized for off-resonance data production.

A list of the Monte Carlo event sets, used in this analysis to determine the a priori unknown detection efficiencies, is given in table 6.1. More Monte Carlo event sets have been produced to analyze background channels and to determine the radiative corrections. They are presented in the following chapters.

The on-resonance data and the data for the line shape used in this analysis was

$\sqrt{s}$ [GeV]	Generator	Parent particle	Decay model	# Events
scan	real data	—	—	$\mathcal{L} \approx 63 \text{ pb}^{-1}$
3.650	real data	—	—	$\mathcal{L} \approx 44 \text{ pb}^{-1}$
3.773	real data	—	—	$\mathcal{L} \approx 2916 \text{ pb}^{-1}$
3.65	BesEvtGen	Vpho	PHSP	1 m
3.744	KKMC	$\psi(3770)$	PHSP	1 m
3.753	KKMC	$\psi(3770)$	PHSP	1 m
3.757	KKMC	$\psi(3770)$	PHSP	1 m
3.766	KKMC	$\psi(3770)$	PHSP	1 m
3.773	KKMC	$\psi(3770)$	PHSP	1 m
3.778	KKMC	$\psi(3770)$	PHSP	1 m
3.791	KKMC	$\psi(3770)$	PHSP	1 m
3.806	KKMC	$\psi(3770)$	PHSP	1 m

Table (6.1) Data sets that are used in the analysis of $\psi(3770) \to p\bar{p}\pi^0$. The abbreviation *Vpho* means vector photon and is the parent particle usually used to generate decays at a certain energy via a virtual photon. *PHSP* is the shortcut for phase space.

collected by the BESIII detector in the running periods in the years 2010 and 2011. The data of the line shape scan comprises the energy range from 3.744 GeV to 3.806 GeV. Additionally off-resonance data, accumulated at an energy of 3.65 GeV, is used. A brief overview of all the data sets is also given in table 6.1.

6.2. Event Selection Criteria

The decay analyzed involves two charged particles, the proton and the antiproton, and the neutral pion, which decays dominantly into a pair of photons. Hence, event selection criteria for neutral and charged particles are required.

### 6.2.1. Initial Event Selection Criteria and Particle Identification

- **Charged Tracks** All charged tracks are reconstructed from their MDC information. Following cuts have been applied:

  - The point of the closest approach for each track in direction to the beam axis is required to be less than ± 10 cm of the interaction point and in the plane perpendicular to the beam axis ± 1 cm of the interaction point.

  - Two charged tracks with a net charge of zero are required.

- **Neutral Particles** The neutral particles are reconstructed from their EMC information and their "missing" MDC information. Following criteria are applied to select the photon candidates:

  - The EMC signal has to originate within 0 and 700 ns after the collision.

  - To suppress background and noise the energy deposited in a cluster has to be at least 25 MeV in the barrel region ($|\cos(\theta)| < 0.8$) and at least 50 MeV in the endcap region ($0.86 < |\cos(\theta)| < 0.92$).

  - To reject photons produced due bremsstrahlung, the angle between a positive charged track and the photon candidate has to be larger than $10°$. To exclude photons from the antiproton annihilation a more stringent cut of $30°$ is chosen for negatively charged tracks.

  - The amount of reconstructed photon candidates has to be larger or equal two ($N_\gamma \geq 2$).

- **Particle Identification** Protons and antiprotons are identified using the information of the ToF detector and their specific dE/dx energy loss information in the drift chamber. Both information are combined and a PID hypothesis is calculated for protons, pions and kaons. The hypothesis with the largest probability is eventually assigned to the track. Proton (antiproton) candidates have to fulfill:

  - $\mathcal{P}(\text{proton}) > \mathcal{P}(\text{kaon})$ && $\mathcal{P}(\text{proton}) > \mathcal{P}(\text{pion})$.

Figure 6.1(a) shows the number of photons after applying the initial event selection criteria to a subsample of the simulated $\psi(3770) \rightarrow p\overline{p}\pi^0$ events at the center of mass energy of $\sqrt{s}=$3.773 GeV (compare to table 6.1). More than 45% of all events contain three or more photons, even though only two can come directly from the π^0's decay. More than 95% of those additional photons arise from the antiproton annihilation and are not suppressed by the cut on the angle between proton (antiproton) and photon. Figure 6.1(b) show the comparison of the number of photons (normalized) for the simulated Monte Carlo events at 3.773 GeV and data collected at that energy. The Monte Carlo events match the trend of the collected data rather well, but small discrepancies arising in events with 2, 3 and 4 photons.

It is important to note that these event selection criteria will contaminate the data with different decay channels, e.g. $\psi(3770) \rightarrow p\overline{p}\pi^0\gamma$. The contamination of background sources similar to the one mentioned here have been studied and will be discussed in detail in section 6.6. The issue of choosing the correct photon pair for the π^0 reconstruction has to be taken into account, too, and is addressed in the following section.
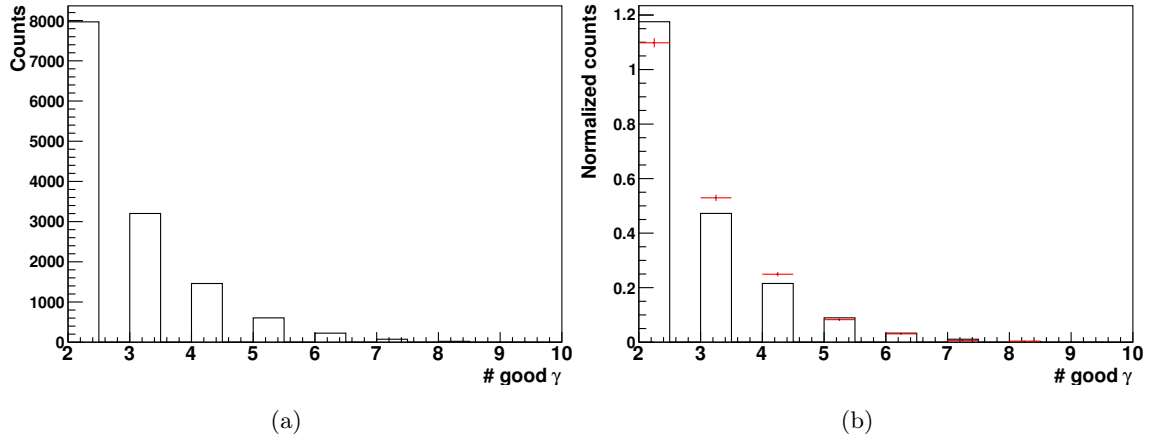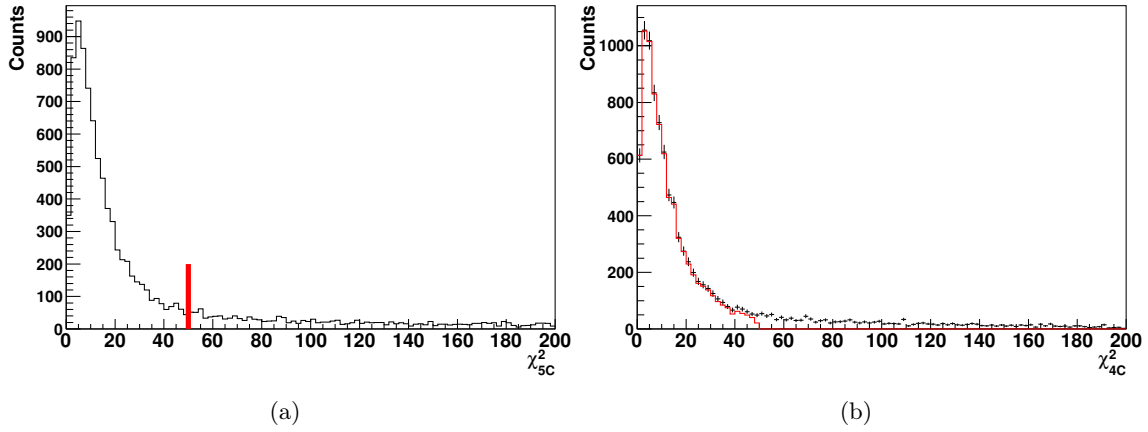
Figure (6.1) **(a)** shows the distribution of the number of photons per event in a Monte Carlo events sample for the decay of $\psi(3770) \rightarrow p\bar{p}\pi^0$. **(b)** shows the comparison of this sample and data, which has been collected by the BESIII detector (red), after the final event selection. The trend is matched well, but discrepancies can be observed for events with $N = 2, 3, 4$ photons.

6.2.2. Correct Photon Pair Combination

The correct photon pair has to be picked up to reconstruct the π^0 meson. Several constraints on the photons arising from the decay of a π^0 are existing: They have to be back-to-back in the frame of reference of the π^0, the combined invariant mass of both photons should be the mass of the π^0, etc.

A simple way to select the correct photon pair, which considers also the initial event structure, is a kinematic fit with 5 constraints (in the following abbreviated as 5C-fit). The constraints chosen for the fit are the initial 4-momentum and the information on the π^0 meson. The 4-momentum vectors of the proton, the antiproton and every combinations of photons are taken into account for the fit. The best combination — the one with the smallest χ^2 — is chosen for the π^0 reconstruction. The χ^2 distribution for the fit is shown in figure 6.2(a).

To verify, that the fit chooses the correct photons, the reconstructed photons of the Monte Carlo events have been compared with their Monte Carlo Truth (MC-Truth) information. As this information is stored in an independent collection, the MC-Truth particles have to be assigned to the reconstructed tracks: The matching of both has been performed with the help of the absolute 3-momentum information of the π^0 and the opening angle of the two photons in the laboratory frame. Figure 6.3 shows both distributions (for positive and negative matches), which have been used for matching the MC-Truth and reconstructed track information.

(a) (b)

Figure (6.2) **(a)** shows the χ^2 distribution of the 5C-fit. The red line indicates the cut chosen in the final event selection criteria. **(b)** shows in black the χ^2 distribution of the 4C-fit. The red curve is also the χ^2 distribution of the 4C-fit, but under condition that the event passes the 5C-fit with $\chi^2_{5C} < 50$. Events, which do pass the 4C-fit, but not the 5C-fit have mainly a χ^2 larger than 40, i.e. a tighter cut on χ^2_{4C} will also enhance the correct photon selection rate of the 4C-fit.

Eventually, one can conclude that the efficiency of choosing the correct photon pair combination for the 5C-fit is **(99.25±0.09)%**.
The given error is the binomial one, which takes into account the correlation of the amount of selected and total events. It is given as $\Delta\varepsilon = \sqrt{\varepsilon(1-\varepsilon)N}/N$, with ε the efficiency and N the number of events [101].
An alternative approach employs the event selection with a 4C-fit taking as constraint only the initial 4-momentum. Here, only in **(96.41±0.18)%** the correct photon pair combinations are found. Events passing the 4C-fit, but not the 5C-fit have mainly χ^2 larger than 40, i.e. a tighter cut on χ^2_{4C} will also enhance the correct photon selection rate of the 4C-fit (compare to figure 6.2(b)).
Concerning the total amount of correct events, the 5C-fit is more efficient: 49.6% of the events will pass the 5C-fit, whereas only 48.6% will pass the 4C-fit.

6.2.3. Final Event Selection Criteria

The cut-flow of the analysis is shown in figure 6.4. The first cut applied is a cut on the polar angle θ of the charged tracks. It does consider the geometrical size of the MDC: $|\cos(\theta)| < 0.93$.
The two upper left plots show the transversal and total momentum for the protons and antiprotons after applying this cut. A cut on the transversal momentum, $p_{trans} > 300\,\mathrm{MeV/c}$, ensures that Monte Carlo events and reconstructed data will not differ too
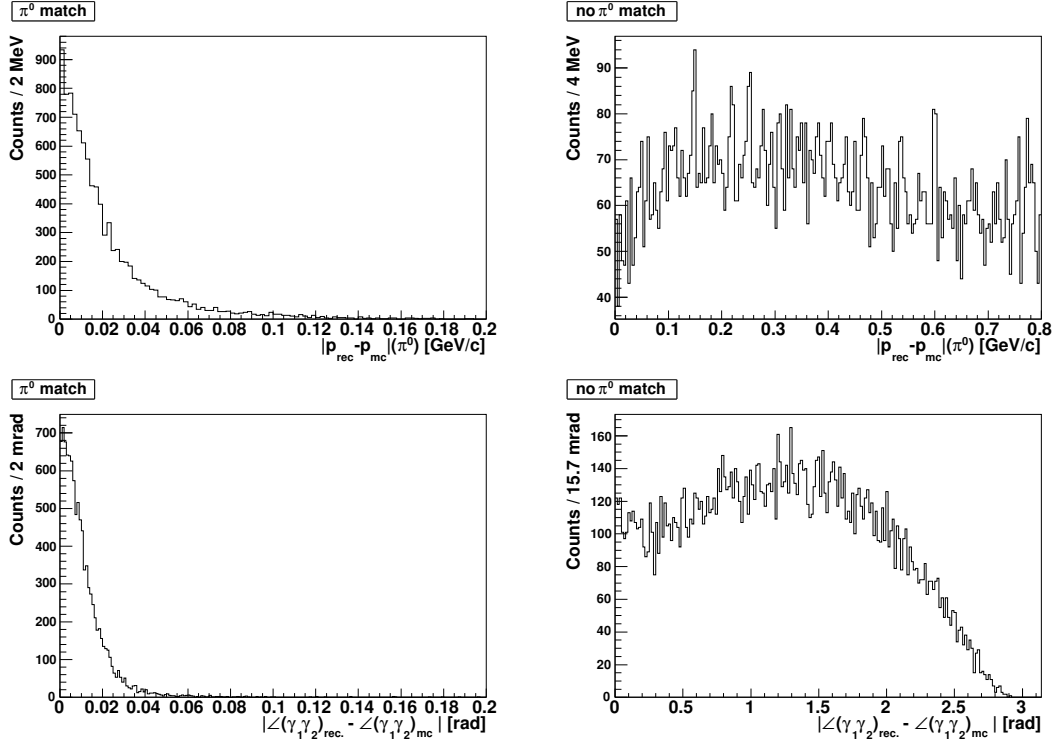
Figure (6.3)   The upper left plot shows the difference between the momentum of the MC-Truth π^0 and the π^0, which has been reconstructed according the 5C-fit selection. The upper right plot shows the same difference, but for a wrong combination of photons, not chosen by the 5C-fit criteria. The lower plots show the difference of the opening angle of the photon chosen (not chosen, right figure) by the 5C-fit and the MC-Truth photon.
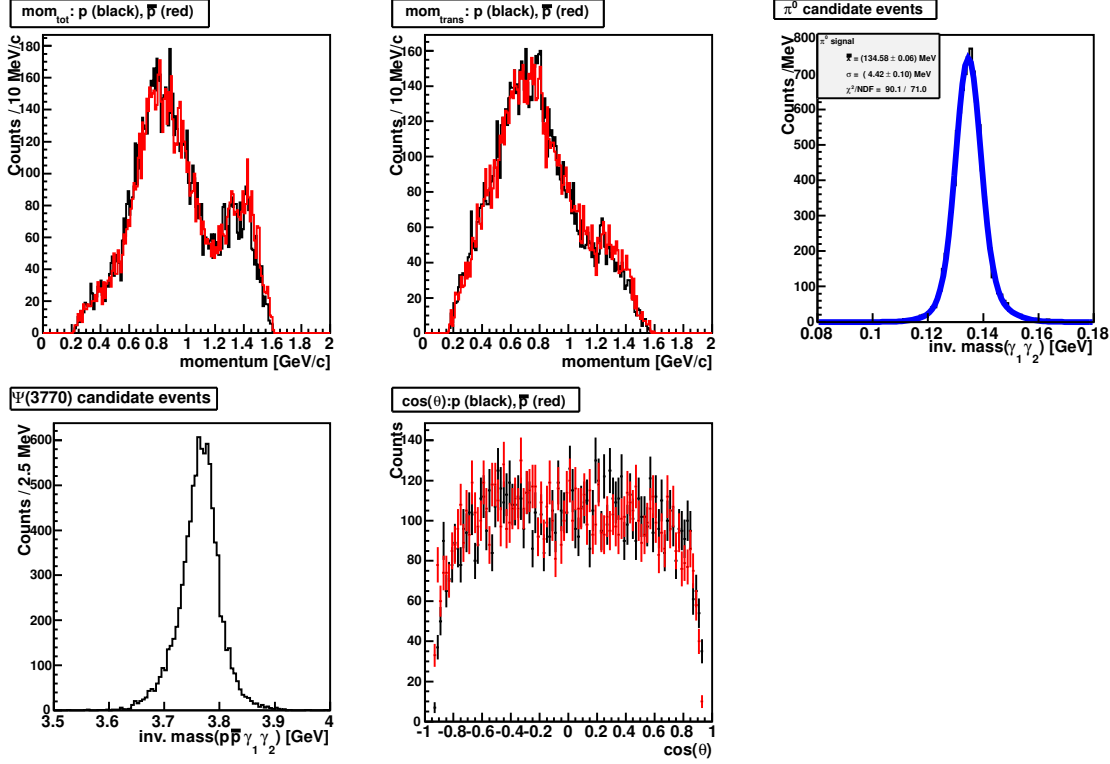
Figure (6.4) The both upper left figures show the reconstructed momentum and the transverse momentum for protons (black) and antiprotons (red) after applying the cut $|cos(\theta)|<0.93$ (data). The upper right plot shows the fitted π^0 mass distribution after performing the 4C-fit and applying the cut $\chi^2_{5C} < 50$ and a cut on the transverse momentum of the proton and antiproton ($p_{trans} > 300$ MeV/c); the $cos(\theta)$ cut is used as well. The lower left figure shows the mass distribution of the selected candidate events after applying additionally a 3σ cut onto the π^0 mass distribution. The lower right plot shows the $cos(\theta)$ distribution of charged tracks (protons in black and antiprotons in red).

much and thus smaller systematic errors can be assumed. This is especially important for the estimation of tracking and PID efficiencies of protons and antiprotons, as for transversal momenta smaller than 300 MeV/c strong discrepancies between data and MC are observed (compare to section 6.7). The amount of events removed by this cut is ~4%.

Additionally a cut on the χ^2 distribution of the 5C-fit has been applied : $\chi^2_{5C} < 50$. This cut is motivated in the following section.

The upper right figure shows the fitted π^0 mass distribution after the 4C-fit and after applying the three cuts. The center of the Gaussian distribution is determined by the fit to (134.61±0.07) MeV and the standard deviation to $\sigma = (4.51 \pm 0.11)$ MeV. Eventually, a 3σ cut on the invariant mass distribution of the π^0 mass is applied. The lower left plot in figure 6.4 shows the distribution of the $\psi(3770)$ candidate events after applying all the cuts. The distribution shown is the one of the unfitted 4-vectors, which pass the fit and the different cuts. The lower right figure shows the $\cos(\theta)$ distribution of the charged tracks.

A comparison of Monte-Carlo events and real data, which is presented in section B.1, reveals a good agreement between both sets.

6.3. Efficiency Correction

Without the knowledge of the reconstruction efficiency the determination of the correct branching ratio for the analyzed decay channel is impossible. The efficiency can be calculated from a Monte-Carlo sample, when all intermediate states and their angular distributions are known. As this information is not available for the decay channel analyzed, a different method has to be utilized. The relevant degrees of freedom n of the system will be determined, each degree of freedom will be again divided into bins and a n-dimensional reconstruction efficiency matrix will be calculated from an arbitrary Monte-Carlo data set by the ratio of reconstructed data and MC-Truth data, where reconstructed data means all data which pass the whole chain of event selection criteria [102–104].

Three decay products (p, $\bar{p}$, π^0) have 12 degrees of freedom (d.o.f). Since the initial state is known, four d.o.f can be removed (4-momentum conservation). Three further d.o.f can be removed as the masses of the decay products are known (after PID). Three more d.o.f can be neglected (the *Euler*-angles), if the decay plane is isotropic (which would imply that the initial state is unpolarized) or the efficiency does not depend on those d.o.f. However, the $\cos\theta$ distribution of the π^0 of data and MC sample does not agree well (compare to figure B.1).
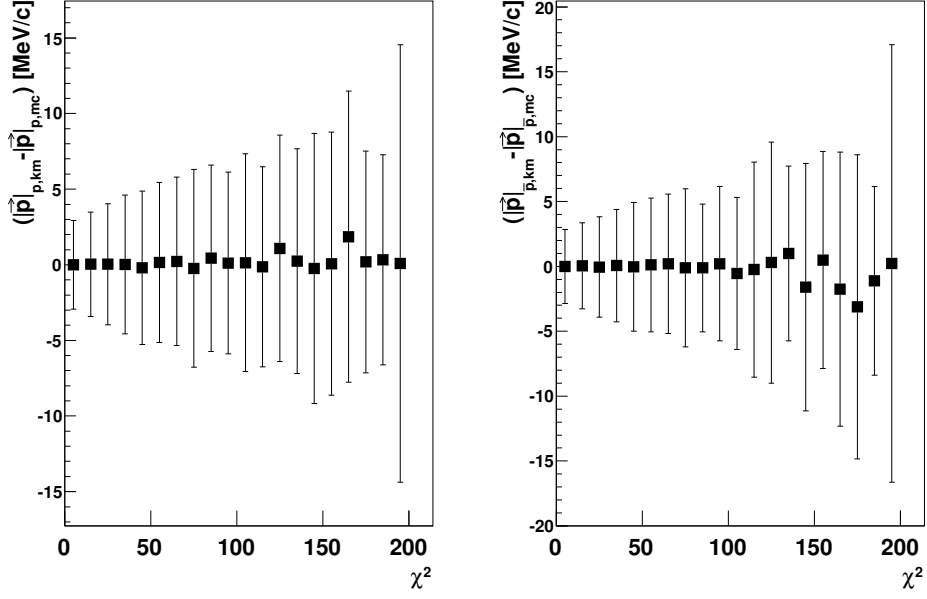
Figure (6.5) (left) Difference of the MC-truth 3-momentum ($\vec{p}_{mc}$) and the reconstructed 3-momentum after the 5C-fit ($\vec{p}_{km}$) for protons, (right) for antiprotons, as a function of the χ^2 of the 5C-fit. The error bars are the standard deviations σ from the fitted Gaussian distribution.

This discrepancy is arising due to polarized intermediated states (e.g. nucleon resonances) in the decay process and might influence the detection efficiency. In order to extract the correct detection efficiency, the MC sample has to be tuned according to the data. Therefor, the observed distribution in data has been fitted with a function $\propto \beta(1 + \alpha \cos^2 \theta)$ and the MC sample was adapted according to this fit result ($\beta = 0.89 \pm 0.02$, $\alpha = 0.55 \pm 0.08$ and $\chi^2/\text{n.d.f} = 44.02/48$). The detection efficiency can now be determined correctly. A sample with the tuned $\cos \theta$ distribution is shown in figure B.2. A comparison of other quantities for collected data and Monte Carlo events reveals a good agreement (compare to section B.1).

Eventually, the efficiency can be determined considering only two d.o.f, which are chosen as $m(p\pi^0)$ and $m(\bar{p}\pi^0)$. These are the invariant mass combination required for a *Dalitz plot*. They describe the whole dynamic of the decay process and take into account the change of the detection efficiency with a change of the kinematic region.

However, this method can only be applied if the MC-Truth data is in the same bin of the Dalitz plot as the reconstructed data. If this does not hold, the efficiency will be calculated wrong and the whole method is obsolete. A simple check has been performed using Monte Carlo events and the MC-Truth information: The MC-Truth 3-momentum has been compared with the reconstructed momentum after the 5C-fit.
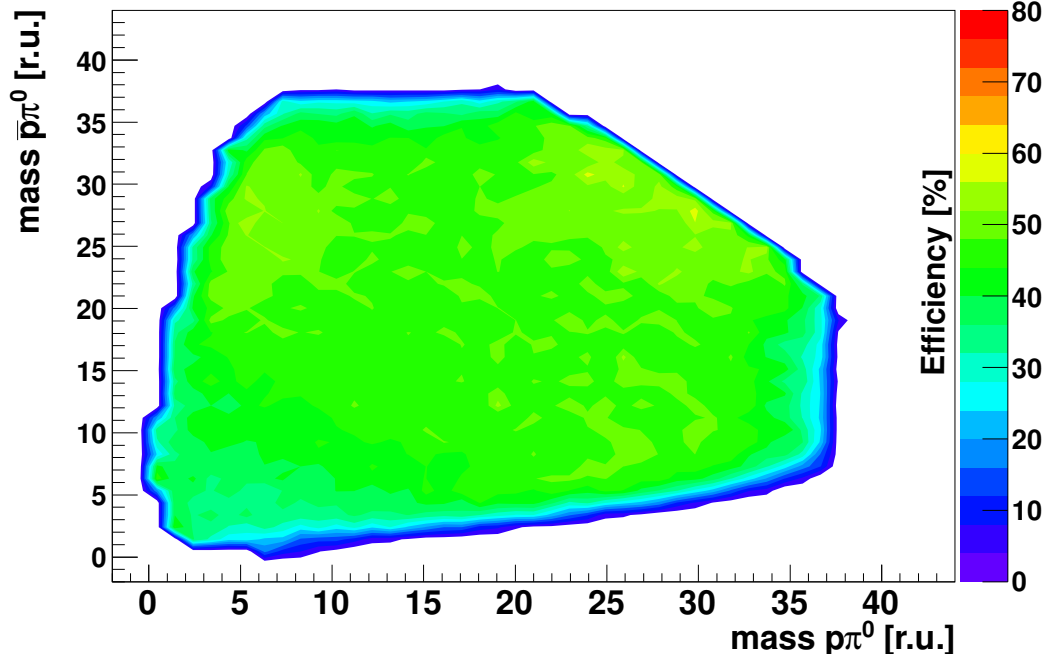
Figure (6.6) The efficiency map used for the correction of the data at an energy of 3.773 GeV.

The absolute values have been subtracted, filled into a histogram and fitted with a Gaussian function. Figure 6.5 shows the mean values and the standard deviations σ, determined by the fit, as a function of the χ^2 of the 5C-fit.

For a $\chi^2 < 50$ the momentum spread (σ) will be smaller than ~ 5 MeV. Hence, for a bin size for the efficiency correction of 30 MeV, 99.7% of the reconstructed data will be in the same bin as the MC-Truth data (assuming that the events will be located at the center of the bin). If the events would be directly at the border of a bin, 50% of all events would be in the adjacent bin. However, the reconstruction efficiency and number of events is only varying smoothly from bin to bin. This effect can be neglected.

Different bin sizes for the Dalitz plot between ~ 15 MeV and ~ 55 MeV have been used in this analysis and the systematic effects are estimated in section 6.7.

Figure 6.6 shows the generated efficiency map. The reconstruction efficiencies are not varying too much, except at the borders where they are rather low.

This can be explained as following: At the left and at the lower border the opening angle between proton or antiproton and the π^0 is rather low and a photon will be emitted in the direction of the proton or antiproton. Thus, the events will be suppressed by the initial event selection criteria. For the upper right border the proton antiproton opening angle is small and the momentum of the π^0 is rather high.

The small opening angle and the low momentum of the charged tracks are the reason for the small reconstruction efficiency. At the other borders in between, a mixture of both effects is observed.

6.4. Data After Final Event Selection and Efficiency Correction

The upper right plot in figure 6.7(a) shows the Dalitz plot of the 2916 pb^{-1} data taken at the energy of $\sqrt{s}$ =3.773 GeV, the lower left plot in figure 6.7(a) is the Dalitz plot after the efficiency correction. The red histograms in the upper left and lower right figures are the efficiency corrected ones, whereas the black ones are not corrected for efficiency.

The events are not phase space distributed and a lot of structure can be seen. At the mass of around 1.5 GeV/c^2 and 1.65 GeV/c^2 two structures can be guessed, which can be the nucleon resonances N(1535) and N(1650). In the region for masses higher than 2 GeV/c^2, also a lot "activity" is observed.

The origin of the structures can be revealed by a partial wave analysis, which considers isospin 1/2 and 3/2 resonances. However, the large parameter set required, will lead to results with large uncertainties.

Figure 6.8 shows the reconstructed cross sections for the decays to $p\bar{p}\pi^0$ as a function of $\sqrt{s}$. The cross section are calculated according to

$$\sigma_{e^+e^- \to p\bar{p}\pi^0} = \frac{N_{sig.}}{\epsilon \cdot \mathcal{L}} \quad , \tag{6.4.1}$$

with $N_{sig.}$ the number of signals passing the final event selection, ϵ the reconstruction efficiency and $\mathcal{L}$ the integrated luminosity.
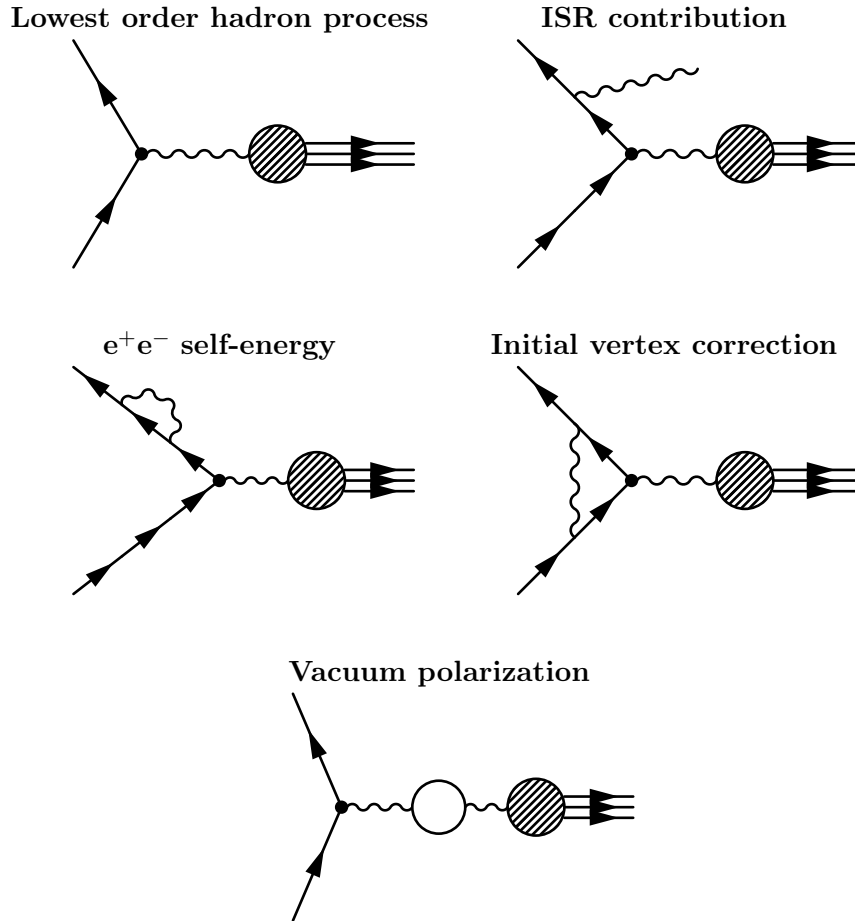
6.5. Radiative Corrections

The cross section measured in e^+e^- experiments is a superposition of the lowest order cross section — the *Born cross section* — and higher order cross sections. The Feynman diagrams of the respective higher order cross sections interfering with the lowest order cross section are shown in table 6.9. They all describe QED processes, which are fully calculable. Divergences arising in the calculation of the individual terms cancel each other. The observed cross section dependents on experimental conditions, as the detection efficiencies for the ISR photons do enter. Thus, the relevant cross section allowing for the comparison of the results of different experiments is the Born cross section, which needs to be extracted from the measured cross section.

(a)

(b)
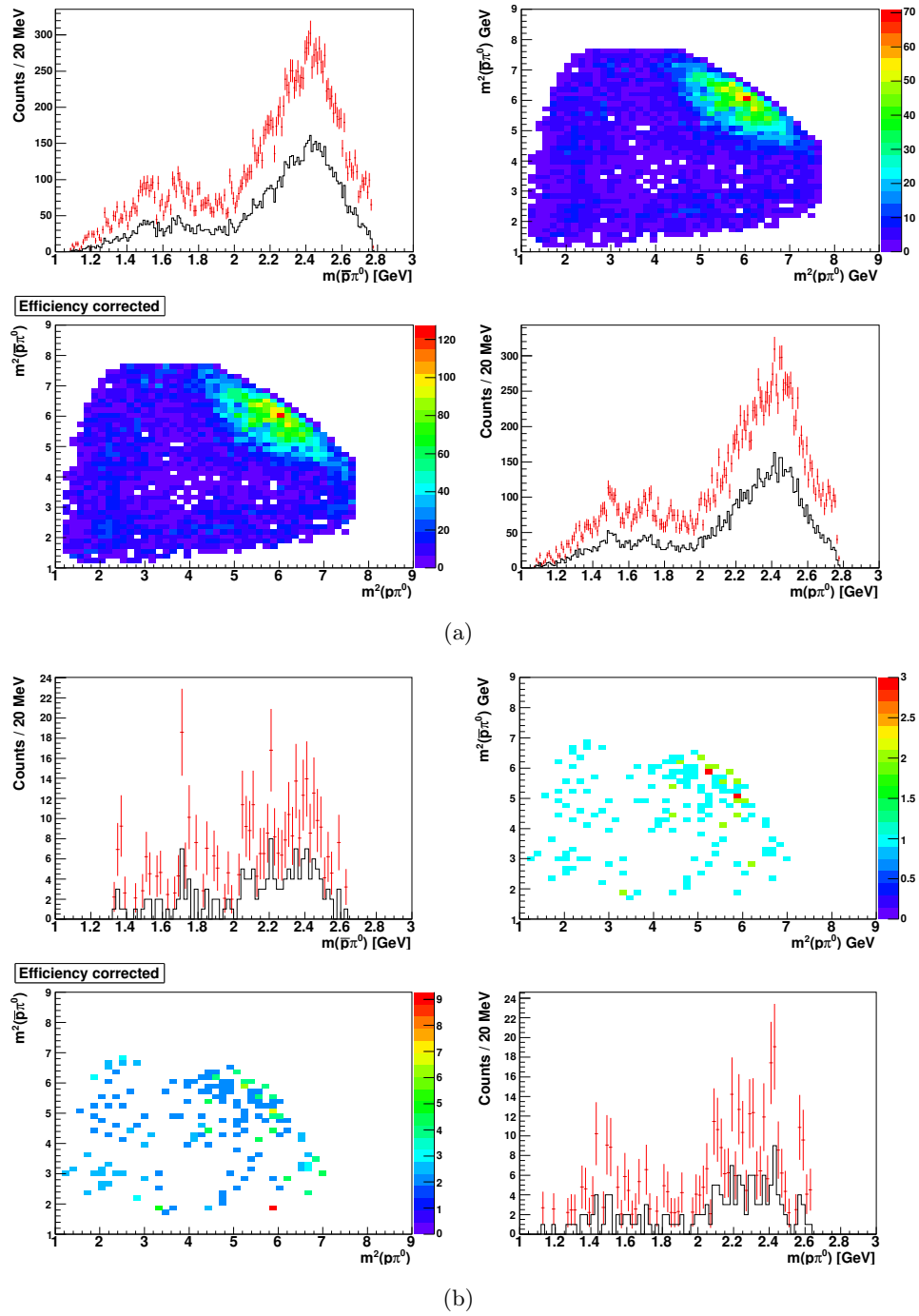
Figure (6.7)   **(a)** is for the data taken at 3.773 GeV, **(b)** for the data taken at 3.65 GeV. The respective upper left and lower right figure show the invariant mass spectra of m($p\pi^0$) and m($\bar{p}\pi^0$). The red curves are the mass spectra after efficiency correction. The respective upper right plot is the Dalitz plot without efficiency correction, for the lower left plot the efficiency correction has been applied.
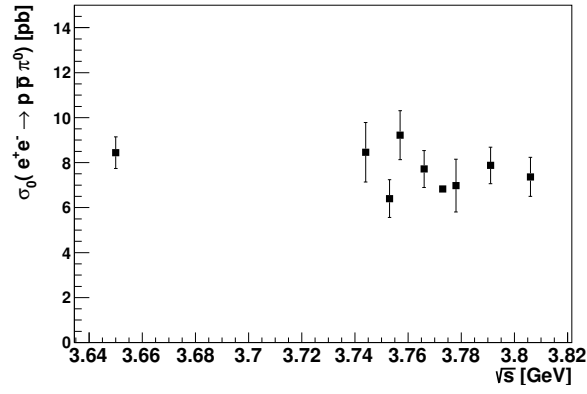
Figure (6.8) The efficiency corrected cross section σ for the decays to $p\bar{p}\pi^0$ as a function of $\sqrt{s}$. The errors are the statistical ones.

Figure (6.9) Feynman diagrams for the process $e^+e^- \to$ hadrons. All contributions from diagrams, except of the *lowest order hadron process*, are represented by the radiative correction factor δ. The self-energy and the ISR contribution exist for both fermion lines.

Considering only the ISR process, the process effectively studied is $e^+e^- \to f + n\gamma$, with $n = 0, 1, 2, \ldots$ and f a final state. Its cross section can be written as

$$\sigma(s) = \int_0^{1-m_{th}^2/s} W(s, x)\sigma_0(s(1-x))dx. \tag{6.5.1}$$

$W(s, x)$ is the radiator function describing the probability density for photons carrying away a fraction x of the beam energy. $\sigma_0(s(1-x))$ is the Born cross section of the finale state f.

Since the fraction of energy carried away by ISR photons can be limited by requiring momentum and energy balance, it is sufficient to relate the measured cross section to the Born cross section by the radiative correction factor $(1+\delta)$. Thus, equation 6.4.1 can be rewritten as

$$\sigma_{e^+e^- \to p\bar{p}\pi^0} = \frac{N_{sig.}}{\epsilon \, \mathcal{L} \, (1 + \delta)} \quad, \tag{6.5.2}$$

where $\sigma_{e^+e^- \to p\bar{p}\pi^0}$ is now the Born cross section [105, 106].
The radiative correction factor itself can be rewritten as

$$1 + \delta = 1 + \delta_{\text{ver.}} + \delta_{\text{vac.}}^{l\bar{l}} + \delta_{\text{vac.}}^{\text{had.}} + \delta_\gamma \quad, \tag{6.5.3}$$

with $\delta_{\text{ver.}}$ the vertex correction, $\delta_{\text{vac.}}^{l\bar{l}}$ and $\delta_{\text{vac.}}^{\text{had.}}$ the leptonic and hadronic vacuum contribution, which can be calculated independently from the detector's geometry by the formulas given in [105, 106].
The last term, δ_γ, is related to the ISR photons and thus is experiment dependent (the detection efficiency for the radiated photons enters). It can be expressed accordingly to [105, 106] as

$$\delta_\gamma = \beta \int_0^{k_m} \frac{dk}{k} k^\beta \left[(1 - k + \frac{k^2}{2})\frac{\epsilon(k)\sigma_0(s')}{\epsilon(0)\sigma_0(s)} - 1\right] + k_m^\beta - 1 \quad, \tag{6.5.4}$$

with $\beta = 2\alpha/\pi \cdot (log(s/m_e^2) - 1)$, the *equivalent radiator* describing the probability of a photon emission from the electron or positron. m_e is the electron mass, α the fine-structure constant, s the *Mandelstam* variable s and $s' = s(1 - k)$. $\epsilon(k)$ is the detection efficiency of events with a radiated photon of relative energy k.
However, δ_γ is depending also on the Born cross section σ_0, which was planned to be determined with this radiative correction procedure. To solve this dilemma an iterative way of the calculation is chosen:

1. First the observed cross section is taken as input (described by formula 6.8.1) for the calculation of $1 + \delta$. The result of this step is marked as $1 + \delta^{(1)}$.

2. The $1 + \delta^{(1)}$ is then used to correct the observed cross section, which is marked as $\sigma^{(1)}_{cor.}$.

3. The corrected cross section $\sigma^{(1)}_{cor.}$ is then used as input for the calculation of a refined radiative correction factor, which will be marked as $1 + \delta^{(2)}$.

4. The steps are repeated until the result converges (already true after a few iterations).

The detection efficiencies $\epsilon(k)$ required for the determination of the radiative correction factor, can be obtained from Monte-Carlo simulations. Details on the simulation are provided in section 6.7. The detection efficiencies as a function of k are shown in figure B.9.

6.6. Background Estimation

Different background sources have to be considered in this analysis. Background may arise from $D\overline{D}$ decays, which is the dominant decay channel of the $\psi(3770)$ resonance [10]. Furthermore, background events from similar final states, such as $\psi(3770) \to p\overline{p}\pi^0\gamma$ has to be considered.

Another important background source is arising from initial state radiation to the lower lying $J^{PC} = 1^{--}$ resonances (radiative return). These resonances are not considered in the line shape used for the determination of the radiative correction factor δ_γ.

6.6.1. Background from Initial State Radiation at $\sqrt{s} =$ 3.773 GeV

Initial state radiation can lead to an energy drop and a J/ψ or a ψ(2S) might be produced at a collision energy of 3.773 GeV. Hence, the selected candidates can contain background events from an radiative return. Since only the line shape without the resonances is considered in the radiative correction procedure, these background events (N^b) have to be subtracted from the number of efficiency corrected events ($N_{cor.}$).

Their contribution is estimated with Monte Carlo samples (γ_{ISR}J/ψ and $\gamma_{ISR}\psi$(2S) at 3.773 GeV), typical about 30% larger then the collected data.

Naively one would expect zero events for the γ_{ISR}J/ψ sample, as the detection efficiency for the events with such a high energetic ISR photon is zero (compare to
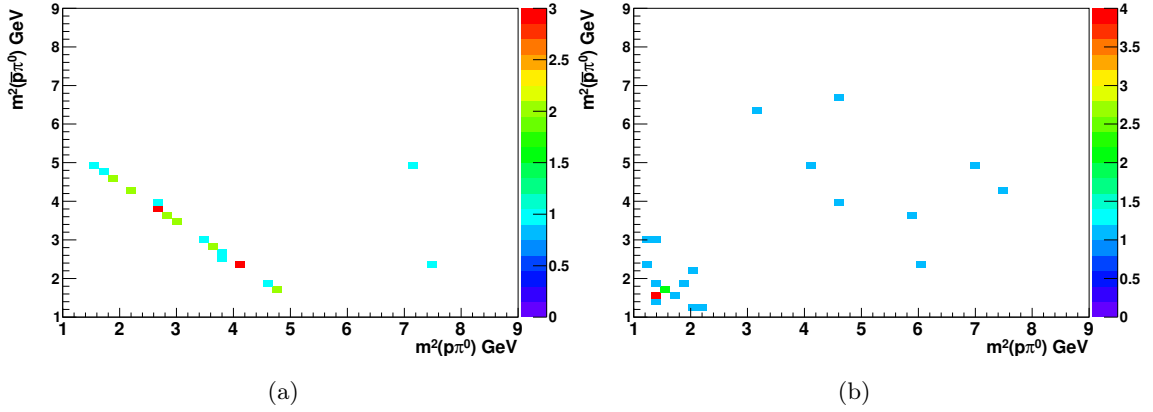
Figure (6.10)   **(a)** shows the background events from $\gamma_{ISR}J/\psi$. The proton and antiproton are from the J/ψ decay and a fake π^0 is reconstructed from the ISR photon and a photon from the antiproton annihilation. **(b)** shows the background events from $\gamma_{ISR}\psi(2S)$. The events have various sources, but about 60% are from the process $\gamma_{ISR}\psi(2S) \to \gamma_{ISR}p\bar{p}\pi^0$.

figure B.9). However, a few events are found in this sample: For most of these events a fake photon from the antiproton annihilation was combined with the ISR photon to a π^0, the proton and antiproton produced in a J/ψ decay to $p\bar{p}$. The remaining events are from J/ψ decays to $p\bar{p}\gamma$; again the ISR photon was used to reconstruct a fake π^0.

Table 6.2 shows the number of events considered for the correction. The events from the $\gamma_{ISR}\psi(2S)$ sample, where about 60% of the events are coming from the process $\gamma_{ISR}\psi(2S) \to \gamma_{ISR}p\bar{p}\pi^0$, are given as well. Figure 6.10(a) and 6.10(b) show the Dalitz plots for these background events.

6.6.2. Background from $D\overline{D}$ Decays at $\sqrt{s} =$3.773 GeV

The $\psi(3770)$ decays dominantly into $D\overline{D}$ pairs and some of the decays might be misidentified as $p\bar{p}\pi^0$ final state. To estimate this background component a Monte Carlo sample containing inclusive $D\overline{D}$ decays (4.8 times larger than the data taken at 3.773 GeV) has been analyzed. The fraction of events passing the event selection is only 0.01% of all reconstructed $p\bar{p}\pi^0$ events and thus is neglected (compare to table 6.2).

6.6.3. Background from Similar Decay Channels at $\sqrt{s} =$3.773 GeV

Final states, similar to the analyzed decay channel, may pass the event selection. For example, the cut $N_\gamma \geq 2$ in the initial event selection (compare to section 6.2.1), allows a variety of other final states (compare to table 6.3).

Source	$N_b^{cor.}$	in % of $N_{cor.}$
$(\gamma_{ISR})J/\psi$	46.98	0.24
$(\gamma_{ISR})\psi(2S)$	52.72	0.26
$D\overline{D}$	3.05	0.015

Table (6.2) Number of background events N_b at $\sqrt{s} = 3.773$ GeV for the different sources. They have been subtracted from the number of corrected events $N_{cor.}$.

The total cross section at an energy of 3.773 GeV is $\sigma_{e^+e^-}^{3.773} \approx 20.72$ nb, the *observed* cross section of $\psi(3770)$ contributes about 7.71 nb [107, 108]. The known resonant branching fraction are used for the estimation of the background events given in table 6.3. Unknown branching ratios are estimated by the one of $\psi(2S)$ decays. As the $\psi(2S)$ can not decay into $D\overline{D}$ pairs and the $\psi(3770)$ has a small non $D\overline{D}$ branching fraction and no further threshold opens, which could enhance the branching ratio of the respective decay mode, this assumption is reasonable.

The sum of all these events after efficiency correction is estimated to be 75.7, which is about 0.40% of all events. However, the estimation of the branching ratios implies that the background events can not be simply subtracted from the number of signals and thus have to be considered in the systematic error.

To validate the assumptions for the background estimations an additional approach has been performed: The π^0 sidebands ($6\sigma < |m(\gamma\gamma) - m(\pi^0)| < 9\sigma$) events have been studied to estimate the background. The contribution is here found to be 0.29% of all corrected events and thus in agreement with the prior estimated value.

6.6.4. Background from Similar Decay Channels at the Scan Data Points

The dominating sources of the background arising from similar decay channels at $\sqrt{s} = 3.773$ GeV have been analyzed for the scan data points, too. The results are given in table 6.4.

The same cross section and branching ratios as in section 6.6.3 have been used. The estimated number of background events is not subtracted from the number of signals events, but considered in the systematic error (compare to section 6.6.3).

6.6.5. Background at $\sqrt{s} = 3.65$ GeV

The events taken at $\sqrt{s} = 3.65$ GeV can contain contributions from the $\psi(2S)$ resonance. Its cross section is estimated to be $\sigma_{\psi(2S)}^{3.65} = (0.136 \pm 0.012)$ nb at this energy [20].

The total number of these events can be calculated to

Decay channel $\psi(3770)$		Branching ratio		Survived events (BR cor.)
$\gamma\chi_{c0}$	$\chi_{c0} \to p\overline{p}$	$1.66 \cdot 10^{-6}$		0.66
$\gamma\chi_{c0}$	$\chi_{c0} \to p\overline{p}\pi^0$	$4.16 \cdot 10^{-6}$		0.15
$\gamma\chi_{c1}$	$\chi_{c1} \to p\overline{p}$	$2.12 \cdot 10^{-7}$		0.09
$\gamma\chi_{c1}$	$\chi_{c1} \to p\overline{p}\pi^0$	$3.48 \cdot 10^{-7}$		0.01
$\gamma\chi_{c2}$	$\chi_{c2} \to p\overline{p}$	$6.48 \cdot 10^{-8}$		0.03
$\gamma\chi_{c2}$	$\chi_{c2} \to p\overline{p}\pi^0$	$4.23 \cdot 10^{-7}$		0.02
$\gamma\eta_c$	$\eta_c \to p\overline{p}$	$4.42 \cdot 10^{-6}$	(*)	1.19
$\gamma\eta_c(2S)$	$\eta_c(2S) \to p\overline{p}$	$9.1 \cdot 10^{-7}$	(**)	0.15
$p\overline{p}$		$2.7 \cdot 10^{-4}$	(*)	1.67
$p\overline{p}\gamma$		$3.9 \cdot 10^{-5}$	(*)	12.84
$p\overline{p}\pi^0\gamma$		$1.3 \cdot 10^{-4}$	(***)	16.90
$p\overline{p}\pi^0\gamma\gamma$		—		0

Table (6.3) The estimated contaminations from similar decay channels to the one analyzed. The branching ratio are from [10]. (*) As an upper limit the branching ratio of the $\psi(2S)$ decay has been used. (**) As an upper limit the branching ratio of $\psi(2S)$ and the η_c decay has been used. (***) As an upper limit the branching ratio of $\psi(2S) \to p\overline{p}\pi^0$ has been used.

Energy	Survived Events (BR. corrected)		
[GeV]	$\psi(3770) \to p\overline{p}$	$\psi(3770) \to p\overline{p}\gamma$	$\psi(3770) \to p\overline{p}\pi^0\gamma$
3.744	0.0013	0.016	0.023
3.753	0.0025	0.025	0.042
3.757	0	0.029	0.045
3.766	0.0061	0.038	0.059
3.778	0.004	0.027	0.029
3.791	0.0033	0.034	0.054
3.806	0.006	0.034	0.054

Table (6.4) The estimated contaminations from similar decay channels for the scan data points. The same cross sections and the same branching ratios as in section 6.6.3 have been used for the estimation of the amount of background events.

Decay channel		$\psi(2S)$ tail (BR cor.)	Survived Events (BR. cor.)
$\gamma\chi_{c0}$	$\chi_{c0} \to p\overline{p}$	0.0024	0.12
$\gamma\chi_{c0}$	$\chi_{c0} \to p\overline{p}\pi^0$	0.00002	0.023
$\gamma\chi_{c1}$	$\chi_{c1} \to p\overline{p}$	0.0003	0.016
$\gamma\chi_{c1}$	$\chi_{c1} \to p\overline{p}\pi^0$	0.00006	0.019
$\gamma\chi_{c2}$	$\chi_{c2} \to p\overline{p}$	0.0003	0.006
$\gamma\chi_{c2}$	$\chi_{c2} \to p\overline{p}\pi^0$	0	0
$\gamma\eta_c$	$\eta_c \to p\overline{p}$	0.0001	0.019
$\gamma\eta_c(2S)$	$\eta_c(2S) \to p\overline{p}$	≈ 0	≈ 0
$p\overline{p}$		0	0
$p\overline{p}\gamma$		0.0009	0.167
$p\overline{p}\pi^0\gamma$		0.002	0.247
$p\overline{p}\pi^0\gamma\gamma$		0	0

Table (6.5) Background at 3.65 GeV — the branching ratios are taken from [10].

$$N = \sigma^{3.65}_{\psi(2S)} \cdot \mathcal{L} \cdot \text{BR}(\psi(2S) \to p\overline{p}\pi^0) = 0.796 \pm 0.172 \quad , \qquad (6.6.1)$$

with $\mathcal{L}$ the integrated luminosity and $\text{BR}(\psi(2S) \to p\overline{p}\pi^0)$ the branching ratio of the $\psi(2S)$ decay [10]. This number has been subtracted from the number of events at $\sqrt{s} =$3.65 GeV.

Similar decay channels due to the $\psi(2S)$ contribution can be neglected at this energy. The background channels are summarized in table 6.5 — the tail contribution of the $\psi(2S)$ is determined using equation 6.6.1, but multiplied with a factor to take into account the misidentification. The total cross section at this energy point has been taken from [109], the branching ratios from [10].

6.6.6. Study of the $\gamma_{ISR}\psi(2S)$ Background at $\sqrt{s} =$3.744 GeV

The data at 3.744 GeV should have the highest fraction of $\gamma_{ISR}\psi(2S)$ events, as it is closest to the $\psi(2S)$ resonance. A non-significant contribution at an 3.744 GeV implies a non-significant contribution at higher energies, too.

Using an exclusive MC event sample $(e^+e^- (@ \, 3.744 \, GeV) \to \gamma_{ISR}\psi(2S) \to \gamma_{ISR}p\overline{p}\pi^0)$, the detection efficiency is determined to be 2.51 % (compare to figure 6.11(a)). Figure 6.11(b) shows the real data at an energy of 3.744 GeV. The black curve shows all events directly after the particle identification applying only the $cos(\theta)$ cut. The π^0 is reconstructed with those photons, whose combination is closest to the π^0 mass.

(a)　　　　　　　　　　　　　(b)
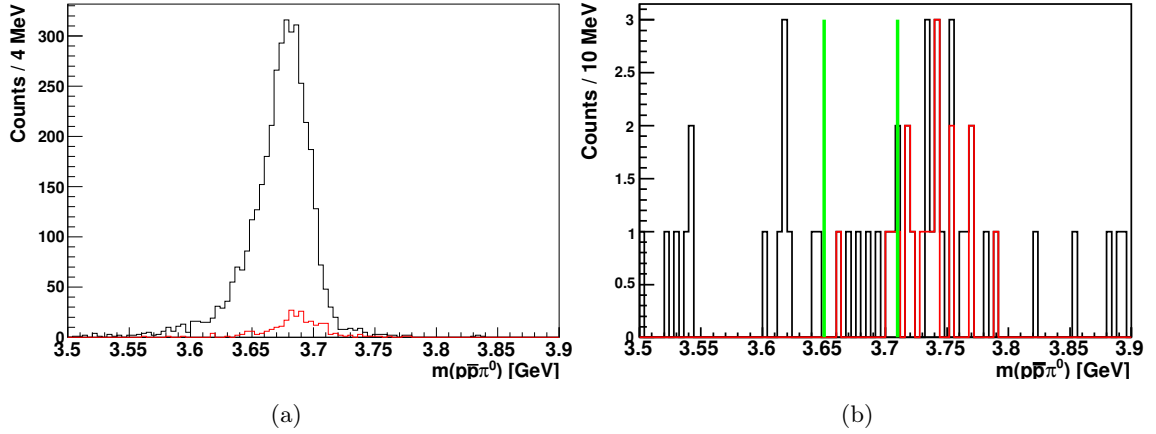
Figure (6.11) **(a)** $\gamma_{ISR}\psi(2S)$ Monte Carlo at 3.744 GeV: The black curve are all events that pass the 5C-fit ($\chi^2_{5C} < 200$), the red curve are the events which pass the final event selection. **(b)** Data at 3.744 GeV: The black curve shows the events after particle identification (for details compare to text), the red curve are the events, which pass the final event selection.

The red curve shows the data which pass the final event selection. The green lines indicate the $\psi(2S)$ region.

In order to observe one $\psi(2S)$ background event in the final event data (red curve), the green interval would have to contain ≈ 40 counts.

As only a few events are observed, one can conclude that the contribution of $\gamma_{ISR}\psi(2S)$ events can be neglected at this energy and at higher energies as well. This result is also consistent with the values estimated in section 6.6.1.

6.7. Systematic Errors

The systematic errors are summarized in table 6.6. Except for the first three errors, which are uncorrelated, the errors exhibit a strong correlation (among the different energy points). This correlation has to be considered for the extraction of the cross section and is discussed in section 6.7.11.

Source	Error [%]			Correl-
	3.773 GeV	3.65 GeV	Scan	ation
Efficiency determination	1.5	1.5	1.5	–
Background exclusive channel	0.4	0.4	0.4	–
Size of official MC	0.5			–
Radiative correction procedure	4.0	4.0	4.0	✓
Extraction of Born cross section	1.5	1.5	1.5	✓
Kinematic fit	2	2	2	✓
MDC tracking	1 (p) +1 ($\overline{\text{p}}$)	1 (p) +1 ($\overline{\text{p}}$)	1 (p) +1 ($\overline{\text{p}}$)	✓
Photon selection	2	2	2	✓
PID	1 (p) +2 ($\overline{\text{p}}$)	1 (p) +2 ($\overline{\text{p}}$)	1 (p) +2 ($\overline{\text{p}}$)	✓
Integrated luminosity	1.1	1.1	1.1	✓
Polarization	0.7	0.7	0.7	✓
Energy measurement	1.0 MeV	1.0 MeV	1.0 MeV	✓

Table (6.6) An overview over the relative systematic errors.

6.7.1. Uncertainties for the Efficiency Determination

The efficiency has been determined by dividing the Dalitz plot into different bins and calculating the ratio of RECONSTRUCTED DATA/MC-TRUTH DATA (compare to section 6.3). The reconstruction efficiency within one bin is assumed to be constant. To estimated an error for this assumption, different grid-sizes of the Dalitz plot have been tried and the efficiency has been calculated again. The differences are not larger than 1.5%; this value is eventually used as systematic uncertainty for the efficiency determination.

6.7.2. Uncertainties for the Background Estimation

6.7.2.1. Exclusive Channels

The uncertainties arising from similar decay channels passing the event selection have been estimated in section 6.6.3 and 6.6.4 and the results are given in table 6.3 and 6.4. For the dominating channels passing the event selection criteria the number of background events at the $\psi(3770)$ resonance have been estimated (as they are not measured yet) using the branching ratios from the $\psi(2S)$ decays given in [10].
Considering the largest errors given in [10] and the results from the π^0 sideband estimation (compare to section 6.6.3), the amount of these background events will not exceed 0.4% of all events. This value has been used as systematic uncertainty

for the exclusive channels.

6.7.2.2. Monte Carlo Event Sets

The background events arising from ISR returns and D$\overline{\text{D}}$ decays have been estimated in section 6.6 using inclusive Monte Carlo event samples. The size of the samples is estimated to be about 1.3 and 4.8 times larger than the data, respectively. Even if the size has been estimated wrong by 10%, the amount of background events would not be rise or shrink by more than 0.5%. The systematic uncertainty is chosen to be 0.5%.

6.7.3. Uncertainties for the Radiative Correction Procedure

For the determination of the radiative correction factor, the detection efficiency of events with a radiated photon of relative energy k, $\epsilon(k)$ is required (compare to section 6.5). The efficiencies have been determined using Monte Carlo events. The simulated process is $e^+e^- \to m_x\gamma$, the underlying model the *VECTORISR* model. The mass of the state m_x defines the energy of the photon and decays to $p\overline{p}\pi^0$. The state m_x is boosted according to the simulated photon.

However, the angular distribution of the radiated photon might be different from the true case. Since no appropriate generator with the correct ISR distribution for the analyzed decay channel is existing yet, additional MC samples have been produced containing the process $e^+e^- \to m_x$. The detection efficiency for these samples has been estimated again and the radiative correction factors have been recalculated. The difference between both radiative correction factors is smaller than 3.0% and thus 3.0% is used as systematic error.

Additionally, the uncertainty of the whole scheme has to be considered. Therefore, the results of the scheme applied in section 6.5 have been compared with the results from a different method, the structure function method [110, 111]. The radiator function (equation 6.5.1) required for the calculation, is taken from [112]. The difference between both methods is 2%, which is similar to the uncertainty given in [106]. The combined error is 3.61%. As a conservative estimate, 4.0% is taken as total uncertainty of the radiative correction procedure.

6.7.4. Uncertainties for the Extraction of the Born Cross Section

Different χ^2 cuts of the 5C-fit should lead to similar results. However, this is not true: Opening the χ^2 cut, more events will pass the event selection, which have a worse momentum balance of initial state and final state.

(a) (b)
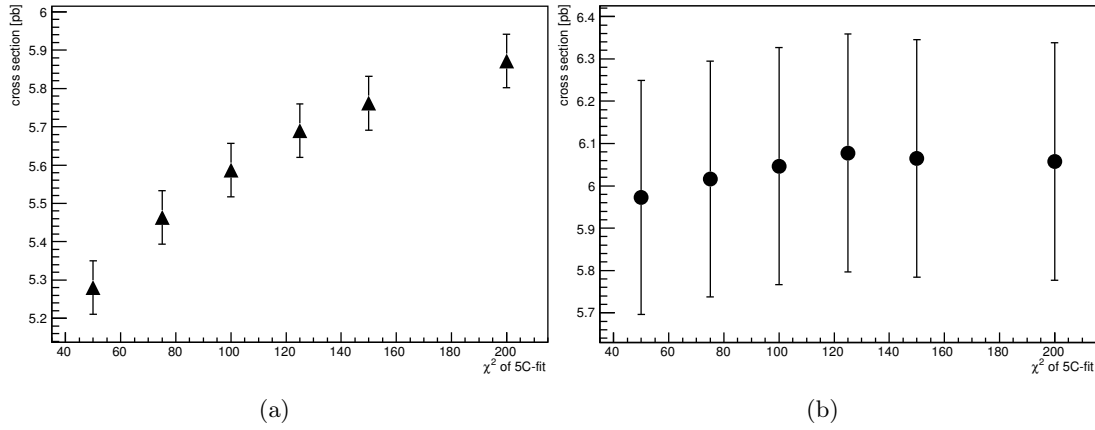
Figure (6.12) **(a)** The extracted cross sections at $\sqrt{s}$=3.773 GeV as a function of the χ^2-cut of the 5C-fit. The cross section has not been corrected by the radiative correction procedure. The given errors are the statistical ones.
(b) The same cross sections, but after applying the radiative correction. The error bars include the error of the radiative correction procedure and the statistical errors.

As a consequence more ISR events will show up, which are not covered by the standard efficiency correction. In figure 6.12(a) it can be clearly seen, that the cross section is experiment dependent, one could also say cut-dependent.

After applying the ISR correction procedure described in section 6.5, the cross sections have almost similar values, they do not differ by more than 1.5% (compare to figure 6.12(b)). This value is used as systematic error.

6.7.5. Uncertainties of the Kinematic Fit

The kinematic fit's systematic error is estimated using a control sample of $\psi(2S)\rightarrow p\bar{p}\pi^0$ decays. Therefor, an inclusive $\psi(2S)$ Monte Carlo event sample and the data collected at the $\psi(2S)$ resonance are compared with each other.

Applying the final event selection criteria presented in section 6.2.3 (except the χ^2-cut) and additionally a cut on the charged tracks ($|\cos(\theta)|$<0.8), on the total momentum of the final state and the invariant mass of the final state ($|m(p\bar{p}\pi^0)$-3.686 GeV|<40 MeV), a sub sample is obtained, which contains almost only decays of $\psi(2S)\rightarrow p\bar{p}\pi^0$. The purity of the sub sample is estimated to be 99% by using the MC-Truth information from the inclusive $\psi(2S)$ Monte Carlo events. The selected events and the cuts are shown in figure 6.14(b) for data and in figure 6.14(a) for the inclusive $\psi(2S)$ Monte Carlo events.
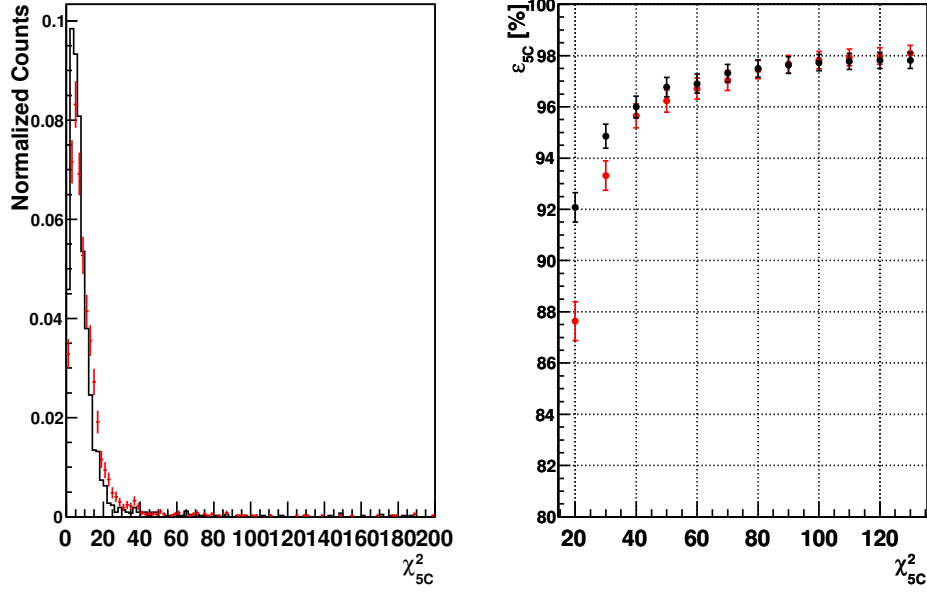
Figure (6.13) The left plot shows the comparison of the χ^2 of the kinematic 5C-fit between inclusive $\psi(2S)$ Monte Carlo events (black) and the data collected at the $\psi(2S)$ resonance (red). The right figure shows the difference in efficiencies of kinematic 5C-fit depending on the χ^2 cut between the inclusive $\psi(2S)$ Monte Carlo events (black) and the data collected at the $\psi(2S)$ resonance (red).

An efficiency of the kinematic fit can be defined as

$$\epsilon_{5C} = \frac{N_{5C}}{N_{sub}} \quad ,$$

with N_{5C} the events passing the kinematic fit and N_{sub} the total number of events of the selected sub sample. This efficiency can be used as measure for the difference between the Monte Carlo events and the $\psi(2S)$ data.

The right plot in figure 6.13 shows the difference in the χ^2 distributions, whereas the left plot in figure 6.13 shows the comparison of the efficiencies of the fits. The difference after applying the cut $\chi^2_{5C} < 50$ is (0.54 ± 0.55) %.

Considering the correct photon selection ratio of $(99.25 \pm 0.09)\%$ (compare to section 6.2.2) the largest error of the fit should not exceed 2%, which is taken as systematic error.

6.7.6. Uncertainties for the MDC Tracking

The uncertainties for the MDC tracking efficiency have been studied in [113]. For a transverse momentum p_t larger than 300 MeV the difference between Monte Carlo events and data for the proton and anti-proton has to be found to be less than 1%. Thus, 1% is taken as systematic error.

(a) (b)
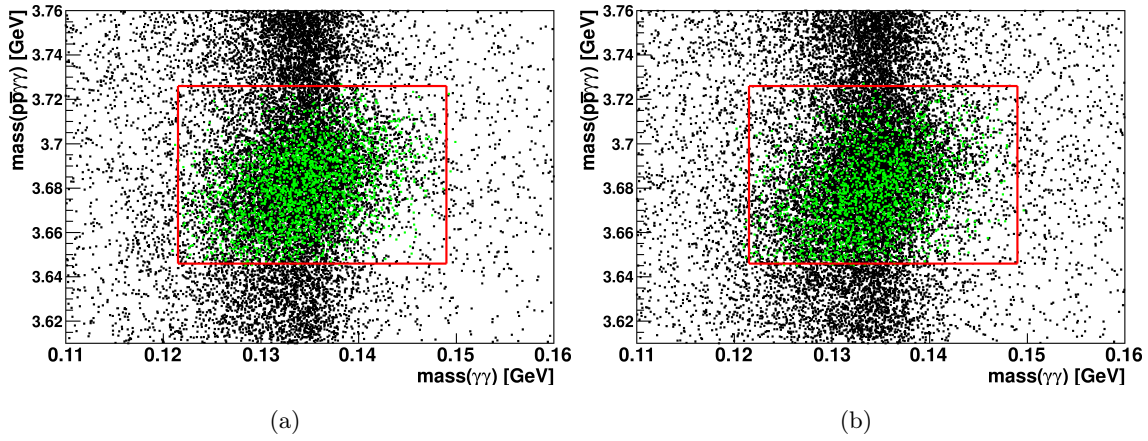
Figure (6.14)   **(a)** shows the selected $p\bar{p}\pi^0$ events for inclusive $\psi(2S)$ Monte Carlo events. The black points are the data after a preselection, the red lines indicate the mass cuts applied and the green data points are the finally selected events. The purity of the selected subsample is 99%.

(b) shows the events for data taken at the $\psi(2S)$ resonance. The black points are the data after a preselection, the red lines indicate the mass cuts applied and the green data points are the selected events.

6.7.7. Uncertainties for the Photon Selection

The uncertainties for the photon selection have been studied in [114] and are determined to be 1%. The systematic uncertainty for the selection of 2 photons arising from π^0 and η decay is calculated to be 2%.

6.7.8. Uncertainties for the Particle Identification

The uncertainties arising due to the particle identification have been studied in [113]. For a transverse momentum p_t larger than 300 MeV the difference between Monte Carlo events and data is smaller than 1% for a proton and less than 2% for the antiproton.

6.7.9. Uncertainties of the Polarization

The $\cos\theta$ distribution of the π^0 is extracted from data and fitted with the function $\beta(1 + \alpha\cos^2\theta)$ (compare to section 6.3). The fit result is: $\beta = 0.89 \pm 0.02$ and $\alpha = 0.55 \pm 0.08$.

In order to determine the systematic uncertainty, the mean value of the fit was shifted according to its upper and lower limit and the cross section at an energy of 3.773 GeV

has been recalculated. The differences are 0.7% and 0.6%, respectively. The largest difference (0.7%) is taken as the systematic error.

6.7.10. Uncertainties for the Integrated Luminosity

The integrated luminosities have been determined in [115]:

E_{cms} [GeV]	Luminosity [pb^{-1}]
3.650	$44.49 \pm 0.02 \pm 0.44$
3.773	$2916.94 \pm 0.18 \pm 29.17$

Table (6.7) Calculated luminosities from [115].

The systematic uncertainty is taken as 1.1%. For the scan data points the luminosity has been determined using large angle Bhabha events (compare to table 6.8). The systematic error for the scan data points is determined to be 1.1%.

E_{cms} [GeV]	Luminosity [nb^{-1}]
3.744	4939.1 ± 13.3
3.753	9313.3 ± 16.8
3.757	8043.5 ± 12.9
3.766	11864.1 ± 21.4
3.778	5695.3 ± 13.1
3.791	12474.8 ± 22.5
3.806	10149.4 ± 22.3

Table (6.8) Calculated luminosity and the statistical error for the scan data points.

6.7.11. Treatment of Correlated Errors

Most of the systematic errors are correlated (compare to table 6.6). They cannot be easily summed up and considered directly in the fit. To estimate the effect of correlated errors, the *offset method* [116] has been used. Here, only a short summary over the working principle is given (compare also to [117]):

1. Perform fit without correlated systematics.

2. Shift measurement to the upper limit of its systematic.

3. Redo fit and record differences to fit without correlated systematics.

4. Go back to (2) and shift measurement to lower limit.

5. Repeat step 2-4 for all sources of correlated systematics.

6. Add all deviations in quadrature (Treat positive and negative results separately).

6.8. Extraction of the Cross Section of $\psi(3770) \to p\overline{p}\pi^0$

Resonant cross sections can be generally described by the Breit-Wigner formula [10]. Taking into account the continuum cross section and a phase between continuum and resonant production amplitude, the cross section as a function of the Mandelstam variable s can be written as

$$\sigma(s) = \left| \sqrt{\sigma_{con}} + \sqrt{\sigma_\psi} \frac{m\Gamma}{s - m^2 + im\Gamma} \exp\left(i\phi\right) \right|^2 . \tag{6.8.1}$$

σ_ψ is the resonant cross section, m the mass and Γ the width of the respective resonance, the parameter ϕ is the phase between the resonant and continuum amplitude. The continuum cross section σ_{con} can be described as a function of $\sqrt{s}$ by

$$\sigma_{con} \propto \frac{1}{s^\lambda} \quad , \tag{6.8.2}$$

where the exponent λ is a priori unknown.

The fit of the formula to the data points and the extraction of the respective quantities seems to be straightforward. However, it has to be taken into account, that not the whole continuum amplitude is allowed to interfere with the resonant one:

The virtual photon arising in an electron positron annihilation can be associated with an isospin of $I = 0$ or $I = 1$. In order to produce a $J^{PC} = 1^{--}$ charmonium resonance only the $I = 0$ component contributes, since charmonium states do not contain u or d quarks and hence have $I = 0$. However, for the continuum production, the photon is not restricted to $I = 0$, but rather can have $I = 1$ or $I = 0$. This is also the reason, why Δ resonances ($I = 3/2$) can be observed in the continuum process in association with a proton or antiproton, but not in resonant charmonium decays. According to quantum mechanics only states with the same quantum numbers can mix or interfere with each other. Following this thought equation 6.8.1 has to be modified, since only a certain part of the resonant process can interfere with the continuum process:

$$\sigma(s) = \left| \sqrt{M\sigma_{con}} + \sqrt{\sigma_\psi} \frac{m\Gamma}{s - m^2 + im\Gamma} \exp(i\phi) \right|^2 + (1 - M)\sigma_{con} \quad , \tag{6.8.3}$$

with M describing the fraction of the continuum amplitude allowed to interfere with the resonant amplitude. Since the resonant amplitude $\sqrt{\sigma_\psi}$ is correlated to M, the

parameter M cannot be simply determined by a fit and theoretical input is required. Thus, the question of the isospin share of the virtual photon is arising, which is discussed, for example, in [118–123]. The basic idea in [118, 119] is the dominance of single states in the virtual intermediate state, which can be for example excited ρ^* or ω^* mesons or coherent pion configurations with $I = 0$ and $I = 1$. Their amplitudes can be written as

$$A(e^+e^- \to \rho \text{ (Isopin=1)}) = \frac{1}{\sqrt{2}}(A_u - A_d) = \frac{C}{\sqrt{2}}$$
$$A(e^+e^- \to \omega \text{ (Isopin=0)}) = \frac{1}{\sqrt{2}}(A_u + A_d) = \frac{1}{3}\frac{C}{\sqrt{2}} \quad,$$

assuming that the whole coupling depends only on the charge of the quarks. Hence, the ratio should be

$$\frac{I=0}{I=1} = \frac{\left(\frac{1}{3}\frac{C}{\sqrt{2}}\right)^2}{\left(\frac{C}{\sqrt{2}}\right)^2} = 1 \; : \; 9 \tag{6.8.4}$$

and the continuum cross section can be written as

$$\sigma_{con} = \frac{1}{10}\sigma_{con}^{|I=0\rangle} + \frac{9}{10}\sigma_{con}^{|I=1\rangle} \quad. \tag{6.8.5}$$

Clearest evidence for such a ratio comes from the process $e^+e^- \to N\pi$ around 2 GeV, where the ratio of $I = 0$ and $I = 1$ is 1:9 [118, 119]. Also the electromagnetic decay width of the $\rho(770)$ and the $\omega(782)$ meson are in agreement with the ratio: $\Gamma(\omega(782) \to e^+e^-)/\Gamma(\rho(782) \to e^+e^-) \sim 1 : 9$. That the ratio continues to stay large at higher energies is consistent with ideas of generalized vector meson dominance models [118].

6.9. Results

The data has been corrected with the radiative correction factors determined in section 6.5. The background estimated in section 6.6 has been subtracted. Eventually, the cross section has been fitted with equation 6.8.3 allowing 1/10 of the continuum amplitude to interfere with the resonant one. The mass m and the width Γ in equation 6.8.3 have been fixed accordingly to the world average values for the $\psi(3770)$ resonance [10]. The maximum likelihood fit yields for the Born cross section $\sigma(\psi(3770) \to p\bar{p}\pi^0)$ a value of $0.87^{+1.27}_{-0.72}$ pb and for the corresponding phase

$271.4^{+29.2}_{-27.2}$ °. A phase equal 270° corresponds to a total destructive interference between continuum and resonant production amplitude.

As the error on the cross section is too large, an upper limit at 90% confidence level (CL) has been determined. Therefor it is assumed, that the total error can be described by a Gaussian distribution.

The fit results are summarized in table 6.9, the correlated systematic uncertainties are included. The corrected data points and the fit are shown in figure 6.15(a), the fit's χ^2/n.d.f is 1.3, where n.d.f. is the number of degrees of freedom.

$\sigma_{\psi(3770)}$ [pb]	Phase angle [°]
$0.87^{+1.27+0.05}_{-0.72-0.05}$ (< 2.7 @ 90 % CL)	$271.4\ ^{+29.2+4.2}_{-27.2-4.2}$

Table (6.9) The parameters extracted from the fit under the assumption that only 1/10 of the continuum production amplitude can interfere with the resonant amplitude. The first errors are the one arising from the fit; the second ones are correlated systematic uncertainties. The fit's χ^2/n.d.f is 1.3.

6.9.1. Results Allowing Interference with the Whole Continuum Amplitude

As an instructive example, the cross section allowing the whole continuum amplitude to interfere with the resonant one (i.e. setting M=1 in equation 6.8.3) is determined, too. Two different solutions with the same $\chi^2/n.d.f. = 5.8/5$ are found, which according to [124] both have to be considered. The solutions are given in table 6.10, the fit itself is shown in figure 6.15(b). The phase for both solutions is again in agreement with a destructive interference, a dip at an energy of 3.773 GeV can be clearly seen in figure 6.15(b).

Parameter	Solution 1	Solution 2
$\sigma_{\psi(3770)}$ [pb]	$0.061^{+0.05+0.004}_{-0.04-0.004}$ (< 0.13 @ 90% CL)	$33.7\ ^{+1.2+0.8}_{-1.2-0.9}$
Phase angle [°]	$270.7\ ^{+39.0+4.7}_{-36.1-4.7}$	$269.8\ ^{+1.7+0.2}_{-1.7-0.2}$

Table (6.10) The parameter extracted from the fit under the assumption that the whole continuum production amplitude can interfere with the resonant amplitude. The fit's χ^2/n.d.f. is 1.2.

(a)

(b)
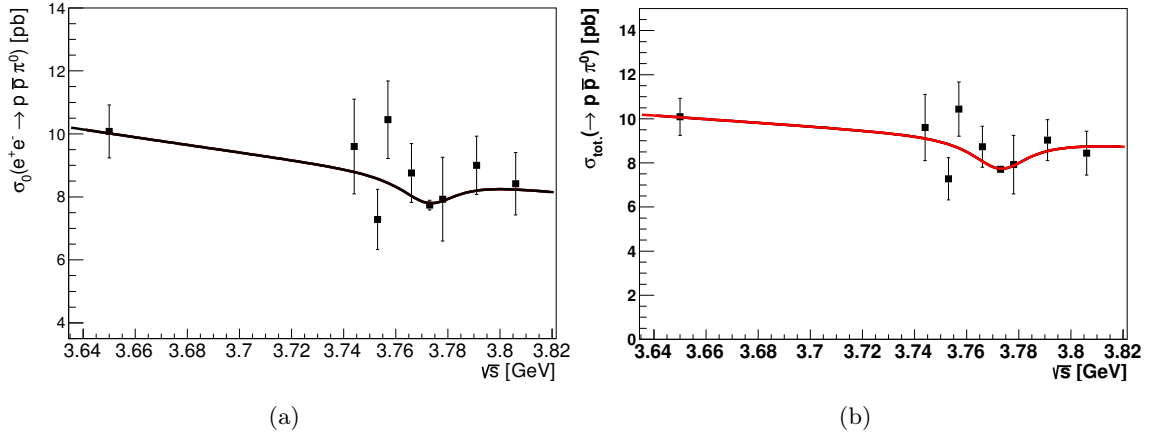
Figure (6.15) **(a)** shows the solution of the fit under the assumption that only $1/10$ of the continuum amplitude can interfere with the resonant amplitude; the fit's $\chi^2/\text{n.d.f}$ is 1.3. **(b)** shows the solution of the fit under the assumption that the whole the continuum amplitude can interfere with the resonant amplitude; the fit's $\chi^2/\text{n.d.f}$ is 1.2.

6.10. Estimation of the Cross Section of $p\bar{p} \to \psi(3770)\pi^0$

The cross sections of the charmonium production processes $p\bar{p} \to \psi m$, where ψ is a charmonium state and m a light meson can be related to the partial decay width of $\psi \to p\bar{p}m$ [8]. Therefor a constant decay amplitude $\mathcal{M}$ is assumed, which allows to relate the decay width of $\psi \to p\bar{p}m$ directly to the area A_D of the Dalitz plot [8, 10]:

$$\Gamma_{\psi \to p\bar{p}m} = \frac{1}{2S_\psi + 1} \frac{1}{8\pi^3} \frac{32}{M_\psi^3} \left[\sum |\mathcal{M}|^2 \right] A_D \quad , \tag{6.10.1}$$

where M_ψ is the mass and S_ψ the spin of the charmonium state. Under the assumption of a constant decay amplitude the production cross section $\sigma_{p\bar{p} \to \psi m}$ can be written as

$$\sigma_{p\bar{p} \to \psi m} = \frac{1}{64\pi} \frac{p_m^{cms}}{p_p^{cms}} s^{-1} \left[\sum |\mathcal{M}|^2 \right] \quad , \tag{6.10.2}$$

with p_x^{cms} the corresponding particle's momentum in the center of mass system and s the Mandelstam variable [8].

Eliminating the squared amplitude, which both equation 6.10.1 and 6.10.2 have in common, the production cross section can be expressed as:

$$\sigma_{p\bar{p} \to \psi m} = 4\pi^2 (2S_\psi + 1) \frac{M_\psi^3}{A_D} \Gamma_{\psi \to mp\bar{p}} \left[\frac{p_m^{cms}}{p_p^{cms}} s^{-1} \right] \quad . \tag{6.10.3}$$

(a) (b)
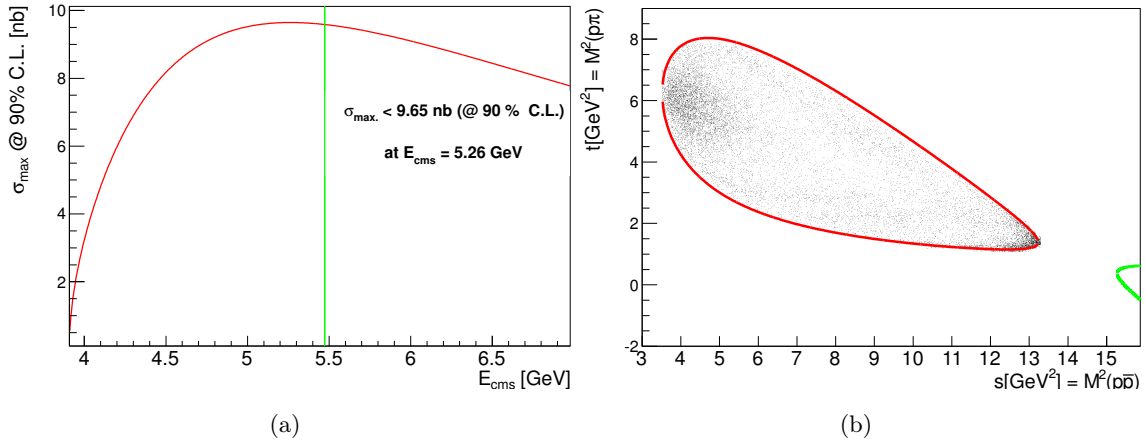
Figure (6.16) **(a)** The cross section for the process of $p\bar{p} \to \psi(3770)\pi^0$, which has been calculated according to equation 6.10.3 and under the assumption that $1/10$ continuum production amplitude can interfere with the resonant production amplitude. The green vertical line shows the maximum c.m.s energy available at $\overline{P}ANDA$.
(b) The s- and t-channel for the investigated process: The red framed region shows the Dalitz plot evaluated in the analysis of the data collected by the BESIII experiment, the green framed region is the kinematic region for the process $p\bar{p} \to \psi(3770)\pi^0$ accessible at $\overline{P}ANDA$ (assuming a maximum momentum of the antiproton of 15 GeV/c [1]).

The proton's and the meson's momentum can be calculated for the kinematic situation at the $\overline{P}ANDA$ experiment using relativistic kinematics. $\overline{P}ANDA$ will be a fix target experiment: The proton is at rest and the antiproton has a certain momentum in the laboratory frame.
The partial decay width of $\psi(3770) \to p\bar{p}\pi^0$ can be calculated with the help of the Born cross section for the $\psi(3770)$ and the estimated cross section determined in section 6.9. The Born cross section is given as [10]:

$$\sigma_{Born}^{\psi(3770)} = \frac{12\pi\Gamma_{ee}\Gamma_{tot}}{(E_{cm}^2 - M^2) + M^2\Gamma_{tot}^2} = (10.01 \pm 0.78) \text{ nb} \qquad , \qquad (6.10.4)$$

Γ_{ee} is the partial electron decay width, Γ_{tot} is the total decay width, M the mass of the resonance and E_{cm} the center of mass energy. All values have been taken from [10], E_{cm} was set equal to M.
The cross section of $\sigma(p\bar{p} \to \psi(3770)\pi^0)$ has been calculated according to formula 6.10.3, the result for the solution allowing $1/10$ of the continuum amplitude to interfere with the resonant one is shown in figure 6.16(a): The green vertical line indicates the maximum c.m.s energy available at $\overline{P}ANDA$. The maximum cross section for $p\bar{p} \to \psi(3770)\pi^0$ can be expected at a center of mass energy of 5.26 GeV and will be

less than 9.7 nb @ 90% CL.

Figure 6.16(b) shows the s- and t-channel for the analyzed process: The red framed region shows the Dalitz plot for $e^+e^- \to p\bar{p}\pi^0$ events, the green framed region is the kinematic region for the process $p\bar{p} \to \psi(3770)\pi^0$ accessible at $\overline{\text{P}}$ANDA .

The cross sections for the solutions allowing the whole continuum amplitude to interfere with the resonant one are calculated, too: The larger branching ratio (solution 2) results in a production cross section of 120^{+8}_{-8} nb, whereas the first solution results in an upper limit at a 90% CL of < 0.46 nb for the production cross section $\sigma(p\bar{p} \to \psi(3770)\pi^0)$.

Chapter 7

Summary, Discussion and Outlook

The first part of this thesis is focusing on the development of simulation and reconstruction software packages for a possible ToF detector upgrade of the BESIII experiment. In the second part, the cross section of $\psi(3770) \to p\bar{p}\pi^0$ has been determined and the cross section of $p\bar{p} \to \psi(3770)\pi^0$, which is from great importance for the $\overline{\text{P}}$ANDA experiment, has been estimated.

For both parts an independent summary will be given:

MRPC Detector Upgrade

The simulation software includes the implementation of the MRPC's geometry and is based on a model, which is motivated by realistic physical processes. It allows for the simulation of the characteristics of the MRPC detector and is able to reproduce and explain the beam test results.

The simulated reconstruction efficiency matches well with the beam test results over the whole investigated range of electrical field values (85 kV/cm up to 120 kV/cm). The simulated time resolution does coincide with the measured data starting from electric field values of $\sim$100 kV/cm. For smaller values the time resolution is underestimated by the simulation as the model does not include recombination effects of electron-ion pairs. However, the simulation results do show the same trend for the time resolution as the measured data: They rise for smaller electrical field strengths. However, the upgrade is planned to be operated at an electrical field strength of $\sim$112 kV/cm, where simulated data and measured results do agree.

The reconstruction software allows for a matching of tracks from the MDC with the ToF information and applies several corrections (e.g. walk and signal transition time corrections), which help to improve the time of flight resolution. The measured time over threshold is used for the determination of the energy loss in the MRPC's material of electrons/positron and photons and thus for a correction of the EMC energy measurement.

The results of the simulation of the ToF system, based on available MRPC technology, show that the design goal of an improved pion/kaon particle identification at a 2σ level up to momenta of 1.4 GeV/c can be achieved for the BESIII detector. The total resolution for the difference of measured time of flight and expected time of flight is $\sim$80 ps for pions and kaons with momenta around 1.45 GeV/c.

The reconstruction efficiencies are similar to those of the current ToF detector system. However, in total more tracks are usable, as the high momentum pion and kaon tracks can be clearly identified and so be used for analysis.

Estimation of $\sigma(\psi(3770) \to p\bar{p}\pi^0)$ and $\sigma(p\bar{p} \to \psi(3770)\pi^0)$

Using the 2916 pb^{-1} data accumulated at a center of mass energy of 3.773 GeV and the data collected during a $\psi(3770)$ line shape scan by the BESIII detector, an analysis of the process of $e^+e^- \to p\bar{p}\pi^0$ has been performed. The Born cross section of $\psi(3770) \to p\bar{p}\pi^0$ has been determined allowing 1/10 of the continuum amplitude — the fraction with the same isospin component — to interfere with the resonant amplitude.

As an instructive exercise the solution allowing the whole continuum amplitude to interfere with the resonant one is determined. Here two solutions with the same probability are found.

A summary of the results is given in table 7.1, the upper limits at a 90% CL are obtained under the assumption that the total error can be described by a Gaussian distribution.

The branching fraction for the decay of $\psi(3770) \to p\bar{p}\pi^0$ can be obtained with the estimated cross section and the Born cross section from the $\psi(3770)$ resonance, which can be calculated assuming a relativistic Breit-Wigner description of the resonance and the world average values from [10] to 10.01 ± 0.78 nb. The resulting branching ratio for $\psi(3770) \to p\bar{p}\pi^0$ is $< 2.7 \cdot 10^{-4}$ @ 90% CL.

This value is in agreement with the upper limit of less than $1.2 \cdot 10^{-3}$ reported by the BESII collaboration [10]. However, the result of the BESII collaboration is estimated under the assumption that interference effects can be neglected and thus a comparison of both values is actually not legit.

The solution allowing the whole continuum amplitude to interfere with the resonant one results in branching ratios of about 0.3% and an upper limit of less than $8.6 \cdot 10^{-5}$ @ 90% CL. According to [10] a branching ratio of 0.3% would be one of the largest branching ratios ever reported for the $\psi(3770)$. However, also the small solution would be possible and would fit much better

Interference Scenario	10%	100%	
		Solution 1	Solution 2
$\sigma(\psi(3770) \to p\bar{p}\pi^0)$ [pb]	$\mathbf{0.87^{+1.27+0.05}_{-0.72-0.05}}$ $\mathbf{< 2.7\ @\ 90\%\ CL}$	$0.061^{+0.05+0.004}_{-0.05-0.004}$ $< 0.13\ @\ 90\%\ CL$	$33.7^{+1.2+0.8}_{-1.2-0.9}$
Phase angle [°]	$\mathbf{271.4^{+29.2+4.2}_{-27.3-4.2}}$	$270.7^{+39.0+4.7}_{-36.1-4.7}$	$269.8^{+1.7+0.2}_{-1.7-0.2}$
$\sigma_{max}(p\bar{p} \to \psi(3770)\pi^0)$ [nb]	$\mathbf{< 9.7\ @\ 90\%\ CL}$	$< 0.5\ @\ 90\%\ CL$	120^{+8}_{-8}

Table (7.1) A summary of the analysis results. The ratio for the interference scenario describe, which fraction of the continuum production amplitude can interfere with the resonant production amplitude, the scenario allowing 100% of the continuum amplitude to interfere with the resonant is only presented as an instructive example. The phase given is the one for the solution of the fit. The maximum proton antiproton cross section is determined for the kinematic situation at the $\overline{\text{P}}$ANDA experiment and can be expected at a center of mass energy of 5.26 GeV.

in the common picture of $\psi(3770)$ decays: Most of the so far reported non-$D\overline{D}$ branching fractions of the $\psi(3770)$ are upper limits smaller than 10^{-3} [10].

The phase determined for the solution of the fit is in agreement with a total destructive interference between the continuum and resonant production amplitude — total destructive interference corresponds to a phase of 270°. Since the resonant production amplitude can be again divided into two different amplitudes — the 3-gluon amplitude a_{3g} and the electromagnetic amplitude a_γ — the total cross section is

$$\sigma \propto |a_{3g} + a_\gamma + a_c|^2 \quad ,$$

where a_c is the continuum amplitude. The ratio of the amplitude a_γ and the 3-gluon amplitude a_{3g} for the $\psi(3770)$ resonance can be calculated accordingly to [24, 25]:

$$\left| \frac{a_\gamma(m^2_{\psi''})}{a_c(m^2_{\psi''})} \right| = \frac{3}{\alpha} \mathcal{B}(\psi'' \to e^+e^-) \approx 3.99 \cdot 10^{-3} \quad ,$$

where $\mathcal{B}(\psi'' \to e^+e^-)$ was taken from [10]. As the electromagnetic resonant amplitude is small compared to the continuum amplitude, the interference can be interpreted as the interference between the 3-gluon and the continuum amplitude and thus as a destructive interference between strong and electromagnetic production amplitude [24, 25].

Recent, but model dependent results — the investigation of the phase using the non-resonant electromagnetic continuum does not rely on any model — did

show phases between strong and electromagnetic amplitude of $\sim 90°$ for the J/ψ and the $\psi(2S)$ resonance, but also phases of $270°$ $(\hat{=} -90°)$ could not be excluded for the $\psi(2S)$ [125, 126].

Using the constant decay amplitude approximation and the model presented in section 6.10 [8] and the estimated partial decay width, the cross section of $\sigma(p\overline{p} \rightarrow \psi(3770)\pi^0)$ has been estimated for the kinematic situation at the $\overline{P}$ANDA experiment: $\overline{p} + p \rightarrow \psi(3770) + \pi^0$, where the antiproton has a certain momentum and the proton is at rest.

The maximum cross section for $\sigma(p\overline{p} \rightarrow \psi(3770)\pi^0)$ has been calculated to be < 9.7 nb @ 90% CL. The cross section starts to rise from the production threshold of the π^0 and a $\psi(3770)$ meson and reaches its maximum at a center of mass energy of 5.26 GeV (compare to figure 6.16(a)) and eventually starts to decrease again. The value of 5.26 GeV corresponds to an antiproton momentum of $\sim$13.8 GeV/c in the laboratory frame and thus is still in reach of $\overline{P}$ANDA [1]. Table 7.1 gives an overview over the estimated results; also the corresponding values for the solution allowing the whole continuum amplitude to interfere with the resonant one are given.

Benchmark studies for the process $p\overline{p} \rightarrow D\overline{D}$ assessing the ability to separate charm signals from the large hadronic background for the $\overline{P}$ANDA experiment assume a cross section of $\sigma(p\overline{p} \rightarrow \psi(3770) \rightarrow D^+D^-)$=2.8 nb [1]. Using a value of 60 mb for the total $p\overline{p}$ cross section and considering only the $D^\pm$ decays into $K\pi\pi$ the expected signal to background ratio at $\overline{P}$ANDA is estimated to be $4 \cdot 10^{-10}$ [1].

Assuming the same values and a photon detection efficiency of 90%, the ratio for the process of $p\overline{p} \rightarrow \psi(3770)\pi^0 \rightarrow D^+D^-\pi^0$ would be $\lesssim 4.7 \cdot 10^{-10}$ for the upper limit allowing 1/10 of the continuum amplitude to interfere with the resonant one and thus almost similar. Hence, the production of a $\psi(3770)$ in association with a π^0 is also suited to study the open charm region.

However, the relation of the decay width to the production cross sections is based on a simple constant amplitude approximation, which does not consider energy dependence and resonance effects in the experimental Dalitz plots of $\psi(3770) \rightarrow p\overline{p}\pi^0$. Thus, the calculated cross sections should be seen as a simple estimate. The large estimation can be an artifact of baryon resonance contribution (for example the aforementioned N* resonances). They do not necessarily need to contribute to the production cross section [8].

However, the estimates for the cross section of $\sigma(p\overline{p} \rightarrow \psi(3770) \rightarrow D^+D^-)$

are based on an extrapolation of the $J/\psi \to p\bar{p}$ branching ratio to the $\psi(3770)$ resonance [1]. Thus, they might not be appropriate and can be even smaller. The study of the channel in association with pions might become even more promising. More results, which might clarify this situation, can be expected in near future by the BESIII and by the LHCb collaboration.

More data of $\psi(3770)$ decays might also be helpful to clarify the situation of the destructive interference between resonant and continuum amplitude. Such data can be accumulated by the BESIII experiment and might also help to solve the dilemma of the large difference in expected and measured non-$D\overline{D}$ branching ratios of the $\psi(3770)$ resonance, which has been discussed in the introduction. However, to obtain correct results interference effects between the different amplitudes should be taken into account. Most of the results listed in [10] do not consider interference effects so far.

In summary, the planned upgrade of the endcap time of flight detector of the BESIII experiment will not only improve the quality and analysis possibilities of further $\psi(3770)$ data, but of all the data to be accumulated at the BESIII experiment. Thus, the analysis of the expected data from the BESIII experiment in general will lead to a better understanding of the $\tau - charm$ energy region and be of great importance for the $\overline{P}$ANDA experiment. The gathered knowledge will allow for the formulation of detection strategies for the $\overline{P}$ANDA experiment and thus for an unprecedented investigation of the fundamental physical questions of the strong interaction in the non-perturbative region.

Appendix A

Appendix — MRPC

A.1. Design Drafts of the MRPC Module

Material	height	low. width	up. width	thickness	note
strips	25			0.035	24, 4mm gaps in between
inner glass	344	88.68	147.32	0.4	10 pieces
outer glass	350	98.17	157.83	0.55	4 pieces
graphite elect.	346	93.51	152.49	0.13	4 pieces
mylar	352	103	163	0.07	4 pieces
PCB	352	114	174	0.9/1.5	2+1 pieces
honeycomb	350	98.17	157.83	3	2 pieces
tape	350	98.17	157.83	0.13	2, for the honeycomb
gas gaps				0.22	12 gaps

Table (A.1)   All sizes are in [mm]. The building blocks are trapeze-shaped.
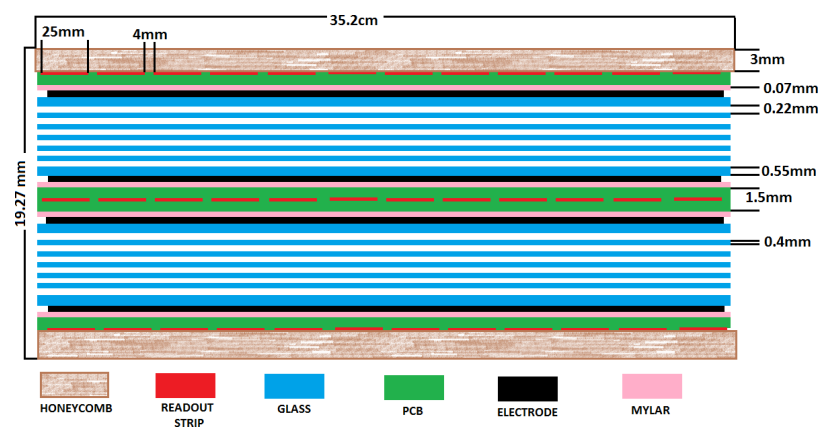
Figure (A.1)   Sketch of the MRPC planned to be used for the ToF upgrade at the BESIII experiment. PCB is the shortcut for printed circuit board.
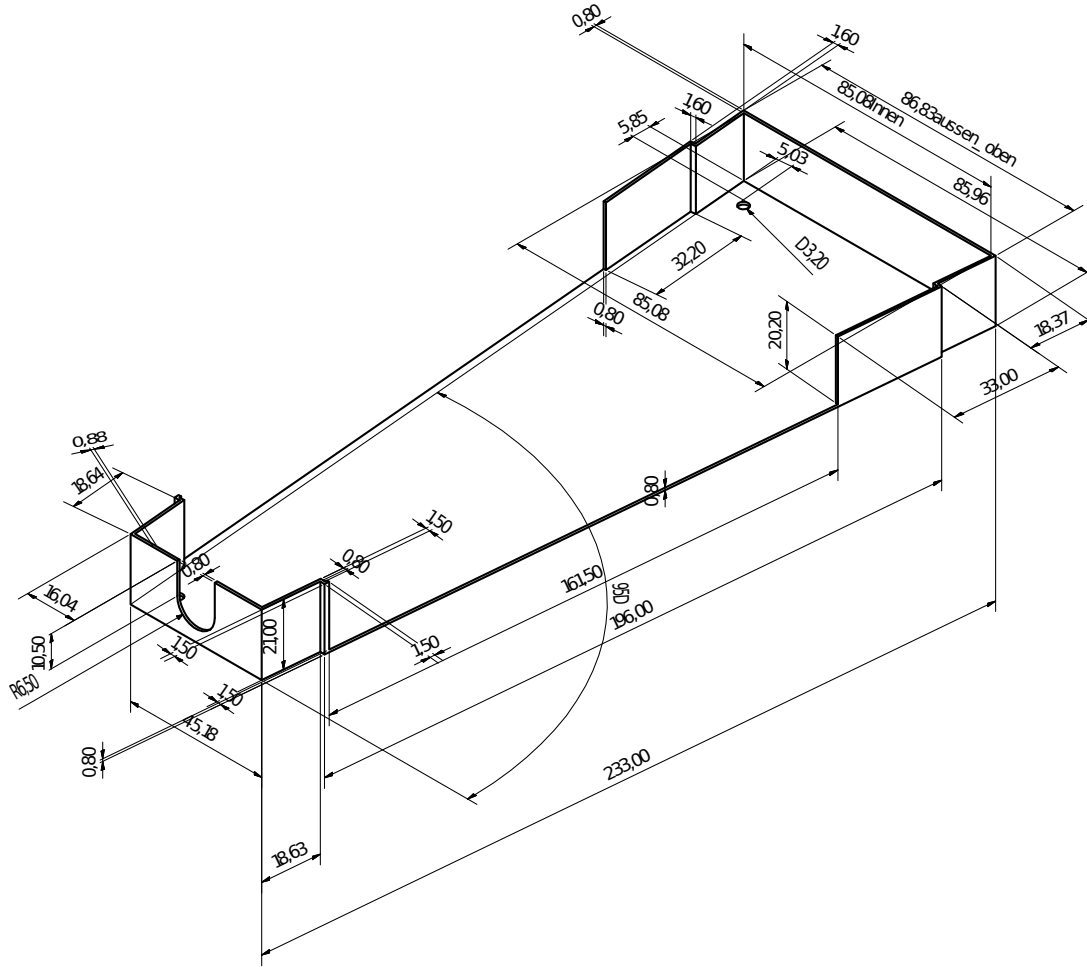
Figure (A.2) Design drawing for the box, which will contain the front-end electronics. It is build of aluminum. All dimension are in [mm].

Figure (A.3) Drawing of the frame, which will contain one MRPC module. The frame's material will be aluminum. It will be covered by two 1 mm thick plates, in order to seal it air-tight.
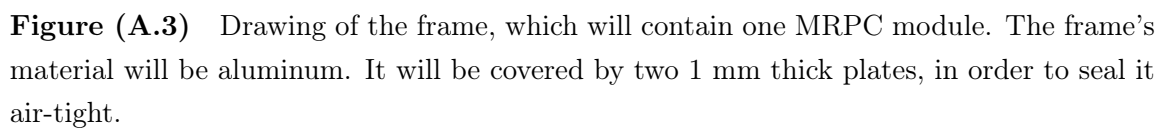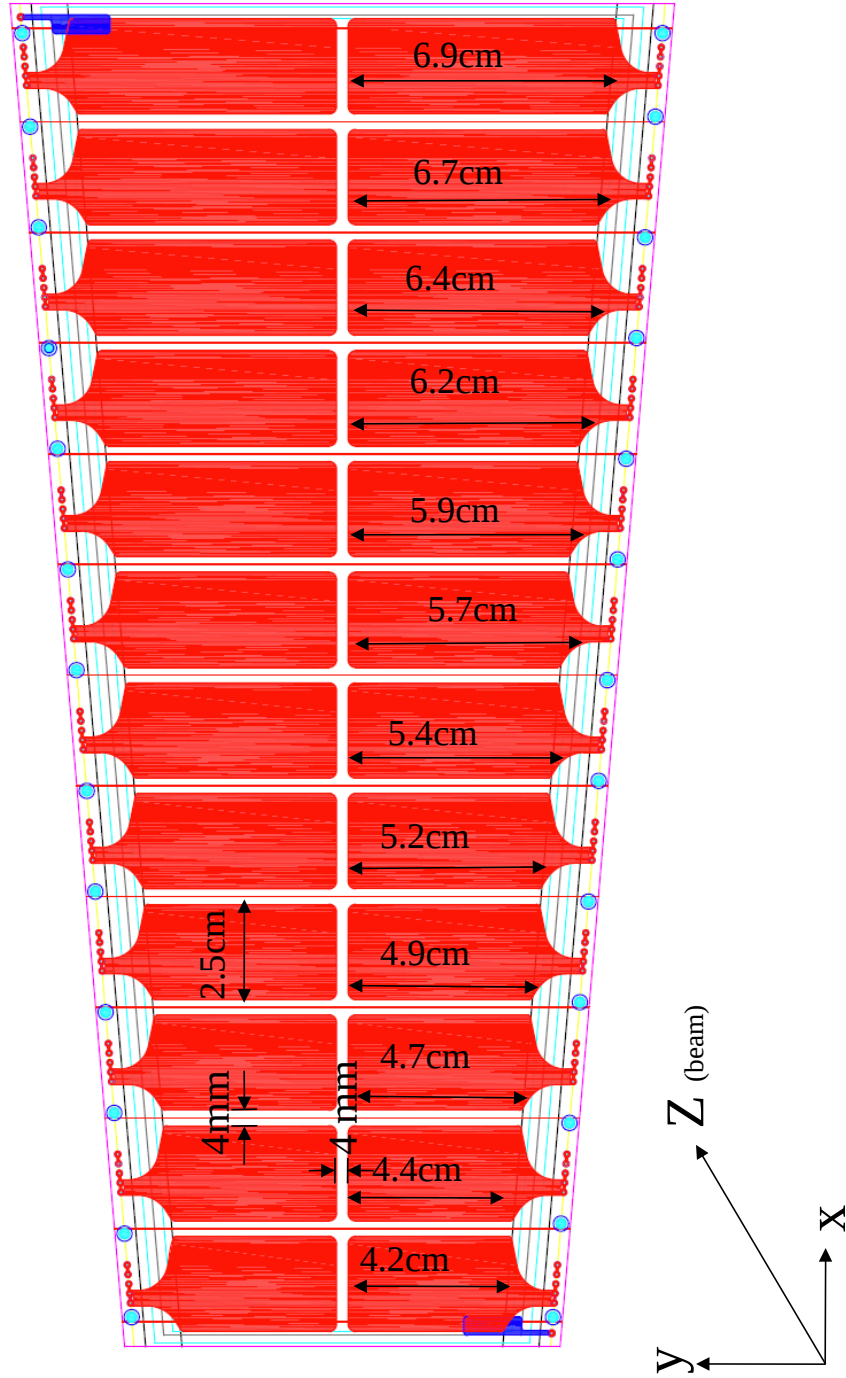
Figure (A.4) Sketch of the readout-pads and their dimension for the single end readout version. The strip length of the double sided readout version is $2 \cdot x + 4$ mm, where x is the corresponding length of the strip of the single end read version.

A.2. Neighborhood Sets
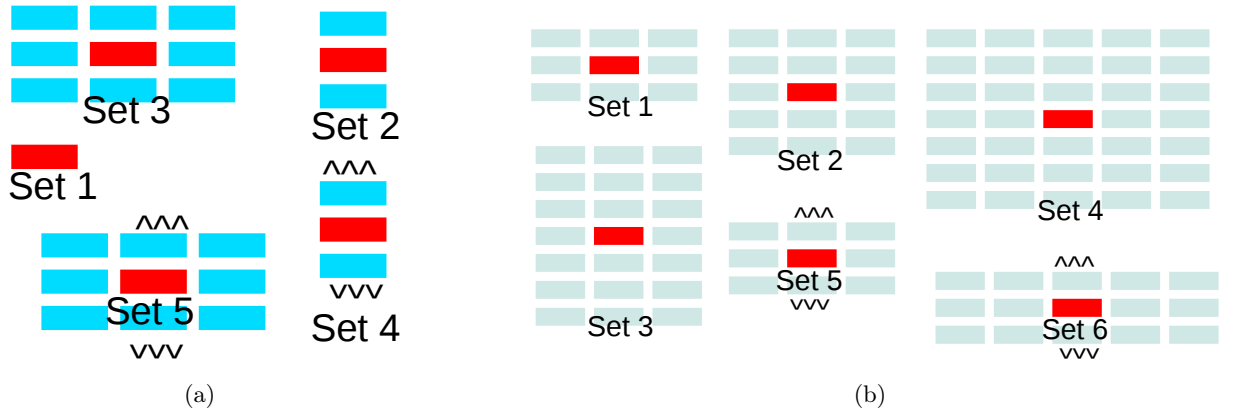
Figure (A.5) **(a)** shows the different neighborhood sets for the double sided readout version. The red readout strip is the extrapolated one, the blue ones are the readout strips to be searched in for MRPC signals. Set 4 and 5 reach from bottom to top of a MRPC module. **(b)** shows the different neighborhood sets for the single end readout version. Set 5 and 6 reach from bottom to top of a MRPC module.

Appendix B

Appendix — Analysis

B.1. Dedicated Monte Carlo Events

A dedicated Monte-Carlo event set has been produced utilizing the event distribution in the Dalitz plot of the real data. The following example may demonstrate the way of production: When a certain bin in the Dalitz plot of the measured data contains x times more events then a different bin; x times more events, originating from an phase space Monte-Carlo data sample (and arising in the same bin), are used as input for the dedicated Monte Carlo sample.

The plots in figure B.3 to B.5 show the comparison of the data and the dedicated Monte Carlo sample and are self-explanatory. The θ angle and the ϕ angle are the azimuthal (ϕ) and polar (θ) angles of the corresponding particle in the BESIII coordinate system (z-axis is the beam axis, y-axis is pointing upwards).

Figure B.6, B.7 and B.8 show the comparison of the angular distributions for the π^0 in the proton-π^0 and in the antiproton-π^0 reference system. As quantization-axis the direction of flight of the respective system is chosen. They seem to be highly asymmetric: However, this asymmetry is only arising due to kinematic reflection (i.e. combining the π^0 with the "wrong" baryon).
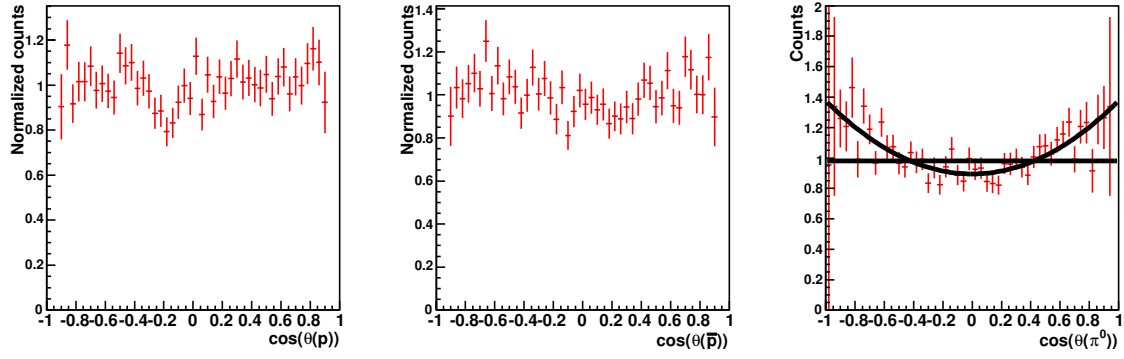
Figure (B.1) The ratio of the $\cos(\theta)$ of the proton (left), antiproton (middle) and the π^0 (right) of data and a PHSP MC sample. The functions in figure of the π^0 are a linear fit to the data and a fit with $\beta(1 + \alpha \cos^2 \theta)$.
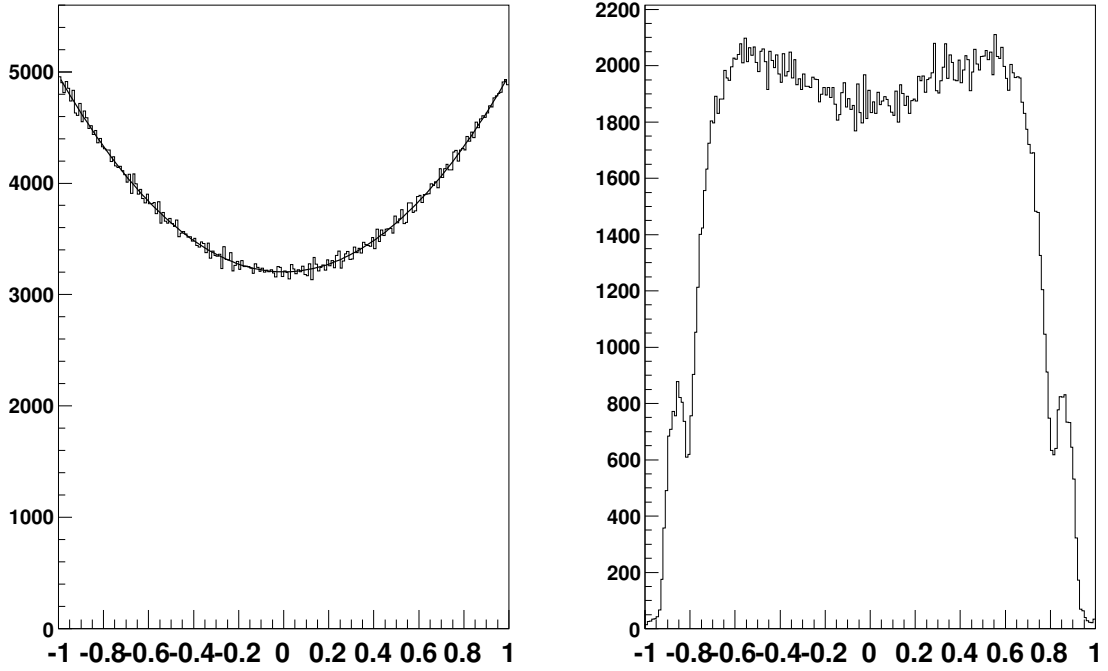

Figure (B.2) (left) MC-Truth sample with the corrected $\cos\theta$ distribution at E_{cm}=3.773 GeV; (right) events of this sample, which pass the event selection criteria.
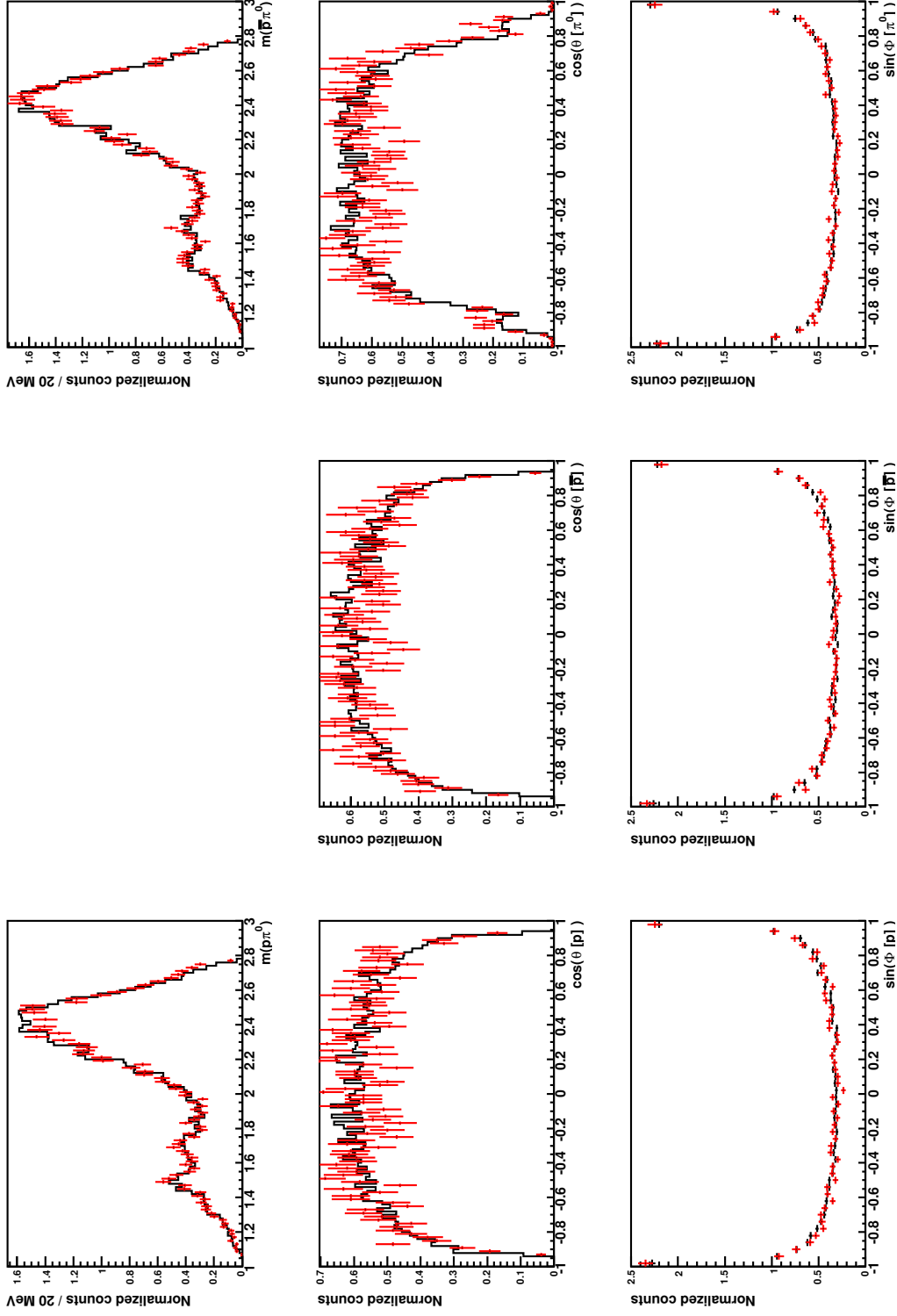
Figure (B.3) Comparison of $\cos(\theta)$ and $\sin(\phi)$ of the dedicated Monte Carlo sample and the collected data for the mass range given by the upper two plots. The $\cos(\theta)$ of the π^0 is not tuned yet.
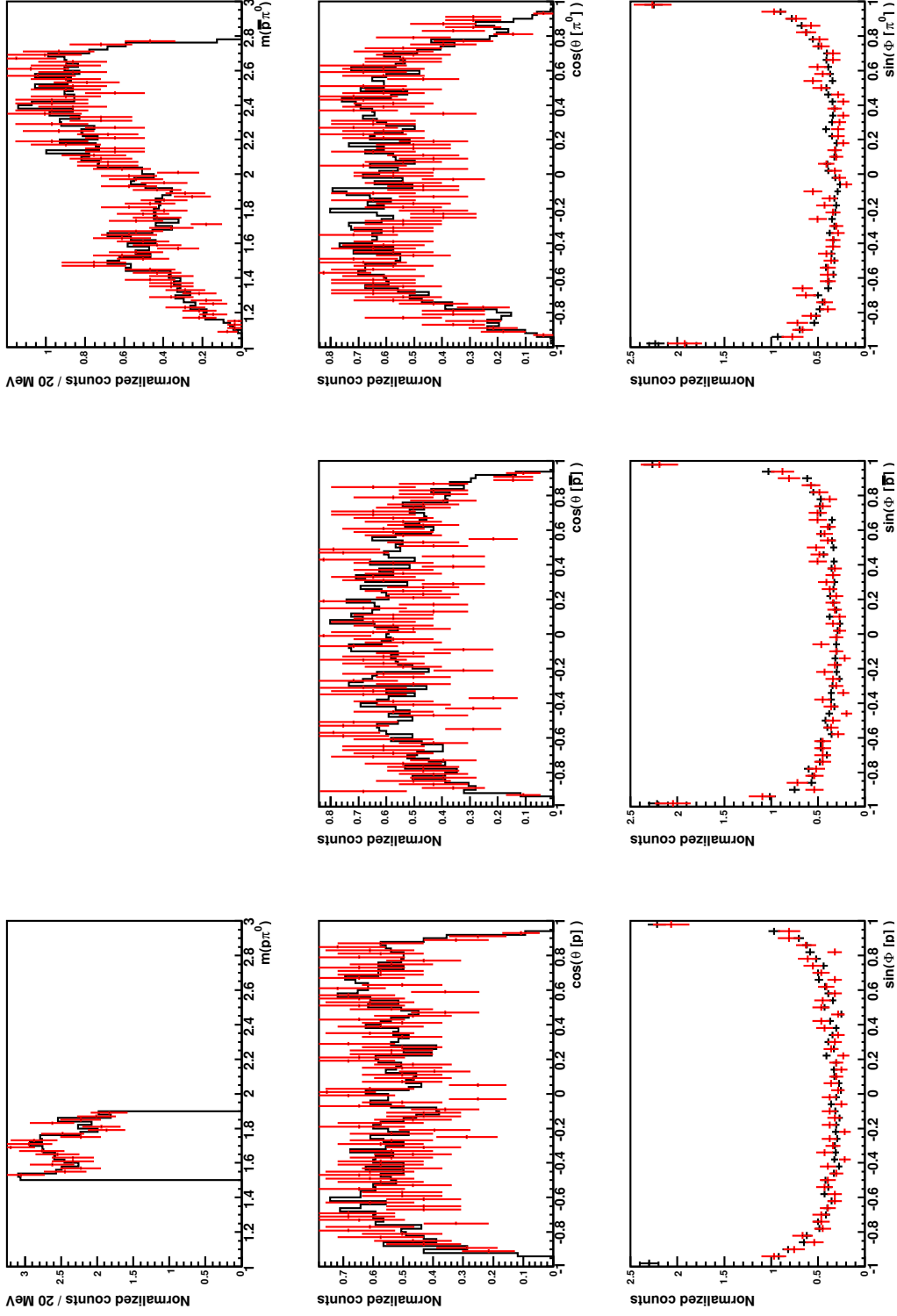
Figure (B.4) Comparison of $\cos(\theta)$ and $\sin(\phi)$ of the dedicated Monte Carlo sample and the collected data for the mass range given by the upper two plots. The $\cos(\theta)$ of the π^0 is not tuned yet.
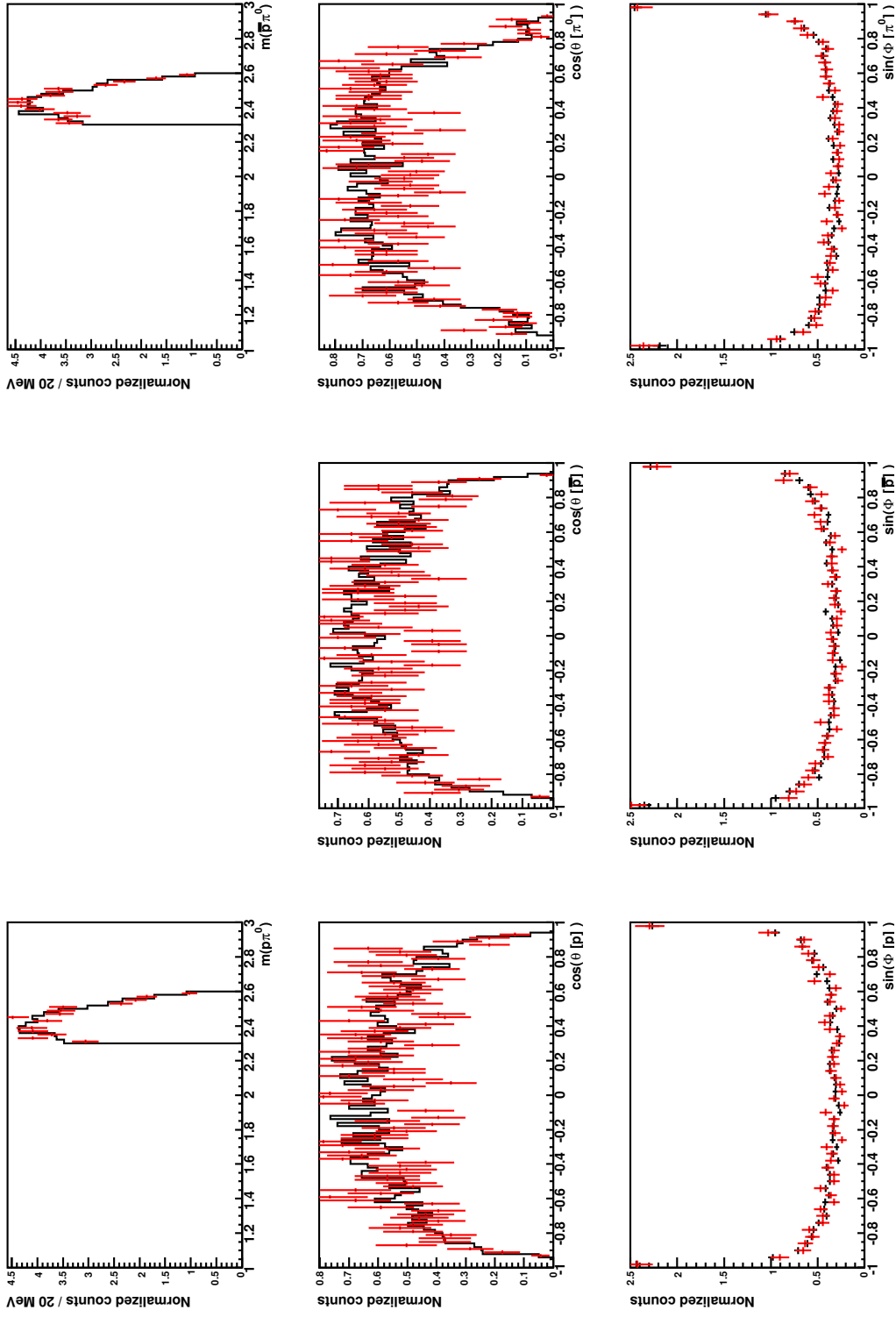
Figure (B.5) Comparison of cos (θ) and sin (ϕ) of the dedicated Monte Carlo sample and the collected data for the mass range given by the upper two plots. The cos (θ) of the π^0 is not tuned yet.
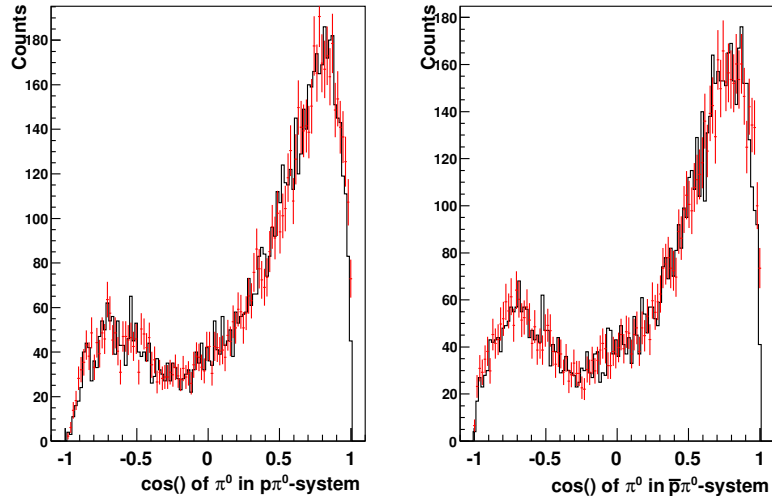
Figure (B.6)   No cut on mass($\bar{p}\pi^0$) and mass($p\pi^0$) - red MC, black data. For details it is referred to the text in section B.1.
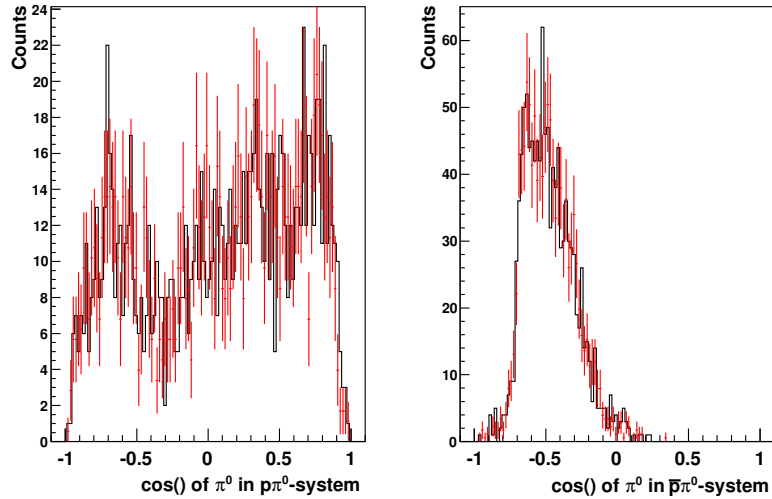
Figure (B.7)   No cut on mass($\bar{p}\pi^0$) and 1.5 GeV^2 < mass($p\pi^0$) <1.9 GeV^2 - red MC, black data. For details it is referred to the text in section B.1.
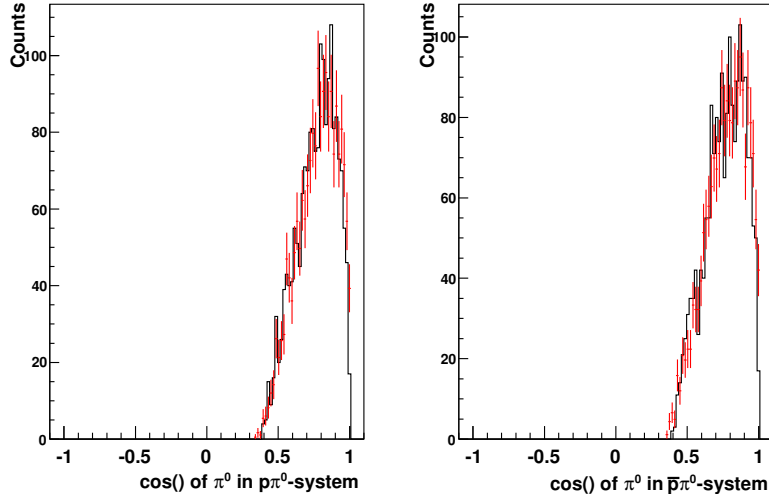
Figure (B.8) Applied cuts: $2.3\,\mathrm{GeV}^2 < \mathrm{mass}(\overline{p}\pi^0) < 2.6\,\mathrm{GeV}^2$ and $2.3\,\mathrm{GeV}^2 < \mathrm{mass}(p\pi^0)$ $< 2.6\,\mathrm{GeV}^2$ - red MC, black data. For details it is referred to the text in section B.1.

B.2. Detection Efficiencies Events with Radiated Photons

The detection efficiency for events with a photon, which was emitted in the initial state has been determined by Monte Carlo simulations. Figure B.9 shows the detection efficiencies normalized to the number of events without a photon in the initial state.
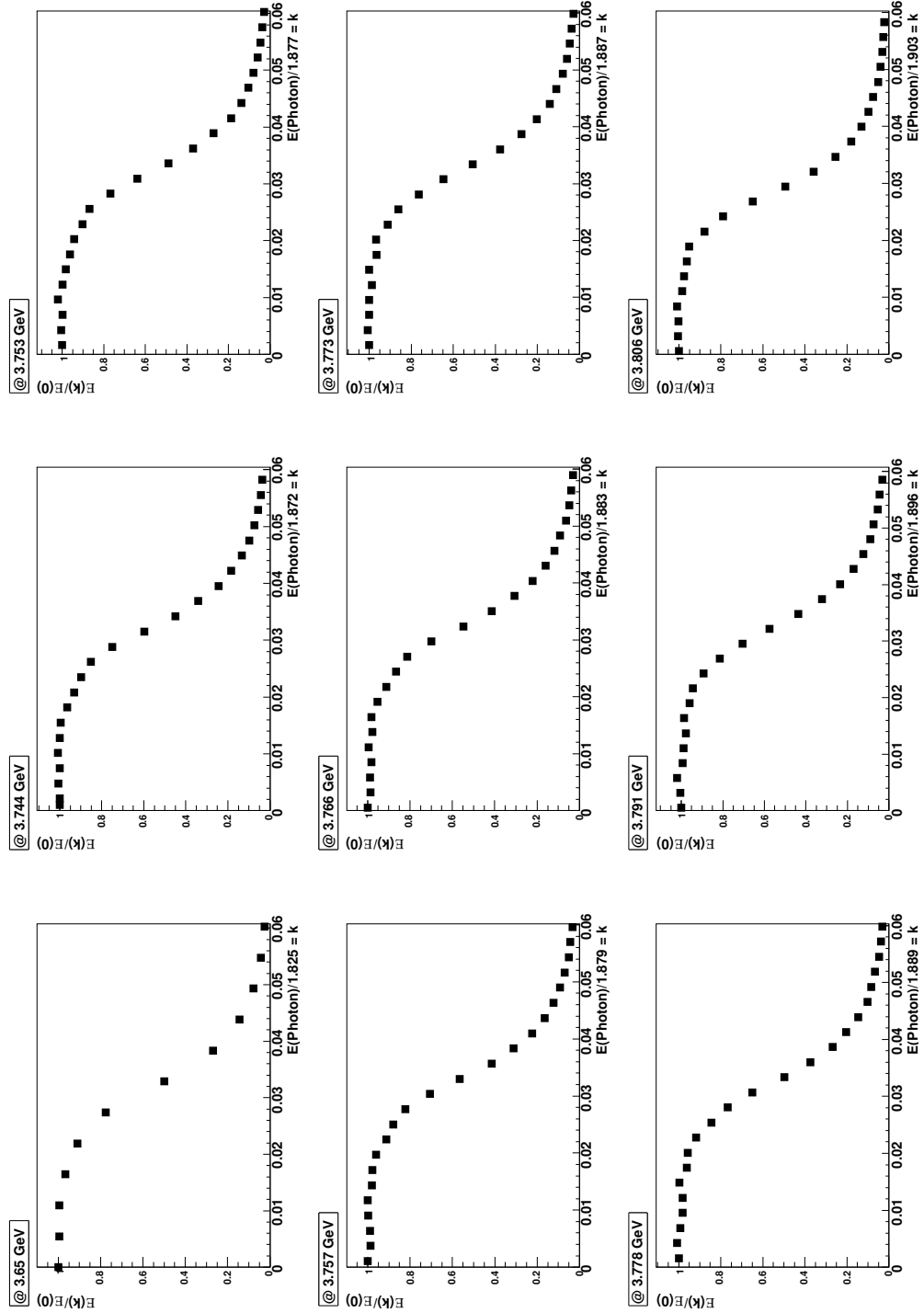
Figure (B.9) Detection efficiencies of events with a radiated photons at different energy points normalized to the detection efficiency of events without an ISR photon.

Bibliography

[1] M. Lutz et al. (PANDA Collaboration), ArXiv e-prints (2009), `hep-ex/0903.3905`.

[2] W. Erni et al. (PANDA Collaboration), ArXiv e-prints (2012), `physics.ins-det/1207.6581`.

[3] T. Barnes and X. Li, Phys. Rev. D **75**, 054018 (2007).

[4] N. Isgur and J. Paton, Phys. Rev. D **31**, 2910 (1985).

[5] J. Merlin and J. Paton, Phys. Rev. D **35**, 1668 (1987).

[6] X. Liao and T. Manke, ArXiv e-prints (2002), `hep-lat/0210030`.

[7] G. S. Bali, Eur.Phys.J. **A19**, 1 (2004).

[8] A. Lundborg, T. Barnes, and U. Wiedner, Phys. Rev. D **73**, 096003 (2006).

[9] T. A. Armstrong et al., Phys. Rev. Lett. **69**, 2337 (1992).

[10] J. Beringer et al. (Particle Data Group), Phys. Rev. D **86**, 010001 (2012).

[11] A. Kaidalov and P. Volkovitsky, Zeitschrift für Physik C **63**, 517 (1994), ISSN 0170-9739.

[12] P. Kroll, B. Quadder, and W. Schweiger, Nuclear Physics B **316**, 373 (1989), ISSN 0550-3213.

[13] E. Braaten, Phys. Rev. D **77**, 034019 (2008).

[14] M. K. Gaillard, L. Maiani, and R. Petronzio, Physics Letters B **110**, 489 (1982).

[15] E. Eichten et al., Phys. Rev. Lett. **34**, 369 (1975).

[16] J. L. Rosner, Phys. Rev. D **64**, 094002 (2001).

[17] P. A. Rapidis et al., Phys. Rev. Lett. **39**, 526 (1977).

[18] L.-H. Chan and R. O'Connell, Physics Letters B **76**, 121 (1978).

[19] M. Ablikim et al. (BES Collaboration), Phys. Rev. Lett. **97**, 121801 (2006).

[20] M. Ablikim et al. (BES Collaboration), Phys. Rev. D **76**, 122002 (2007).

[21] M. Ablikim et al. (BES Collaboration), Physics Letters B **641**, 145 (2006).

[22] M. Ablikim et al. (BES Collaboration), Physics Letters B **659**, 74 (2008).

[23] D. Besson et al. (CLEO Collaboration), Phys. Rev. Lett. **96**, 092002 (2006).

[24] P. Wang, X. H. Mo, and C. Z. Yuan, International Journal of Modern Physics A **21**, 5163 (2006).

[25] P. Wang, C. Yuan, X. Mo, and D. Zhang (2002), `hep-ph/0212139`.

[26] N. E. Adam et al. (CLEO Collaboration), Phys. Rev. Lett. **96**, 082004 (2006).

[27] T. E. Coan et al. (CLEO Collaboration), Phys. Rev. Lett. **96**, 182002 (2006).

[28] R. A. Briere et al. (CLEO Collaboration), Phys. Rev. D **74**, 031106 (2006).

[29] M. Ablikim et al., Nuclear Instruments and Methods in Physics Research Section A: Accelerators, Spectrometers, Detectors and Associated Equipment **614**, 345 (2010).

[30] D. Asner et al., Int. J. Mod. Phys. **A24**, S1 (2009).

[31] S.-K. Choi, S. L. Olsen, et al. (Belle Collaboration), Phys. Rev. Lett. **91**, 262001 (2003).

[32] R. Aaij et al. (LHCb collaboration), Phys. Rev. Lett. **110**, 222001 (2013).

[33] M. Ablikim et al. (BESIII Collaboration), Phys. Rev. Lett. **110**, 252001 (2013).

[34] G. Aad et al. (ATLAS Collaboration), Phys. Lett. **B716**, 1 (2012).

[35] S. Chatrchyan et al. (CMS Collaboration), Phys. Lett. **B716**, 30 (2012).

[36] W. Erni et al. (PANDA Collaboration) (2009), `physics.ins-det/0907.0169`.

[37] E. Eichten, K. Gottfried, T. Kinoshita, K. D. Lane, and T. M. Yan, Phys. Rev. D **17**, 3090 (1978).

[38] G. Breit, Phys. Rev. **34**, 553 (1929).

[39] G. Breit, Phys. Rev. **39**, 616 (1932).

[40] J. Eiglsperger, ArXiv e-prints (2007), `hep-ph/0707.1269`.

[41] T. Barnes, S. Godfrey, and E. S. Swanson, Phys. Rev. D **72**, 054026 (2005).

[42] S. Okubo, Phys. Lett. **5**, 165 (1963).

[43] G. Zweig, CERN Report No. 8419/TH-4126 (1964).

[44] J. Iizuka, Progress of Theoretical Physics Supplement **37-38**, 21 (1966).

[45] H. Stockhorst et al., in *Proceedings of EPAC08, Genoa, Italy, THP055* (2008), p. 3491.

[46] B. Gålander et al., in *Proceedings of EPAC08, Genoa, Italy, THP049* (2008), p. 3473.

[47] W. Erni et al. (PANDA Collaboration), ArXiv e-prints (2012), `physics. ins-det/1205.5441`.

[48] B. Aubert et al. (BaBar Collaboration), Nucl. Instrum. Meth. **A479**, 1 (2002).

[49] W. Erni and others (PANDA Collaboration), ArXiv e-prints (2008), `physics. ins-det/0810.1216`.

[50] M. Ye and Z. Zheng, International Journal of Modern Physics A **02**, 1707 (1987).

[51] J. Baia et al., Nuclear Instruments and Methods in Physics Research Section A: Accelerators, Spectrometers, Detectors and Associated Equipment **344**, 319 (1994).

[52] J. Bai et al., Nuclear Instruments and Methods in Physics Research Section A: Accelerators, Spectrometers, Detectors and Associated Equipment **458**, 627 (2001).

[53] X. Li, Q. Ji, L. Wang, and L. Zheng, Nuclear Instruments and Methods in Physics Research Section A: Accelerators, Spectrometers, Detectors and Associated Equipment **585**, 40 (2008).

[54] W. Yong-gang, Z. Tao, X. Zi-zong, S. Qing, and H. Tao, in *Instrumentation and Measurement Technology Conference Proceedings, 2008. IMTC 2008. IEEE* (2008), pp. 1155–1158.

[55] M. Anelli et al., Nuclear Instruments and Methods in Physics Research Section A: Accelerators, Spectrometers, Detectors and Associated Equipment **718**, 118 (2013).

[56] C. Chen et al., in *Nuclear Science Symposium Conference Record, 2007. NSS '07. IEEE* (2007), vol. 3, pp. 1844–1846.

[57] J. Liu et al., Nuclear Instruments and Methods in Physics Research Section A: Accelerators, Spectrometers, Detectors and Associated Equipment **557**, 436 (2006).

[58] M. Adinolfi et al., Nuclear Instruments and Methods in Physics Research Section A: Accelerators, Spectrometers, Detectors and Associated Equipment **461**, 25 (2001).

[59] S. Uno, Nuclear Instruments and Methods in Physics Research Section A: Accelerators, Spectrometers, Detectors and Associated Equipment **379**, 421 (1996).

[60] D. Peterson, Nuclear Instruments and Methods in Physics Research Section A: Accelerators, Spectrometers, Detectors and Associated Equipment **409**, 204 (1998).

[61] G. Sciolla et al., Nuclear Instruments and Methods in Physics Research Section A: Accelerators, Spectrometers, Detectors and Associated Equipment **419**, 310 (1998).

[62] Y. Heng, C. Wu, Z. Sun, et al., eConf **C0604032**, 0115 (2006).

[63] Y. Heng, in *Nuclear Science Symposium Conference Record, 2007. NSS '07. IEEE* (2007), vol. 1, pp. 53–56.

[64] S. Shengsen, Journal of Physics: Conference Series **396**, 022051 (2012).

[65] C. Wu et al., Nuclear Instruments and Methods in Physics Research Section A: Accelerators, Spectrometers, Detectors and Associated Equipment **555**, 142 (2005).

[66] Z. Chuan et al., Chinese Physics C **35**, 72 (2011).

[67] D. Ming-Yi et al., Chinese Physics C **32**, 908 (2008).

[68] C. Liu, Journal of Physics: Conference Series **293**, 012048 (2011).

[69] J. Zhang et al., Nuclear Instruments and Methods in Physics Research Section A: Accelerators, Spectrometers, Detectors and Associated Equipment **614**, 196 (2010).

[70] T. Carli and B. Koblitz, Nuclear Instruments and Methods in Physics Research Section A: Accelerators, Spectrometers, Detectors and Associated Equipment **501**, 576 (2003).

[71] P. C. Bhat (D0 Collaboration), AIP Conf.Proc. **357**, 308 (1996).

[72] C. M. Bishop, *Neural networks for pattern recognition* (Oxford University Press, 1995).

[73] Y.-J. M. Wei-Dong Li and Y.-F. Wang, International Journal of Modern Physics A **24**, 9 (2009).

[74] S. Agostinelli et al., Nuclear Instruments and Methods in Physics Research Section A: Accelerators, Spectrometers, Detectors and Associated Equipment **506**, 250 (2003).

[75] P. Cortese et al. (ALICE Collaboration) (2002), ALICE: Addendum to the technical design report of the time of flight system (TOF).

[76] H. A. Pol, R. Alves, et al., Nuclear Instruments and Methods in Physics Research Section A: Accelerators, Spectrometers, Detectors and Associated Equipment **535**, 277 (2004).

[77] Y. Sun et al., Nuclear Instruments and Methods in Physics Research Section A: Accelerators, Spectrometers, Detectors and Associated Equipment **593**, 307 (2008).

[78] R. Santonico and R. Cardarelli, Nuclear Instruments and Methods in Physics Research **187**, 377 (1981).

[79] W. M.C.S., Nuclear Physics B - Proceedings Supplements **61**, 250 (1998).

[80] H. Zhang et al., ArXiv e-prints (2012), `physics.ins-det/1208.3049`.

[81] F. Anghinolfi et al., Nuclear Instruments and Methods in Physics Research Section A: Accelerators, Spectrometers, Detectors and Associated Equipment **533**, 183 (2004).

[82] CERN Technology portfolio, *High performance time to digital converter*, http://cern.ch/knowledgetransfer.

[83] J. Christiansen, *Hptdc – high performance time to digital converter*, http://tdc.web.cern.ch/tdc/hptdc/docs/hptdc_manual_ver2.2.pdf.

[84] W. Legler, Z. Naturforschg. **16a**, 253 (1961).

[85] W. Riegler, C. Lippmann, and R. Veenhof, Nuclear Instruments and Methods in Physics Research Section A: Accelerators, Spectrometers, Detectors and Associated Equipment **500**, 144 (2003).

[86] C. Lippmann and W. Riegler, Nuclear Instruments and Methods in Physics Research Section A: Accelerators, Spectrometers, Detectors and Associated Equipment **517**, 54 (2004).

[87] M. Abbrescia et al., *Progesses in the simulation of resistive plate chambers in avalanche mode*, MS Conference Report CMS CR 1998/021.

[88] S. Ramo, *Currents induced in electron motion*, Proceedings IRE 27 (1939).

[89] M. Shao et al., Measurement Science and Technology **17**, 123 (2006).

[90] S. Biagi, Nuclear Instruments and Methods in Physics Research Section A: Accelerators, Spectrometers, Detectors and Associated Equipment **421**, 234 (1999).

[91] S. Biagi, Nuclear Instruments and Methods in Physics Research Section A: Accelerators, Spectrometers, Detectors and Associated Equipment **283**, 716 (1989).

[92] W. B. W. Riegler and L. Rolandi, *Particle Detection with Drift Chambers* (Springer, 2008).

[93] A. Pansky, A. Breskin, and R. Chechik, Journal of Applied Physics **82**, 871 (1997).

[94] Y. H. Hilal and L. G. Christophorou, Journal of Physics D: Applied Physics **20**, 975 (1987).

[95] A. Sharma, *Properties of some gas mixtures used in tracking detectors* (1998).

[96] CAEN, *Technical Information Manual, MOD. V1290 A/N and VX1290 A/N, Revision n.15.*, http://www.caen.it/ (2012).

[97] D. Hongliang, *Private communication*.

[98] S. Yang, Y. Sun, C. Li, and other, *MRPC prototypes for the BESIII end-cap time-of-flight system upgrade* (2013), *to be published.*

[99] S. Jadach, B. Ward, and Z. Was, Comput. Phys. Commun. **130**, 260 (2000).

[100] A. Ryd et al., *EvtGen: A Monte Carlo Generator for B-Physics* (2005).

[101] T. Ullrich and Z. Xu, ArXiv Physics e-prints (2007), `arXiv:physics/0701199`.

[102] I. Fröhlich, Ph.D. thesis, Justus-Liebig-Universiät Giessen (2002).

[103] H.-W. Pfaff, Ph.D. thesis, Justus-Liebig-Universiät Giessen (1999).

[104] M. Ablikim et al. (BESIII Collaboration), Phys. Rev. D **83**, 112009 (2011).

[105] C. Edwards, R. Partridge, C. Peck, F. Porter, D. Antreasyan, et al., Phys. Rev. D (1990).

[106] H. Hu, *Initial Radiative Correction for R Measurement at BES* (2001).

[107] G. Rong, D. Zhang, and J. Chen, ArXiv e-prints (2010), `hep-ph/1003.3523`.

[108] P. Wang, C. Yuan, and X. Mo, Physics Letters B **574**, 41 (2003).

[109] J. E. Augustin et al., Phys. Rev. Lett. **34**, 764 (1975).

[110] E. A. Kuraev and V. S. Fadin, Sov. J. Nucl. Phys. 41, 466 (1985).

[111] O. Nicrosini and L. Trentadue, Physics Letters B **196**, 551 (1987).

[112] M. Benayoun, S. I. Eidelman, V. N. Ivanchenko, and Z. K. Silagadze, Modern Physics Letters A **14**, 2605 (1999).

[113] M. Ablikim et al. (BESIII Collaboration), Phys.Rev. **D87**, 112011 (2013).

[114] M. Ablikim et al. (BESIII Collaboration), Phys. Rev. D **83**, 112005 (2011).

[115] M. Ablikim et al. (BESIII Collaboration), ArXiv e-prints (2013), `1307.2022`.

[116] M. Botje, Journal of Physics G: Nuclear and Particle Physics **28**, 779 (2002).

[117] C. Gwenlan, *Talk: Treatment of correlated systematic uncertainties in the ZEUS QCD Fit.*

[118] J. Ellis and M. Karliner, New Journal of Physics **4**, 18 (2002).

[119] M. Karliner, Nuclear Physics B - Proceedings Supplements **108**, 84 (2002).

[120] J. L. Rosner, Annals of Physics **319**, 1 (2005), ISSN 0003-4916.

[121] J. L. Rosner, ArXiv e-prints (2004), `hep-ph/0405196`.

[122] H. O'Connell, B. Pearce, A. Thomas, and A. Williams, Progress in Particle and Nuclear Physics **39**, 201 (1997).

[123] A. Goldhaber, G. Fox, and C. Quigg, Physics Letters B **30**, 249 (1969).

[124] K. ZHU, X. H. MO, C. Z. YUAN, and P. WANG, International Journal of Modern Physics A **26**, 4511 (2011).

[125] M. Ablikim et al. (BESIII Collaboration), Phys. Rev. D **86**, 032014 (2012).

[126] P. Wang, C. Z. Yuan, and X. H. Mo, Phys. Rev. D **69**, 057502 (2004).

Eidesstattliche Versicherung

Ich erkläre: Ich habe die vorgelegte Dissertation selbständig und ohne unerlaubte fremde Hilfe und nur mit den Hilfen angefertigt, die ich in der Dissertation angegeben habe. Alle Textstellen, die wörtlich oder sinngemäß aus veröffentlichten Schriften entnommen sind, und alle Angaben, die auf mündlichen Auskünften beruhen, sind als solche kenntlich gemacht. Bei den von mir durchgeführten und in der Dissertation erwähnten Untersuchungen habe ich die Grundsätze guter wissenschaftlicher Praxis, wie sie in der "Satzung der Justus-Liebig-Universität Gießen zur Sicherung guter wissenschaftlicher Praxis" niedergelegt sind, eingehalten.

Gießen,

Matthias Ullrich

Danksagung